KfK 4949
Dezember 1991

# A Three-Field Model of Transient 3D Multiphase, Three-Component Flow for the Computer Code IV A3

## Part 2: Models for the Interfacial Transport Phenomena. Code Validation.

N. I. Kolev
Institut für Neutronenphysik und Reaktortechnik

Kernforschungszentrum Karlsruhe

KERNFORSCHUNGSZENTRUM KARLSRUHE
Institut für Neutronenphysik und Reaktortechnik

KfK 4949

# A THREE–FIELD MODEL OF TRANSIENT 3D MULTIPHASE, THREE–COMPONENT FLOW FOR THE COMPUTER CODE IVA3

## Part 2: Models for the Interfacial Transport Phenomena. Code Validation.

N. I. Kolev

Kernforschungszentrum Karlsruhe GmbH, Karlsruhe

Kernforschungszentrum Karlsruhe GmbH
Postfach 3640, 7500 Karlsruhe 1

ISSN 0303-4003

## Abstract

The second part of the IVA3 code description contains the constitutive models used for the interfacial transport phenomena and the code validation results.

First 20 flow patterns are defined and the transition criteria are discussed. The dynamic fragmentation and coalescence models used in IVA3 are documented. After the description of the models for predicting the flow patterns and flow structure sizes the models for the interfacial mechanical interaction are described. Finally the models for interfacial heat and mass transfer are given with emphasis on the time averaging of the heat and mass source terms.

The code validation passes several stages from simple tests on well known benchmarks trough simulation of one–, two–, and three–phase flows in simple and complicated geometries. The gradually increase of the complexity and the successful comparison of the predictions with experimental data is the main characteristic of the verification procedure. It is demonstrated by several examples that IVA3 is a powerful tool for three–fluid modelling of complicated three–phase flows in complex geometry with strong thermal and mechanical interaction between the velocity fields.


Ein Drei–Feld Modell der transienten 3D Multiphasen Drei–Komponenten Strömung für das Rechenprogramm IVA3

Teil 2: Modelle für die Zweiphasen–Transport Phänomene. Programm–Validierung


## Kurzfassung

Der zweite Teil der Beschreibung des IVA3 Computerprogramms beinhaltet die verwendeten Modelle für Transport von Masse, Impuls und Energie an den Phasentrennflächen und die Codevalidierung.

Zunächst werden 20 komplexe Strömungsmuster definiert und die dazugehörigen Identifikationskriterien diskutiert. Die Modelle für dynamische Fragmentation und Koaleszenz, die in IVA3 verwendet sind, werden detailliert dokumentiert. Nach der Darstellung der Methoden für Identifikation der Strömungsmuster und für die Berechnung der Partikelgröße werden die Modelle für die Berechnung der Kräfte an den Phasentrennflächen beschrieben. Abschließend wurden die Modelle für zeitlich gemittelten Massen– und Energietransport an den Phasentrennflächen beschrieben.

Die Funktionsüberprüfung des IVA3–Algorithmus sowie die Überprüfung der physikalischen Modelle und deren Wechselwirkung geht von einfachen Tests mit bekannten Benchmarks, bis hin zur Simulation von Ein–, Zwei– und Dreiphasenströmungen in einfachen und komplexen Geometrien. Die allmähliche Steigerung der Komplexität der modellierten Strömungen und der erfolgreiche Vergleich von Simulationsergebnissen mit Experimenten sind die wichtigsten Charakteristiken der Verifikationsprozedur.

Es wird an mehreren Beispielen demonstriert, daß IVA3 eine leistungsfähige

Rahmenstruktur für Modellierung von Dreiphasenströmungen in komplexer Geometrie mit schwachen bis sehr heftigen thermischen und mechanischen Wechselwirkungen zwischen den Geschwindigkeitsfeldern darstellt.

CONTENTS

# 1. POSTULATED FLOW REGIMES

Formalizing the flow description by using multifluid representation needs definition of closure laws for the transport processes at the interfaces separating the different velocity fields from each other. These closure laws contain essential some particular solution of the equations representing the conservation principles for the particular geometry and initial conditions at the beginning of the time step considered. Analytical solutions are obtained usually under given simplifying assumptions about the process controlling mechanisms and later modified in order to predict some class of experiments. This makes it necessary to divide the definition region of the local parameters and geometries into well defined structures and situations and to use specific closure laws in each particular surface geometry and each particular parameter situation. No doubt that this is complicated but for the time being it seems to be the only practicable way to close the system of PDE's describing the multiphase flow. Constitutive relationships have been obtained theoretically and experimentally by thousands of authors all over the world. The reader can obtain basic information about this field in Slattery [1] (1990) and about the extent of these investigations and some of the results obtained from the valuable handbooks edited by Skripov et al. [2] (1980), Hetsroni [3] (1982), Rohsenow et al. [4] (1985), or in Shah et al [5] (1988) etc. Nevertheless, at the present time there are several combinations of phases, components, velocity fields, and flow patterns that are not provided with reliable empirical information. Although the very ambitious task to present the modern state of the art in this field could be extremely valuable for practical applications, it is beyond the scope of this work.

The purpose of this section is to summarize the IVA3 selection of constitutive models for interfacial transport phenomena covering the limited but very useful number of main flow patterns presented in Fig.1.

Table 1 summarizes the postulated flow regimes in IVA3.

Table 1 Postulated flow regimes in IVA3

| | |
|---|---|
| | One velocity field only: |
| 1 | Velocity field 1 (gas) only. |
| 2 | Velocity field 2 (water) only. |
| 3 | Velocity field 3 (liquid metal) only. |
| | Two velocity fields only: |
| 4 | Two phase bubble flow – continuous velocity field 2 and discrete velocity field 1 (gas). |
| 5 | Two phase slug flow – continuous velocity field 2 and discrete velocity field 1 (gas). |
| 6 | Two phase churn turbulent flow – continuous velocity field 2 and discrete velocity field 1 (gas). |
| 7 | Two phase dispersed flow – continuous velocity field 1 (gas), discrete velocity field 2 (droplets) for pool flow. |
| 8 | Annular flow – continuous velocity field 1 (gas) and continuous velocity field 2 (water film), identified only for flow in confined geometry. |
| 9 | Dispersed velocity field 3 (liquid metal droplets or solid particles) in continuous velocity field 2 (water). |
| 10 | Dispersed velocity field 2 (water droplets) in continuous velocity field 3 (liquid metal). |

11 Continuous velocity field 1 (gas) and dispersed velocity field 3 (water droplets).
12 Continuous velocity field 1 (gas) and dispersed velocity field 3 (solid particles).
13 Dispersed velocity field 1 (gas bubbles) in continuous velocity field 3 (liquid metal).
14 Continuous velocity field 1 (gas) and dispersed velocity field 3 (solid particles or liquid metal droplets).

Three velocity fields:

15 Three phase bubble flow – dispersed velocity field 1 (gas bubbles), continuous velocity field 2 (water) and dispersed velocity field 3 (liquid metal or solid particles.
16 Continuous velocity field 1 (gas), dispersed velocity field 2 (water droplets) and dispersed velocity field 3 (solid particles or liquid metal droplets or porous velocity field 3) – for pool flow only.
17 Continuous velocity field 1 (gas), dispersed velocity field 2 (water droplets) surrounded by continuous velocity field 3 (porous liquid metal with large particle diameters).
18 Continuous velocity field 1 (gas), continuous velocity field 2 (water) and discrete velocity field 3 (water droplets) – only for flow in confined geometry.

19 Continuous velocity field 1 (gas), continuous velocity field 2 (water) and discrete velocity field 3 (solid particles) – only for flow in confined geometry.

20 Dispersed velocity field 1 (gas bubbles), continuous velocity field 2 (water) and continuous velocity field 3.

---

The corresponding identification number is assigned to an integer vector. Another vector contains the flow regime identification in the old time level. Comparing the two parameters, IVA3 identifies the moment in which the actual structure in the computational cells changes. This information is further used in order to model e.g the fragmentation processes of solid velocity fields that are not solid.

Note that the code architecture is highly modular and allows definition of additional flow patterns and models for the interfacial transport not covered by the regimes given in Table 1 as far as it is necessary for a given practical application.

Rewriting here all models with their symbol definitions, equations and subsequent time averaging would be very voluminous and would by far exceed the usual volume of publication. That is why we prefer to describe briefly the main characteristics of each model and the reference in which the arguments for its derivation are documented.

The introduction of the velocity fields associated with substances and the introduction of the flow regimes requires additional information to identify which of these structures exists in the actual computational cell. Some of them are trivially identified by only checking the values of volume fractions and inert mass concentrations of the velocity fields. The others are identified by using (a) existing empirical correlations and/or (b) a logical set of geometry considerations. For the flow in confined geometry we use Mishima and Ishii's map [6] (1984) for vertical upward flow. For the identification of the flow regimes with entrainment as well for the computation of the entrainment mass flow rate, $(\rho w)_{23}$, in the source term

$$\mu_{23} = \bar{a}_{12}(\rho w)_{23}. \tag{1.1}$$

we use Kataoka and Ishii's work [7] (1982). Kataoka and Ishii distinguish two entrainment regimes depending on whether droplets are under–entrained or over–entrained with respect to the equilibrium condition. In the *under entrained regime* (entrance section and smooth injection of liquid as a film causing excess liquid in the film compared to the equilibrium condition), $Re_2 > Re_{2\infty}$, and

$$(\rho w)_{23} = \frac{\eta_2}{D_h}\left[\frac{1200(Re_2 - Re_{2\infty})^2}{Re_{23}^{1/2} Re_{2\infty}^{1/4} We^{1.5}} + 6.6\ 10^{-7}\ Re_{23}^{0.74}\ Re_2^{0.185}\ We^{0.925}\ \left(\frac{\eta_1}{\eta_2}\right)^{0.26}\right], \tag{1.2}$$

In the *over entrained regime* (entrainment is caused by shearing–off of roll wave crests by gas core flow), $Re_2 \leq Re_{2\infty}$ and $Re_{23} > 160$, and

$$(\rho w)_{23} = 6.6\ 10^{-7}\ Re_{23}^{0.74}\ Re_2^{0.185}\ We^{0.925}\ \left(\frac{\eta_1}{\eta_2}\right)^{0.26}, \tag{1.3}$$

where $Re_2 = \alpha_2\rho_2|V_2|D_h/\eta_2$, $Re_{2\infty} = Re_{23}\,(1-E_n)$, $E_n = \tanh(7.25\ 10^{-7}\ We^{1.25}\ Re_{23}^{1/4})$, $We = \rho_1(\alpha_1 V_1)^2 D_h\ \left(\frac{\rho_2-\rho_1}{\rho_1}\right)^{1/3}/\sigma_2$, $Re_{23} = \rho_2(1-\alpha_1)|V_{23}|D_h/\eta_2$, and $V_{23} = (\alpha_2 V_2 + \alpha_3 V_3)/(1-\alpha_1)$.

The *diffusion droplet deposition* flow rate $(\rho w)_{32}$ to the film in case of dispersed – annular flow in the source term

$$\mu_{32} = \bar{a}_{12}(\rho w)_{32}, \qquad \alpha_3 > 0.0001, \tag{1.4}$$

is computed using the correlation of Paleev and Filipovich [8] (1966)

$$(\rho w)_{32} = (\eta_3/D_h)\ 0.022\ (\eta_1/\eta_3)^{0.26}\ (\alpha_3\rho_2 V_3 D_h/\eta_2)^{0.74}. \tag{1.5}$$

$$\bar{a}_{12} = (4/D_h)\ \sqrt{1-\alpha_2} \tag{1.6}$$

in Eq. 1.4 is the common surface between gas and film per unit flow volume.

## 2. PARTICLE NUMBER DENSITY

To describe the geometrical scales of the structures, e.g. bubble or droplet diameters etc., we introduce the particle number density of each velocity field. For fields identified to occupy the cell fully, the number of the particles in the cell is zero, for continuous fields it is less than one, and for discrete fields it is greater than one. The IVA3 model uses three partial differential equations to describe the conservation of the particle number density for each velocity field taking into account time changes due to convection and/or other sources. Mechanical sources, i.e. fragmentation and collisions, are modelled by means of "production rates" defined by the difference between the actual particle density and the stable one divided by the time constant of the process. Empirical information in form of correlations is used to compute (a) the stable particle number density and (b) the time constant for the corresponding mechanism.

As already mentioned, the main characteristics of the fragmentation process are (a) the stable particle diameter after fragmentation, $D_{d\infty}$, and (b) its duration. Having $D_{d\infty}$ we compute the particle number density for the time after the fragmentation

$$n_{d\infty} = \alpha_d/(\pi D_{d\infty}^3/6) \tag{2.1}$$

and finally the production rate

$$\dot{n}_{dsp} = \frac{n_{d\infty}-n_d}{\Delta\tau_{br}} = n_d\,[(\frac{D_d}{D_{d\infty}})^3-1]/\Delta\tau_{br}, \tag{2.2}$$

or having in mind that

$$\frac{D_d}{D_{d\infty}} = \frac{We_d}{We_{d\infty}}\,(\frac{V_c-V_{c\infty}}{V_c-V_d})^2 \tag{2.3}$$

we obtain

$$\dot{n}_{dsp} = n_d\,[\,(\frac{We_d}{We_{d\infty}})^3\,(\frac{V_c-V_{c\infty}}{V_c-V_d})^6 - 1\,]/\Delta\tau_{br}. \tag{2.4}$$

This is an illustration of the strong dependence of the particle production rate on the initial Weber number and the ratio $(V_c-V_{d\infty})/(V_c-V_d)$. Setting this ratio to unity leads to overestimation of the production rate $\dot{n}_{dsp}$ because in reality the relative velocity $V_c - V_{d\infty}$ is smaller than $V_c - V_d$ in reality.

The stable volume median bubble size is computed using the correlation proposed by Ahmad [9] (1970):

$$D_{1\infty} \approx We_{1\infty}\,\frac{1}{2}\,[\frac{\sigma}{g(\rho_2-\rho_1)}]^{1/2} \tag{2.1}$$

where

$$We_{d\infty} = \frac{1.8}{1+1.34[(1-\alpha_c)w_c]^{1/3}} = We^*_{d\infty} \quad \text{for } \alpha_d < 0.1 \tag{2.2}$$

$$We_{d\infty} = We^*_{d\infty} \left(\frac{9\alpha_d}{1-1_d}\right)^{1/3} \quad \text{for } 0.1 < \alpha_d < 0.99. \tag{2.3}$$

The time constant for bubble fragmentation is simply set equal to the period of natural fluctuation

$$\Delta\tau_{br} \approx D_d/\Delta V_{cd} \tag{2.4}$$

in bubble flow assuming that the identified instability itself means equality between the relaxation time constant for bubble destruction and the period of natural fluctuation.

The stable volume median drop size for pool flow is controlled by a critical Weber number, $We_{d\infty}$, which is equal to 12:

$$D_{d\infty} = We_{d\infty}\sigma_d /[\rho_c(V_c-V_{d\infty})^2] \tag{2.5}$$

and is limited in IVA3 to the maximum stable drop size for free falling droplets

$$D^2_{d\infty} = \frac{3}{4}\frac{\sigma_d c^d_{cd}}{g\Delta\rho_{dc}} We_{d\infty}, \quad c^d_{cd} \approx 0.4. \tag{2.6}$$

For flow in confined geometry we use the correlation proposed by Kataoka and Ishii [7] (1982)

$$D_{d\infty} = \min [\, 0.01\, Re_c^{2/3}\, We_c^{-1}\, (\rho_c/\rho_d)^{-1/3}\, (\eta_c/\eta_d)^{2/3}\, D_h, D_h] \tag{2.7}$$

where $Re_c = \alpha_c\rho_c V_c D_h/\eta_c$, $We_c = (\alpha_c\rho_c V_c)^2 D_h/(\rho_c\sigma)$.

For the computation of the disintegration time constant for liquid, IVA3 distinguishes between two models: (a) jet disintegration and (b) acceleration induced droplet fragmentation.

The jet disintegration mode is used if the number of particles in the particular computational cell is less than one. Note this interesting feature of the particle number density concept – this is the way to model a kind of space memory of the flow structure, which can be convectively transported. Values of the cell particle number converging towards one indicate highly excited but continuous structure. If the cell particle number is greater than one the acceleration induced particle fragmentation may take place.

The time constant for jet disintegration is computed by dividing the computed jet

core breakup length $\Delta L_j$ with the relative velocity between the jet and the surrounding medium $\Delta V_{cj}$

$$\Delta\tau_{br} = \Delta L_j/\Delta V_{cj}. \tag{2.8}$$

using the results of Epstein and Fauske [11] (1985)

$$\Delta L_j/D_j = \frac{\sqrt{3}}{2}(1 + \rho_c/\rho_j)/(\rho_c/\rho_j)^{1/2}. \tag{2.9}$$

In the case of film boiling on the liquid metal jet surface we use the analysis reported by Epstein and Fauske [11] (1985) distinguishing between thick and thin vapor films. For thick vapor films the parameters of the surrounding medium are set equal to the steam parameters. For thin vapor films the water parameters are used as parameters of the surrounding liquid.

The time constant for acceleration induced droplet fragmentation is computed using the implicitly empirical approach proposed by Pilch, Erdman and Reynolds [12] (1981). Pilch, Erdman and Reynolds [12] (1981) correlated experimental data from many authors for free flow fragmentation of droplets with negligable initial velocity using the following approach. Introducing the modified Weber number

$$We_c = \rho_c V_c^2 D_d/\sigma, \tag{2.10}$$

where in our case

$$V_c = \sqrt{(u_c-u_d)^2 + (v_c-v_d)^2 + (w_c-w_d)^2}, \tag{2.11}$$

the authors correlated the data for the breakup period in the form

$$\Delta\tau^*_{br} = c\,(We_c-We_{d\infty})^m \quad \text{for } We^*_c < We_c \leq We^{**}_c, \tag{2.12}$$

where the dimensionless time $\Delta\tau^*_{br}$ was defined as

$$\Delta\tau^*_{br} = \Delta\tau_{br}/[D_d(\rho_d/\rho_c)^{1/2}/V_c], \tag{2.13}$$

the critical Weber number is $We_{d\infty} = 12$, and the constants are

| c | m | $We^*_c$ | $We^{**}_c$ |
|---|---|---|---|
| 6 | −1/4 | 12 | 18 |
| 2.45 | +1/4 | 18 | 45 |
| 14.1 | −1/4 | 45 | 351 |
| 0.766 | +1/4 | 351 | 2670 |
| 5.5 | 0 | 2670 | ∞ |

The fragmentation cloud velocity that is reached when all breakup process are complete was correlated by a modified solution of the simple force balance equation, namely

$$(V_c - V_{d\infty})^2 = V_c^2 \{1 - (\rho_c/\rho_d)^{1/2} [c^d_{cd} \Delta\tau^*_{br} + 3\, b\, \Delta\tau^{*2}_{br}]\}^2 \tag{2.14}$$

where $c^d_{cd} = 0.5$, $b = 0.0758$ for incompressible flow ($Ma < 0.1$), and $c^d_{cd} = 1$ , $b = 0.116$ for compressible flow ($Ma > 0.1$).

For liquid–liquid systems they used the not modified solution

$$(V_c - V_{d\infty})^2 = V_c^2 \{1 - (\rho_c/\rho_d)^{1/2} (\tfrac{3}{4} c^d_{cd} \Delta\tau^*_{br})/[1 + \tfrac{3}{4} c^d_{cd}\, \Delta\tau^*_{br} (\rho_c/\rho_d)^{1/2}]\}^2 \tag{2.15}$$

Analogously to the jets, we distinguish for liquid metal drops in film boiling two different disintegration modes: for thin and thick vapor films.

The agglomerated particles per unit time and unit volume are defined in IVA3 as

$$\frac{dn_d}{d\tau} = -\dot{n}_{dcoal} = -f_{dcoal} n_d/2, \tag{2.16}$$

where $f_{dcoal}$ is the coalescence frequency of single particle with dimensions $s^{-1}$. $\dot{n}_{dcoal}$ is the instantaneous coalescence rate. The number of particles per unit volume remaining after the time interval $\Delta\tau$ is easily obtained after integration of the above equation

$$n_{d,\tau+\Delta\tau} = n_d\, e^{-f_{dcoal}\Delta\tau/2}. \tag{2.17}$$

The time averaged coalescence rate is therefore

$$\dot{n}_{dcoal} = \frac{n_d - n_{d,\tau+\Delta\tau}}{\Delta\tau} = n_d(1 - e^{-f_{dcoal}\Delta\tau/2})/\Delta\tau. \tag{2.18}$$

Not necessarily each collision leads to coalescence. The coalescence frequency of single particle is usually defined as the product of the collision frequency, $f_{dcol}$, of single particle and the coalescence probability, $f^p_{dcoal}$,

$$f_{dcoal} = f_{dcol} f^p_{dcoal}. \tag{2.19}$$

From the analogy to molecular kinetic theory, if the particles are assumed to possess Maxwellian distribution of relative speed, the collision frequency of a single particle is

$$f_{dcol} = (\tfrac{1}{2})^{1/2}\, n_d\, \pi D_d^2\, V^{rel} = (\tfrac{1}{2})^{1/2}\, \frac{6\,\alpha_d}{D_d}\, V^{rel}, \quad \text{Rohsenow and Choi [47] (1961),} \tag{2.20}$$

where $V^{rel}$ is the relative velocity between particles.

Obviously the analogy to molecular kinetic theory does not hold for collisions of real liquid droplets because droplets are deformable, elastic, and may agglomerate after random collisions. Howart [49] (1967) obtained a modified form of equation 2.19 which includes additionally the multiplier $2/(3\alpha_d)^{1/2}$, namely

$$f_{dcol} = (\tfrac{1}{2})^{1/2}\, \frac{6\,\alpha_d}{D_d}\, V^{rel}\, 2/(3\alpha_d)^{1/2} = 24^{1/2}\, \frac{\alpha_d^{1/2}}{D_d}\, V^{rel}. \tag{2.21}$$

The dependence of the collision frequency on $\approx \alpha_d^m$ is confirmed by experiments as follows. For droplets – Howarth [50] (1967) $\approx \alpha_d^{0.6}$, for liquid – liquid droplets Coulaloglu and Tavlarides [51] (1976), Madden [52] (1962), Komasawa et al [53] (1969) $\approx \alpha_d^{0.45}$, and for bubbles Sztatecsny et al. [54] (1977) $\approx \alpha_d^{0.6}$

The collision frequency is not an independent function of the coalescence probability. The functional relationship is not known. That is why some authors correct the collision frequency by a constant less than one estimated by comparison with experiments, e.g. Rosenzweig et al [50] (1980) for relatively low $V^{rel}$ and non oscillatory coalescence gives const = 0.0001. We use in IVA3 $f_{dcoal}^p \approx 0.0001$ for particles and $f_{dcoal}^p \approx 0.0064$ for bubbles.

Obviously agglomeration can take place only if the relative particle – particle velocity $V^{rel}$ is different from zero. The nature of $V^{rel}$ depends (a) on the turbulent fluctuation of the particles, (b) on the difference of the relative velocities caused by the differences of the particle size , and (c) on the nonuniform velocity field. Even when using an averaged particle size, the second and the third component may differ from zero. We call the coalescence caused by reasons (a), (b), and (c), oscillatory, spectral, and nonoscillatory coalescence, respectively. For the oscillatory coalescence the driving force moving the particles is due to the oscillating turbulent eddies and therefore pushes continuum between two particles and moves the particles apart (under some circumstances before they coalesce). For the spectral and the nonoscillatory coalescence, the forces leading to collisions inevitably act towards coalescence. For the time being only the nonoscillatory coalescence is taken into account in IVA3 so that

$$V_d^{rel} = \Delta V_{dd}^{no} \approx [(\Delta r\, \frac{\partial u_d}{\partial r})^2 + (\Delta\theta\, \frac{\partial v_d}{\partial \theta})^2 + (\Delta z\, \frac{\partial w_d}{\partial y})^2]^{1/2}. \tag{2.22}$$

Thermodynamic sources, i.e. origin of particles from nuclei in metastable conditions, are modelled by heterogeneous nucleation theories and a delayed start of the nucleation governed by pressure gradients for fields containing microscopic solid particles and/or dissolved gases and by homogeneous nucleation theories for pure metastable fields. So the particle production or disappearance is governed by the local mechanical and thermodynamic conditions in the cell besides convection.

Having identified the flow structure or pattern and the particle number density for each velocity field, IVA3 proceeds further with the computation of the source terms for the macroscopic conservation equations for each velocity field, mass production rates, energy transfer rates, and forces among the fields, and between the fields and walls, if any.

# 3. FORCES

## 3.1 FLUID STRUCTURE

Generally the momentum equations for IVA3 contain two coexisting groups of terms defining the shear stress (a) due to viscous forces in a pool and (b) due to wall friction in flow in confined geometry. For coarse mesh discretization the diffusive terms practically do not effect the flow. The interaction with the walls is modelled by computing the friction pressure loss in the given direction using equivalent hydraulic diameters, mesh sizes, and the mass flow rates in the particular direction. Friction pressure loss coefficients for one phase flows, $\lambda = \lambda(\mathrm{Re}, \delta/\mathrm{D_h})$, as a function of the Reynolds number, Re, and the relative sand roughness grain size of the structure walls, $\delta/\mathrm{D_h}$, are computed using analytical approximations to the Nikuradze–diagram for technical roughness as summarized by Idelchick [28] (1975).

Empirical correlations for two–phase friction multipliers are used in this case because of lack of a better choice. Following the proposal of Hewitt made in [3] (1982), we use Friedel's correlation [29] (1979) for $\eta_2/\eta_1 < 1000$, the Baroczy correlation (1965) as modified by Chisholm (1982) for $\eta_2/\eta_1 \geq 10$ and $\rho w = \Sigma \alpha_l \rho_l w_l > 100$, and the correlation of Martinelli – Nelson [30] (1949) for $\eta_2/\eta_1 \geq 1000$ and $\rho w \leq 100$.

In pool flow, the wall friction term does not influence the flow due to an artificially large defined hydraulic diameter. Real viscous effects for pool flows are modelled automatically only if the resolution of the discretization net is fine enough for the particular problem of interest.

## 3.2 DRAG FORCES

Drag forces between the velocity fields are computed in each flow direction as a function of the length scale of the velocity field and the relative velocity using a set of empirical correlations. Some of the correlations have originally obtained experimentally for pure two–fluid regimes e.g. droplet – gas, droplet – liquid, bubble – liquid, particle – continuum etc., and corrected in order to take into account the presence of the third velocity field using geometrical considerations. Some of the correlations developed for the pressure loss of liquid–gas mixtures in porous structures are directly extended to three phase flows in case macroscopic solid particles constitute the third velocity field and are touching each other (maximum packing density). In this case, the relative velocities between gas and particles and liquid and particles are used to compute the corresponding drag coefficients.

For pure two–phase mixtures we use the analytical approximations proposed by Ishii and Chawla [31] (1979). This set was extended to three–phase flows by Kolev, Tomiyama and Sakaguchi in [32] (1991) and checked the extension extensively against newly obtained experimental data for gas–liquid two–phase flow, liquid solid two–phase, flow and gas–liquid–solid three–phase bubble flow – see Fig. 2. Details of this comparison are presented in [32] (1991) and will not be repeated here. The agreement between the

IVA3 predictions and the data shows the ability of the IVA3 drag models to successfully predict the drag forces in two– and three–phase flows and the correctness of the numerical modelling technique incorporated in the code, the so–called partial decoupling of the velocity fields.

The interfacial *drag force reflects the interactions among the velocity fields.* The force acting on one particle of the velocity field d surrounded by velocity field c multiplied by the number of particles per unit volume is computed in IVA3 as follows

$$f^d_{cd} = -\alpha_d \rho_c \frac{1}{D_d} \frac{3}{4} c^d_{cd} |V_c - V_d| (V_c - V_d). \qquad (3.1)$$

In IVA3 we calculate the drag coefficient for a family of particles in continuum using the Ishii and Chawla [31] (1975) relationships as for a single particle, changing properly only the *effective continuum viscosity* $\eta_m$ as a function of the volume concentration of the disperse phase $\alpha_d$ and the *maximum packing* $\alpha_{dm}$ (c=continuum).

For computation of the drag coefficient for a *gas–liquid* system *in a pool* ($D_{hy} >> D_1$) we assume that the bubbles are completely surrounded by the continuum and that bubbles and continuous liquid are one mixture which flows through the fictitious channel volume fraction $\alpha_1 + \alpha_2$. The bubble concentration in this fictitious channel is $\alpha_d = \alpha_1/(\alpha_1+\alpha_2)$. For the *Stokes regime* in which $(2/3) D_1 \sqrt{g\Delta\rho_{21}/\sigma} < (1-\alpha_d)^{0.6}\ 24/Re$, where $Re = D_1 \rho_2 |\Delta V_{12}| / \eta_m$, $\eta_m = \eta_2/(1-\alpha_d)$, the drag force is

$$f^d_{21} = -(18\ \alpha_d \eta_m / D_1^2)\ (V_2 - V_1)\ . \qquad (3.2)$$

For the *viscous regime* in which $(2/3)\ D_1 \sqrt{g\Delta\rho_{21}/\sigma} < (1-\alpha_d)^{0.6}\ (1+0.1Re^{0.75})\ 24/Re$, the drag force is

$$f^d_{21} = -(18\ \alpha_d \eta_m / D_1^2)(1 + 0.1\ Re^{0.75})\ (V_2 - V_1). \qquad (3.3)$$

For the *distorted* bubble regime in which $(1-\alpha_d)^{0.6}\ (1+0.1Re^{0.75})\ 24/Re \le (2/3) D_1 \sqrt{g\Delta\rho_{21}/\sigma} < (8/3)\ (1-\alpha_d)^{0.87}$, the drag force is

$$f^d_{21} = -0.5\ \alpha_d \rho_2 \sqrt{g\Delta\rho_{21}/\sigma}\ \left(\frac{1+17.67\ f^{6/7}}{18.67\ f}\right)^2 |V_2 - V_1|\ (V_2 - V_1),\quad f = (1-\alpha_d)^{1.5}. \qquad (3.4)$$

For strongly deformed *cap bubbles*, i.e. $(2/3)\ D_1 \sqrt{g\Delta\rho_{21}/\sigma} \ge (8/3)(1-\alpha_d)^{0.87}$, the drag force is

$$f_{21}^d = -[2\,\alpha_d(1-\alpha_d)^2\rho_2/D_1]\,|V_2-V_1|(V_2-V_1). \tag{3.5}$$

For a flow in a pool, this regime also exists, for $\alpha_d > 0.3$. Besides the above mentioned regimes in pool flow, for flow in confined geometry there are three more kinds of interaction between gas and continuous liquid namely *churn turbulent, slug*, and *film flows.* The identification of these regimes is discussed in Section 1. For the *churn turbulent flow,* the drag coefficient is calculated as for the previously discussed cap bubble regime. The drag force for *slug flow* is

$$f_{21}^d = -[7.35\,\alpha_d(1-\alpha_d)^3\rho_2/D_1]\,|V_2-V_1|(V_2-V_1), \tag{3.6}$$

where $D_1 = 0.9\,D_h$.

The drag force acting on a film in a *fully developed annular flow* is calculated using Barathan's correlation as improved by Stephan and Mayinger [65] (1990)

$$f_{12}^d = -a_{12}\,\rho_1\,c_{12}^d\,\tfrac{1}{2}|V_2-V_1|\,(V_2-V_1), \tag{3.7}$$

where $a_{12} = (4/D_h)\sqrt{1-\alpha_2}$, $c_{u1}^d = (0.079/Re_1^{1/4})\,(1 + 115\,\delta^{*B})$, $Re_1 = \rho_1 w_1 D_h/\eta_1$, $B = 3.91/(1.8 + 3/D^*)$, $\delta^* = \delta_2\,[g(\rho_2-\rho_1)/\sigma]^{1/2}$, $\delta_2 = D_h\,(1 - \sqrt{1-\alpha_2}\,)/2$, $D^* = D_h\,[g(\rho_2-\rho_1)/\sigma]^{1/2}$.

Next we will show how the drag force for a *droplet–gas* system in a pool ($D_h >> D_3$) is computed according to the recommendation of Ishii and Chawla. Again if solid particles participate in the flow we consider the gas–droplet flow as flowing in a fictitious channel with volume fraction $\alpha_1+\alpha_3$ of the total control volume and the volume fraction of the droplets in this channel is $\alpha_d = \alpha_3/(\alpha_1+\alpha_3)$. The effective viscosity for this case is $\eta_m = \eta_1/(1-\alpha_d)^{2.5}$. The drag force for the Stokes regime ($Re < 1$, $Re = D_3\rho_1\Delta V_{13}/\eta_m$), is

$$f_{13}^d = -(18\,\alpha_d\eta_m/D_3^2)\,(V_1-V_3). \tag{3.8}$$

The drag force for the viscous regime ($1 \le Re < 1000$) is

$$f_{13}^d = -(18\,\alpha_d\eta_m/D_3^2)(1 + 0.1\,Re^{0.75})\,(V_1-V_3). \tag{3.9}$$

The drag force for Newton's regime ($Re \ge 1000$) is

$$f_{13}^d = -0.5\,\alpha_d\rho_1\sqrt{g\Delta\rho_{31}/\sigma}\,\left(\frac{1+17.67\,f^{6/7}}{18.67\,f}\right)^2 |V_1-V_3|(V_1-V_3), \quad f=(1-\alpha_d)^3.$$

(3.10)

Depending on the volumetric concentration of the macroscopic solid particles (the third velocity field) we distinguish the following cases: (1) the solid particles are touching each other in the control volume, $\alpha_3 = \alpha_{dm}$, and (2) the solid particles are free in the flow $\alpha_3 < \alpha_{dm}$. In the second case we distinguish two sub–cases: (2a) the volume fraction of the space among the particles if they were closely packed, $\alpha_2^* = \alpha_3(1-\alpha_{dm})/\alpha_{dm}$, is smaller then the liquid volume fraction $\alpha_2^* < \alpha_2$; (2b) the volume fraction of the space among the particles if they were closely packed is larger then the liquid volume fraction $\alpha_3 > \alpha_2$. In the second case of solid particles free in the flow good experimental support is available for description of the two phase regimes: solid particles/gas, (31), or solid particles/liquid (32). We use further the notation discrete (d)/ continuous (c) where d=3 and c can take values 1 and 2. Following Ishii and Chawla we have in case of $\alpha_c + \alpha_d = 1$: For the Stokes regime (Re $\leq$ 1) the drag force is

$$f_{cd}^d = -(18\ \alpha_d \eta_m / D_d^2)\ (V_c - V_d), \tag{3.11}$$

where $Re = D_d \rho_c |\Delta V_{cd}| / \eta_m$, $\eta_m = \eta_c/(1 - \alpha_d/\alpha_{dm})^{1.55}$, $\alpha_{dm} = 0.62$. For the viscous regime (1 $\leq$ Re < 1000) the drag force is

$$f_{cd}^d = -(18\ \alpha_d \eta_m / D_d^2)(1 + 0.1\ Re^{0.75})\ (V_c - V_d). \tag{3.12}$$

For Newton's regime (Re $\geq$ 1000) the drag force is

$$f_{cd}^d = -(0.3375\ \alpha_d \rho_c / D_d)\ (\frac{1+17.67\ f^{6/7}}{18.67\ f})^2\ |V_c - V_d|(V_c - V_d) \quad f = \sqrt{1-\alpha_d}\ \eta_c/\eta_m. \tag{3.13}$$

In case of densely packed solid particles or porous liquid metal ($\alpha_3 \geq 0.72$) we use the correlation proposed by Ergun [33] (1952) to compute the drag force between particles and the surrounding continuum

$$f_{13}^d = -\alpha_l\ [150\ (\frac{\alpha_3}{1-\alpha_3})^2\ \frac{\eta_1}{D_3^2} + 1.75\ \frac{\alpha_3}{1-\alpha_3}\ \frac{\rho_1 |\Delta V_{13}|}{D_3}]\ (V_1 - V_3). \tag{3.14}$$

where l=1 or 2, $D_3 = 6/[F_3/(V\alpha_3)]$, $F_3$ is the total geometrical surface of the solid particles in the volume V of the mixture consisting of phase 1 and phase 3.

The case in which the free particles are part of a solid/liquid/gas mixture is more complicated. Consider first the *bubbly three–phase flow.* As a first approximation we can assume that if the bubbles in the space among the particles are touching each other

$[\alpha_1/(\alpha_1+\alpha_2) > 0.52]$ the bubbly three–phase flow cannot exist and vice versa, if $\alpha_1/(\alpha_1+\alpha_2) < 0.52$, the bubbly three–phase flow assumed. For the time being, no experimental information is available to confirm the value 0.52. In any case if three–phase bubble flow is identified we distinguish two sub–cases. If the volume fraction of the space among the particles if they were closely packed is smaller than the liquid fraction $\alpha_2^* < \alpha_2$, the theoretical possibility exists that the particles are carried totally by the liquid and the mixture is considered as consisting of gas and liquid/solid continuum. The drag force between gas and solid is zero and the drag force between solid and liquid is computed with $\alpha_d = \alpha_3/(\alpha_2+\alpha_3)$ and $\Delta V_{dl} = V_3-V_2$. If the volume fraction of the space among the particles if they were closely packed is larger then the liquid volume fraction $\alpha_2^* > \alpha_2$, only $\alpha_3 - \alpha_2\alpha_{dm}/(1-\alpha_{dm}) = \alpha_3\,(1-\alpha_2/\alpha_2^*) = \alpha_{31}$ are surrounded by gas. So we compute the drag and the virtual mass force between one single solid particle and gas as for a mixture $\alpha_1+\alpha_{31}$, $\alpha_d = \alpha_{31}/(\alpha_1+\alpha_{31})$, $\Delta V_{dc} = V_3-V_c$, namely $f^d_{13o} = f^d_{cd}(\alpha_d, \Delta V_{dc},\ldots)$, $f^{vm}_{13o} = f^{vm}_{cd}(\alpha_d, \Delta V_{dc},\ldots)$, and multiply this force by the number of particles which are surrounded by gas and have volumetric fraction $\alpha_{31}$. The result is $f^d_{13} = \alpha_{31}f^d_{13o}$, $c^{vm}_{13} = \alpha_{31}f^{vm}_{13o}$. The same is done in the calculation of the force between one single solid particle and liquid for the mixture $\alpha_2+\alpha_{32}$, $\alpha_d = \alpha_{32}/(\alpha_2+\alpha_{32})$, $\Delta V_{dc} = V_3-V_2$, namely $f^d_{23o} = f^d_{cd}(\alpha_d, \Delta V_{dc},\ldots)$, $f^{vm}_{23o} = f^{vm}_{cd}(\alpha_d, \Delta V_{dc},\ldots)$, where $\alpha_{32} = \alpha_3-\alpha_{31} = \alpha_3\alpha_2/\alpha_2^*$ and again this force is multiplied by the number of the particles which are surrounded by liquid $\alpha_{32}$, $f^d_{23} = \alpha_{32}f^d_{23o}$, $f^{vm}_{23} = \alpha_{32}f^{vm}_{23o}$.

In case that the bubbles in the space are touching each other, i.e. $\alpha_1/(\alpha_1+\alpha_2) > 0.52$, the more likely flow pattern is *three phase disperse flow*. In this case the gas – liquid flow relative to the solid particles resembles two–phase gas–liquid flow in a channel. Therefore the drag forces exerted by the solid particles are larger than drag forces exerted by the solid phase in case of missing liquid. Thus we correct the drag force coefficients in the following waz: $f^d_{13} = (1-\phi)\, f^d_{13o}$, $f^{vm}_{13} = (1-\phi)\, f^{vm}_{13o}$, $f^d_{23} = \phi\, f^d_{23o}$, $f^{vm}_{23} = \phi\, f^{vm}_{23o}$, where $\phi = \alpha_2/(\alpha_1+\alpha_2)$.

# 4. HEAT AND MASS TRANSFER

The main problems in modelling physical processes in the real macro–world is how to transfer and incorporate the knowledge already obtained for the microscopic process in the micro–world because nature does not distinguish them. The distinction is conditionally introduced by the scientists and therefore subjective. There are no principles governing both groups of processes besides conservation of mass, momentum, and energy. For the microscopic processes like evaporation, condensation, etc. solutions of basic conservation equations for the particular geometry, e.g. bubble growth in superheated liquid, that are proved or corrected by experimental data of separate effect tests, are used in the macroscopic model. This step is accomplished by time and volume averaging of the source terms over the computational cell. The time averaging of the source terms is an important feature of IVA3. It was necessary because the time scales of both groups of processes are normally in the rule different and must be synchronized. Either one should integrate the system of macroscopic governing equations with the smallest time step dictated from the fastest micro–process or one should use the time step dictated by stability analysis of the numerical methods used and integrate the source terms over the time step. The first method needs much bigger computing resources than are available nowadays. That is why IVA3 exploits the second one. The second method even provides smooth transition. If one simply reduces the time steps one obtains the instantaneous values of the source terms. This technique also greatly stabilizes and speeds up the numerical solution.

IVA3 provides closure models for heat, mass, and momentum transfer mechanisms divided into five groups: (a) droplets, (b) bubbles, (c) films, (d) solid particles, (e) heated surfaces. For the first two groups, IVA3 distinguishes between a kinematic or not kinematic origin of the velocity field as already described in the previous section. If the phases already exist, IVA3 distinguishes for the first three regimes among the following heat and mass transfer modes: (a) convective heat transfer, (b) flashing, (c) evaporation into a two–component atmosphere, (d) condensation of pure steam, (e) condensation from steam–air mixtures. For the solid particles, IVA3 models (a) convective and (b) radiative heat transfer, (c) nucleate, and (d) film boiling in liquid. For the heated surfaces, IVA3 provides complete heat transfer mechanism characteristics for a nuclear reactor core at all conditions in addition to transient one– or two–dimensional heat conduction in the fuel rod. The time and space dependence of the heat generation per unit fuel volume is defined as a boundary condition initially.

In what follows we summarize the main features of the different heat and mass transfer constitutive models.

(a) Droplets (all models for heat and mass transfer are subsequently time averaged):

– Convective heat transfer (no conditions for evaporation or condensation), Ranz and Marshal [13] (1952).

$$\dot{q}''_{13} = (6\alpha_3/D_3)\,\frac{\lambda_1}{D_3}\,[2 + 0.6\,(\frac{D_3\rho_1\Delta V_{31}}{\eta_1})^{1/2}\,(\frac{\eta_1 c_{p1}}{\lambda_1})^{1/3}]\,(T_1 - T_3). \tag{4.1}$$

– The spontaneously evaporating mass from the superheated third velocity field (flashing) per unit mixture volume is

$$\mu_{31} = (6\alpha_3/D_3)\,(\rho w)_{31}\,f, \tag{4.2}$$

where

$$(\rho w)_{31} = \frac{2c}{2-c}\,\frac{1}{\sqrt{2\pi R_{M1} T_3^o}}\,[p'(T_3^o) - p_{M1} - \frac{p'(T_3^o)}{2T_3^o}\,(T_3^o - T_1)] \tag{4.3}$$

is the Hetz – Knudsen – Langmuier equation, see in Rhosenow et al [4] (1981) with $c_{H_2O}$ $= 0.01 \div 1$ as *accommodation coefficient.* From the energy jump condition at the surface we have

$$\dot{q}''_{i3} = -\mu_{31}[h''(p) - h_{M3}], \tag{4.4}$$

and $\mu_{13} = 0$, $\dot{q}''_{3i} = 0$. The correction factor f results from averaging the resulting heat source term over the time interval $\Delta\tau$:

$$f = \frac{\Delta\tau_3^*}{\Delta\tau}\,(1 - e^{-\Delta\tau/\Delta\tau^*}) < 1 \quad \Delta\tau > 0. \tag{4.5}$$

where

$$\Delta\tau_3^* = \frac{D_3\rho_3 c_{p3}}{6(\rho w)_{31}}\,\frac{T_3 - T'}{h'' - h_{M3}} \tag{4.6}$$

is the *characteristic time constant of the process.*

– The evaporation into, $(\rho w)_{31} > 0$, and condensation from, $(\rho w)_{31} < 0$, a two component atmosphere

$$\mu_{31} = (6\alpha_3/D_3)\,(\rho w)_{31}, \quad \mu_{13} = 0, \tag{4.7}$$

$$\mu_{13} = -(6\alpha_3/D_3)\,(\rho w)_{31}, \quad \mu_{31} = 0, \tag{4.8}$$

is assumed to be diffusion controlled

$$(\rho w)_{31} = \rho_1\,\beta\,(C_{M1i} - C_{M1})\,f. \tag{4.9}$$

Here the mass transfer coefficient $\beta$ is computed in acordance with Renz and Marshall [13] (1952) and Tanaka [15] (1980) as

$$\beta = \frac{D_{M\to n}}{D_3}\{2 + 0.6\,(\rho_1 D_1 \Delta V_{13}/\eta_1)^{1/2}\,[\eta_1/(\rho_1 D_{M\to n})]^{1/3}\}\,1.39\,\frac{(\frac{C_{n1i}}{C_{n1}})^{0.52}}{(1+\frac{C_{n1}}{C_{n1i}})^{0.48}C_{n1}},$$

(4.10)

$C_{M1i} = \rho_{M1i}/(\rho_{n1i} + \rho_{M1i}) = 1/(1 + \rho_{n1i}/\rho_{M1i})$, $T_{3i} \approx T_3$, $\rho_{M1i} = \rho''(T_{3i})$, $\rho_{n1i} = [p - p'(T_{3i})]/(R_{n1}T_{3i})$, $R_{n1} = 287.04$ for air. The correction f results from averaging the resulting mass source term over the time interval $\Delta\tau$:

$$f = \frac{1}{1-C_o}\{1-\frac{1}{\Delta\bar{\tau}}\ln[1 - C_o(1 - e^{\Delta\bar{\tau}})]\} \le 1, \tag{4.11}$$

$$\Delta\bar{\tau} = \Delta\tau\,(6\alpha_3/D_3)\,\beta\,C_{n1i}/\alpha_1, \tag{4.12}$$

$$C_o = C_{n1}/C_{n1i}. \tag{4.13}$$

Having in mind that during evaporation, $\dot{q}''_{31i} = 0$, we obtain the heat extracted from the droplet per unit mixture volume and unit time from the energy jump condition

$$\dot{q}''_{i3} = -\mu_{31}[h''(p) - h_{M3}]. \tag{4.14}$$

For condensation we have

$$\dot{q}''_{i3} = \mu_{13}[h''(p) - h_{M3}]. \tag{4.15}$$

– Condensation of pure steam is modeled using the model proposed by Dhir and Lienhard [14] (1972). The heat released during condensation which is transported into the droplet by heat conduction is computed as follows:

$$\dot{q}''_{i3} = (6\alpha_3/D_3)\,\frac{\lambda'}{D_3}\,Nu_{lam}\,(T' - T_3)\,f, \tag{4.16}$$

where

$$Nu_{lam} = 0.785\,\{\frac{g\rho'(\rho'' - \rho')[h'' - h' + 0.65c_{p3}(T' - T_{3i})]D_3^3}{\lambda'\eta'(T' - T_{3i})}\}^{1/4}. \tag{4.17}$$

with $T_3 = T_{3i}$. Having in mind that $\mu_{31} = 0$, $\dot{q}''_{31i} = 0$, we obtain the condensing mass per unit volume of the mixture and per unit time from the energy jump condition on the

droplet surface:

$$\mu_{13} = \dot{q}''_{i3}/[h_{M1} - h'(p)]. \tag{4.18}$$

The correction factor f results from averaging the resulting heat source term over the time interval $\Delta\tau$:

$$f = \frac{\Delta\tau_3^*}{\Delta\tau}(1 - e^{-\Delta\tau/\Delta\tau_3^*}) < 1 \quad \Delta\tau > 0, \tag{4.19}$$

where

$$\Delta\tau_3^* = \frac{D_3\rho_3 c_{p3}}{6\alpha_c}\frac{h_{M1} - h'}{h_{M1} - h_3}. \tag{4.20}$$

(b) Bubbles (all models for heat and mass transfer are subsequently time averaged):

– Convective heat transfer: If there is no evaporation or condensation, the heat transported by *convection* between a bubble and the surrounding liquid is computed using the Nigmatulin [16] (1978) result

$$\dot{q}''_{12} = (6\alpha_1/D_1)\,\alpha_c\,(T_{1i} - T_2), \tag{4.21}$$

where $\alpha_c = [2 + 0.65\ Pe_2^{1.7}/(1+Pe_2^{1.3})]\ \lambda_2/D_1$, $Pe_2 = D_1\rho_2|w_1 - w_2|c_{p2}/\lambda_2$. The surface temperature $T_{1i}$ is calculated under the assumption that the heat transfer from the bubble to the surface due to natural convection equals the heat transfer from the surface into the bulk liquid

$$T_{1i} = (\alpha_c T_1 + \alpha_{NC} T_2)/(\alpha_c + \alpha_{NC}) \tag{4.22}$$

where

$$\alpha_{NC} \approx \text{cons}\,\frac{\lambda_1}{D_1}(Gr_1 Pr_1)^m = \text{cons}\,\frac{\lambda_1}{D_1}\{[g(\rho_1 - \rho_{1i})\rho_1 D_1^3/\eta_1^2](\eta_1 c_{p1}/\lambda_1)\}^m, \tag{4.23}$$

is the heat transfer coefficient due to natural convection in a cavity see Holman [26] (1972). Here we have $\rho_{1i} = \rho_{1i}(p, T_{1i})$, const $\approx 0.59 \div 0.9$, $m \approx 1/4$.

– Flashing: For a constant number of bubbles during the time step, the *volume difference* between the end and the beginning of the time step *multiplied* by the *steam density* and the *bubble number per unit mixture volume*, gives the *integral mass evaporating* during the considered time step per unit mixture volume. Dividing this mass by the time step we

obtain the averaged mass source term

$$\mu_{21} = \rho'' n_{1o} V_{1cr}/\Delta\tau \qquad \alpha_1=0 \tag{4.24}$$

for the first integration step in which the bubble growth starts and

$$\mu_{21} = \frac{\rho''\alpha_{1o}}{\Delta\tau}[(R_1/R_{1o})^3-1] \quad \alpha_1>0 \tag{4.25}$$

for the next time steps. For the third power of the ratio of the radii at the end and at the beginning of the time step we have from the Labunzov [17] (1964) equation

$$r_1 = f\sqrt{a_2\tau^*} \tag{4.26}$$

the following result

$$R_1/R_{1o} = (1 + \Delta\tau/\tau^*)^{1/2}, \tag{4.27}$$

where $f = 2(\frac{3}{\pi})^{1/2}\,Ja\,[1 + \frac{1}{2}(\frac{\pi}{6Ja})^{2/3} + \frac{\pi}{6Ja}]^{1/2}$, $a_2 = \frac{\lambda_2}{\rho_2 c_{p2}}$, and $Ja = \frac{\rho_2 c_{p2}(T_2-T')}{\rho''(h''-h')}$. The time interval measured from the beginning of the bubble growth to the beginning of the time step, can easily be calculated

$$\tau^* = (\frac{3\alpha_1}{4\pi n_1})^{2/3}/(a_2 f^2). \tag{4.28}$$

Having in mind that for spontaneous evaporation we have $\mu_{12} = 0$, $\dot{q}''_{2i} = 0$, we obtain the corresponding energy source term

$$\dot{q}''_{i2} = -\mu_{21}[h''(p)-h_{M2}] \tag{4.29}$$

from the energy jump condition on the bubble surface.

– Evaporation into a two–component atmosphere: thermal controlled, Labunzov [17] (1964) with $T'(p_{M1})$ instead T'.

– Condensation of pure steam: The integral expression for the averaged condensation within $\Delta\tau$ is

$$\mu_{12} = \frac{\rho''\alpha_1}{\Delta\tau}[1-(R_1/R_{1o})^3], \qquad \Delta\tau < \Delta\tau_o, \tag{4.30}$$

$$\mu_{12} = \rho''\alpha_1/\Delta\tau \qquad \Delta\tau \geq \Delta\tau_o. \tag{4.31}$$

The last relationship is practically the condition for the total condensation of the available steam within the time step considered. For small $\Delta V_{12}$ we use Nu=2 and

$$R_1/R_{1o} = (1 - Fo/Fo_o)^{1/2}, \tag{4.32}$$

where $Fo = a_2\tau/R_{1o}^2$ and $Fo_o = 1/(Nu_1 Ja)$. For moving bubbles we have

$$R_1/R_{1o} = (1 - Fo/Fo_o)^{2/3}, \tag{4.33}$$

where $Fo_o = 1/(0.423\ Re_{1o}^{1/2}\ Pr_2^{1/3}\ Ja)$, $Re_{1o} = \frac{D_{1o}\rho_2\Delta V_{12}}{\eta_2}$, $Ja = \frac{\rho_2 c_{p2}(T_2'-T_2)}{\rho''(h''-h')}$, $Pr_2 = \frac{\eta_2}{\rho_2 a_2}$, $a_2 = \frac{\lambda_2}{\rho_2 c_{p2}}$ – see Hunt [18] (1970) and Issenberg [19] (1970). Having in mind that during the condensation $\mu_{21} = 0$ and $\dot{q}''_{2li} = 0$ we obtain the averaged energy source term from the energy jump condition on the bubble surface

$$\dot{q}''_{i2} = \mu_{12}(h_{M1}-h'). \tag{4.34}$$

– Condensation from steam air mixtures is modeled analogeously to that for pure steam with correction of the surface temperature $T_{2i} \approx T'(p_{M1})$.

(c) Film:

– Convective heat transfer: We assume that the film is uniformly distributed on the wetted perimeter in planes perpendicular to the z–direction. The heated and the hydraulic diameters of the "channel" occupied by the gas are $D_{12} = D_h\sqrt{1-\alpha_2}$. The surface area between gas and liquid per unit volume of the mixture is $a_{12} = \frac{4}{D_h}\sqrt{1-\alpha_2}$ and the film thickness is $\delta_2 = D_h\,(1 - \sqrt{1-\alpha_2})/2$. If evaporation and condensation are absend, the heat transported by *convection* per unit time and unit mixture volume is

$$\dot{q}''_{12} = a_{12}\,\frac{\lambda_1}{D_{12}}\,Nu_c\,(T_1-T_2), \tag{4.35}$$

where the *heat transfer coefficient* is

$$Nu_c = 0.021\ Re_1^{0.8}\ Pr_1^{0.4}\ (\frac{T_1}{T_2})^{1/2} \qquad Re_1 > 1450 \text{ Mc Eligot} - \text{see in [20]}, \tag{4.36}$$

and

$$Nu_c = 3.66\,(\frac{T_1}{T_2})^{1/4} \qquad Re_1 \leq 1450 \text{ Hausen} - \text{see in [20]}, \tag{4.37}$$

where $Re_1 = \rho_1 |V_1 - V_2| D_{12}/\eta_1$.

– Flashing: We assume that the *thermal resistance* insides the film has a delaying effect on evaporation, because the heat conduction is the slower process as compared to the mass emission from the surface. The *turbulent heat conduction* in the film can be estimated using the information about *condensation on a turbulent film* as obtained by Sonin, Schimko and Chun [21] (1986)

$$\dot{q}''_{i2}{}' = a_{12}\, 0.0098\, \rho_2 V_2' c_{p2}\, (T' - T_2)\, f, \tag{4.38}$$

where $V_2' \cong 0.1 \div 0.3\ V_2$, $\dot{\mu}_{12} = 0$, $\dot{q}''_{2i}{}' = 0$, and $\dot{\mu}_{21} = -\dot{q}''_{i2}{}'/[h''(p) - h_{M2}]$. In this case the *characteristic time constant* is approximately

$$\Delta\tau_2^* \approx \frac{\alpha_2}{a_{12}\ 0.0098\ V_2'}, \tag{4.39}$$

and the *averaged source terms* within the time step $\Delta\tau$ are computed by multiplying the instantaneous source terms at the beginning of the time step with

$$f = \frac{\Delta\tau_2^*}{\Delta\tau}\,(1 - e^{-\Delta\tau/\Delta\tau_2^*}) < 1 \qquad \Delta\tau > 0. \tag{4.40}$$

– Condensation of pure steam: During the *condensation of pure steam* with a temperature $T_1$ close to the saturation temperature on the surface of a film with an averaged temperature $T_2$ below then the saturation temperature, $T_2 < T'$, the heat released on the surface,

$$\dot{q}''_{i2} = \beta_2 \rho_2 c_{p2} (T' - T_2)\, f \tag{4.41}$$

is entirely *absorbed* by the liquid. Here $\beta_2 = 0.0098\ V_2'$ in accordance with Sonin, Schimko and Chun [21] (1986), $V_2' = 0.1 \div 0.3\ V_2$, f is given by Eq.3.40 and the time constant of the process is

$$\Delta\tau_2^* = \alpha_2 \frac{h_{M1} - h'}{h_{M1} - h_2}/(a_{12}\beta_2). \tag{4.42}$$

From the condition of no energy accumulation on the film surface we obtain $\mu_{21} = 0$, $\dot{q}''_{21i} = 0$ and

$$\mu_{12} = a_{12}\, \dot{q}''_{i2}\, /(h_{M1}-h'). \tag{4.43}$$

– Evaporation into a two–component atmosphere: We assume a diffusion controlled process. The evaporating mass per unit mixture volume and unit time is

$$\mu_{21} = -\, a_{21}\, \alpha_c \frac{M_{M1}}{M_1} \ln \frac{p-p'(T_2)}{p_{n1}} / (c_{p1} Le^{2/3}), \text{ for } p_{M1} < p'(T_2) < p, \tag{4.44}$$

see in [22] (1984), where $Le = \lambda_1/(\rho_1 c_{p1} D_{M\to n})$, $M_1 = M_{n1}\, p_{n1}/p + M_{M1}(p-p_{n1})/p$, ($M_{n1} = 28.96$ for air, $M_{M1} = 18.96$ for water steam). $\alpha_c$ is the convection heat transfer coefficient computed using Eq. 3.36. p' is the partial pressure of the steam in the boundary layer, where the steam is assumed to be saturated at a temperature about equal to the film temperature $p' = p'(T_2)$. The heat extracted from the film during slow evaporation per unit mixture volume and unit time is

$$\dot{q}''_{i2} = -\, \mu_{21}(h''-h_{M2}). \tag{4.45}$$

Further we have $\dot{q}''_{21i} = 0$, $\mu_{12} = 0$.

– Condensation from steam air mixtures: We assume a diffusion controlled process [22] (1984). The *condensing* mass per unit mixture volume and per unit time in case of *existence of noncondensing components* in the gas is $\mu_{12}$ calculated from Eq. 4.34 for $p'(T_2) < p_{M1}$. Here p' is the partial pressure of the steam in the boundary layer where the steam is assumed to be saturated at a temperature equal to the film temperature $p' = p'(T_2)$. The heat released during the condensation

$$\dot{q}''_{i2} = \mu_{12}[h_{M1}-h'(p)] \tag{4.46}$$

is absorbed by the film. Further we have $\dot{q}''_{21i} = 0$, $\mu_{21} = 0$. We take into account the energy transported *convectively* between gas and film

$$\dot{q}''_{12}=a_{12}\alpha_c(T_1-T'_c), \tag{4.47}$$

where $\alpha_c$ is the convective heat transfer coefficient.

(d) Solid particles:

– Convective heat transfer: For a submerged particle the heat transferred from the particle surface into the liquid is computed using Nigmatulin's correlation, [16] (1978)

$$\dot{q}''_{32} = (6\alpha_3/D_3)\ \alpha_c\ (T_3 - T_2)\ f, \tag{4.48}$$

where

$$\alpha_c = \frac{\lambda_2}{D_3}\,[2 + 0.65\ Pe_2^{1.7}/(1+Pe_2^{1.3})], \tag{4.49}$$

$$f = (1 - e^{-\Delta\tau/\Delta\tau^*_3})\ \Delta\tau^*_3/\Delta\tau < 1, \tag{4.50}$$

and

$$\Delta\tau^*_3 \approx \frac{\rho_3 c_{p3} D_3}{6\alpha_c}, \tag{4.51}$$

is the characteristic time constant of the process obtained from the entropy equation neglecting convection and diffusion from neighbouring computational cells.

– Radiative heat transfer: For high solid temperatures the effects of *radiation*

$$\dot{q}''_{i3r} = -(6\alpha_3/D_3)\ k_{SB} E_3\ (T_3^4 - T'^4) \tag{4.52}$$

is added to the *convective boiling* heat transport. Here $k_{SB} = 5.6697\ 10^{-8}$ is the Stefan–Boltzmann constant, and $E_3$ is the emission coefficient for particles in liquid (e.g. $E_3 \approx 0.75$ or including the aspect ratio $E_3 \approx 0.75\ \frac{81}{32}\ (\frac{\sqrt{2}}{2\pi})\ \alpha_2^{2/3} \approx 0.7\ \alpha_2^{2/3}$).

– Nucleate boiling: If the heat transferred due to the nucleate boiling on the surface of the particle

$$\dot{q}''_{i3} = -(6\alpha_3/D_3)\alpha_b(T_3 - T')^2, \tag{4.53}$$

where

$$\alpha_b = 1942\ \exp(p/4.35\ 10^6), \quad \text{Thom see in [23] (1966)}, \tag{4.54}$$

is totally transferred into the bulk of the liquid, which means, $-\dot{q}''_{i3} = \dot{q}''_{i2}$, or $\alpha_b(T_{3b} -$

$T')^2 = \alpha_c(T' - T_2)$ the bubbles totally collapse close to the surface and no effective evaporation is observed. Therefore the surface temperature of the particles must be higher than $T_{3b}$ in order to initiate effective nucleate boiling, where

$$T_{3b} = T' + [\frac{\alpha_c}{\alpha_b}(T' - T_2)]^{1/2}. \tag{4.55}$$

In this case we have

$$\mu_{21} = (-\dot{q}''_{i3} - \dot{q}''_{i2})/(h'' - h'). \tag{4.56}$$

If $T_3 < T_{3B}$ no nucleate boiling takes place, $\dot{q}''_{i3} = 0$, $\dot{q}''_{i2} = 0$, and $\dot{q}''_{32}$ is calculated after Eq. 4.48.

Cooling of particles by nucleate boiling in a saturated liquid is very effective. During the time $\Delta\tau$ the average heat released by the particles per unit mixture volume and unit time is

$$\dot{q}''_{32i} \approx (6\alpha_3/D_3)\ \alpha_b\ (T_{3a}-T')^2\ f^2, \tag{4.57}$$

where

$$f = \{\ln\ [1+ (T_{3a}-T')\Delta\tau/\Delta\tau^*_3]\}/[(T_{3a}-T')\Delta\tau/\Delta\tau^*_3]. \tag{4.58}$$

$$\Delta\tau^*_3 \cong \frac{\rho_3 c_{p3} D_3}{6\alpha_b} \tag{4.59}$$

is the *characteristic time constant* of the process obtained from the entropy equation neglecting convection and diffusion from neighbouring computational cells.

– Film boiling in solid–liquid–bubble flow: The heat transferred from the particle to the liquid by means of nucleate boiling cannot exceed a critical value. Like with heat transfer on heated surfaces this is called departure from nucleate boiling – DNB. In order to identify this boiling regime we use the hydrodynamic model of a *boiling crisis*

$$\dot{q}''_{32cr} \cong (6\alpha_3/D_3)\ 0.14\ (h''-h')\ \sqrt{\rho''}\ [\sigma g(\rho'-\rho'')]^{1/4}\ (\frac{\rho'}{\rho'-\rho''})^{1/2} \tag{4.60}$$

(see Kutateladse [55] p.141). For subcooled liquid we use the Irvey and Morris modification of the Kutateladse correlation

$$\frac{\dot{q}''_{32cr}}{\dot{q}''_{32cr,Ku}} = 1 + 0.1\ (\frac{\rho'}{\rho''})^{1/4}\ \frac{c_{p2}\rho_2(T'-T_2)}{(h''-h')\rho'} \tag{4.61}$$

– see in [56] (1962). For $\dot{q}''_{i3}$ (Eq.3.53) > $\dot{q}''_{32kr}$, or $T_3 > T_{3FB}$, where $T_{3FB} = T' + 101 + 8\,(T'-T_2)$ is the minimum surface temperature needed to support a vapor film, the heat transfer is assumed to be due to film boiling and the following model of Dhir and Purohit [24] (1978) is used.

For heat transfer by natural convection film boiling, $Re_2 < 1200$, $T_{3i} > T_{3imin}$, where $Re_2 = |V_3-V_2|D_3\rho_2/\eta_2$, we have

$$\dot{q}''_{i3} = -(6\alpha_3/D_3)\,[E_3 k_{SB}(T_3^4 - T'^4) + \alpha_{FB}(T_3 - T') + \alpha_C(T' - T_2)] \tag{4.62}$$

where

$$\alpha_{FB} = \alpha_{FB0} = 0.8\,[\frac{g\rho_1(\rho_2-\rho_1)(h''-h')\lambda_1^3}{\eta_1 D_3(T_{3i}-T')}]^{1/4}, \tag{4.63}$$

is the free convection film boiling heat transfer coefficient after Frederking [25] (1964). Additional heat is transported from the saturated surface to the bulk liquid due to natural convection,

$$\dot{q}''_{i2} = (6\alpha_3/D_3)\,\alpha_C(T'-T_2), \tag{4.64}$$

where

$$\alpha_C = \alpha_{NC} = 0.9\,(\frac{g|\rho_2'-\rho_2|\rho_2\lambda_2^3 c_{p2}}{\eta_2 D_3})^{1/4} \tag{4.65}$$

is the heat transfer coefficient for natural convection from the saturated gas film to the bulk liquid. This reduces the evaporation by the amount of the condensed vapor.

For heat transfer by forced convection film boiling, $1\,200 \le Re_2 \le 19\,000$, $T_{3i} < T_{3min}$, we have

$$\alpha_{FB} = \alpha_{FB0} + \frac{\lambda_1}{D_3}\,0.8\,Re_2^{1/2}, \tag{4.66}$$

and

$$\alpha_C = \alpha_{NC} + \frac{\lambda_2}{D_3}\,0.8\,Re_2^{1/2}. \tag{4.67}$$

The evaporating mass per unit mixture volume and unit time is

$$\mu_{21} = (-\dot{q}''_{i3} - q''_{i2})/[h''(p)-h_2)]. \tag{4.68}$$

If the conditions for condensation are not fulfilled, the heat transported from gas to a particle by *convection* per unit time and unit mixture volume is

$$\dot{q}''_{i3} = (6\alpha_3/D_3)\,(\lambda_1/D_3)\,Nu_{13}\,(T_1-T_3), \tag{4.69}$$

where for $Pe_1 < 10^3$ we use Nigmatulin's equation $Nu_{13} = 2 + 0.33\ Pe_1^{0.84}/(1 + 0.33\ Pe_1^{0.51})$, Nigmatulin [16] (1978), and for $Pe_1 < 1$ we use the correlation proposed by Acrivos and Taylor [66] (1965), $Nu_{13} = 2 + 0.5\ Pe_1^{0.33}$. Here $Pe_1 = \Delta V_{13} D_3 \rho_1 c_{p1}/\lambda_1$.

In addition to the above mentioned heat and mass transfer models some topologies are completed with the following models:

(e) Film boiling heat transfer from porous liquid metal to droplets: In case of dispersed flow we assume that the droplets occupy predominantly the space between the particles. In this case the aspect ratio used to compute the radiative heat transfer is used also for estimation of the surface which is exposed to film boiling heat transfer. Thus the following model is used

$$\dot{q}''_{i3} = -(6\alpha_3/D_3)\ 0.57\ \alpha_2^{2/3}\ [0.75\ k_{BS}(T_3^4 - T'^4) + \alpha_{FB}(T - T')], \tag{4.70}$$

with $q''_{i2} = 0$ and $\mu_{21}$ being calculated by Eq. 3.68.

(f) Inverted evaporation of a water drop enclosed in melt: The IVA3 model is based on radiative heat transfer into the drop, $\dot{q}''_{31} = (6\alpha_3/D_3)E_3 k_{BS}(T_3^4 - T_2^4)$, spontaneous evaporation from internal surface, $(\rho w)_{21} \approx c\ [p'(T_2)-p]/\sqrt{2\pi R_{M1} T_1}$, acceleration controlled gas bubble expansion, $(dR_1/d\tau)^2 \approx \frac{2}{3}\ [p'(T_2)-p]/\rho_3$, integrated mass conservation,

$$R_1/R_{1o} = 1/(1 - \Delta\tau/\Delta\tau^*) \tag{4.71}$$

where

$$\Delta\tau^* = [\ \frac{2}{3c}\sqrt{2\pi R_{M1} T_1}\ \frac{\rho_2}{\rho_3(\rho_2-\rho_1)}\ \frac{R_{1o}}{R_2^2}\ ]^{-1} \tag{4.72}$$

is the characteristic time constant of the process, and time averaging of the evaporation

mass source term resulting in

$$\mu_{21} = \frac{\rho''(\alpha_1+\alpha_2)}{\Delta\tau}\left[\left(\frac{R_1}{R_{1o}}\right)^3 - 1\right]. \qquad (4.73)$$

The transient heat conduction model of a nuclear reactor core as well as the flow regime dependent heat transfer models that are based on local conditions remain the same as in the previous IVA2 code – see [27] (1986). For the cases when heat and mass transfer on the heated structure (surface) is identified, superposition of the processes in the bulk flow and the processes at the surface is assumed.

# 5. CODE VALIDATION

Next we simulate five processes. One of them has an exact analytical solution and the other four have been observed experimentally. All of them include dramatical changes of the dependent variables like pressure, velocities and volumetric concentration of the velocity fields in time and space.

## 5.1 THE SHOCK TUBE PROBLEM

The properties of different numerical schemes are usually tested against benchmarks having analytical solution like the widely used shock tube problem: In a tube with constant cross section (in our case 0.01 $m^2$) and length 0.99 m filled with air, a diaphragm at z=0.5 m separates two regions which have different pressures. The two regions are in homogeneous states. The initial conditions are $p(\tau=0,\ z=0\div0.5) = 100\ 10^5$ Pa, $p(\tau=0,\ z=0.5\div0.99) = 50\ 10^5$ Pa, $w(\tau=0,\ z=0\div0.99) = 0$; i.e. the fluid is initially at rest, $T(\tau=0,\ z=0.99) = 326.84$ K. At times $\tau > 0$ the diaphragm is broken. Note that this case is qualitative similar but not identical to the benchmark introduced by Sod [39] (1987). The only difference is the initial temperature which is here assumed constant along the tube.

Consider the case before any wave has reached the left or the right boundaries – Figs. 3 – 8. Theoretically, points $z_1$ and $z_2$ represent the locations of the head and the tail of the rarefaction wave (moving to the left). Although the solution is continuous in this region, some of the derivatives of the fluid quantities may not be continuous. The point $z_3$ is called a contact discontinuity. Across a contact discontinuity, pressure and velocity are continuous, whereas density and specific entropy are not continuous according to theory. Point $z_4$ is the location of the shock wave moving to the right. Across a shock all of the quantities w, p, s, $\rho$ are expected to be discontinuous. The predicted dependent variables pressure, velocity, and specific entropy as functions of space at $\tau = 250$ s are presented in Figs. 3 through 5. Additionally the corresponding temperature, density, and velocity of sound are presented in Figs. 6 through 8. The computation was performed with 50, 100 and 200 discretization points. As expected, the higher the number of the discretization points the better the numerical solution approaches the analytical one. In general we see neither more nor less than the expected behavior of numerical schemes using a first–order donor–cell method for the convective terms and second–order central differences for the diffusion terms. This is a proof of the used strategy of pressure–velocity coupling being all right.

## 5.2 GAS JET EXPANSION

Next we will present three comparisons with experimental data for fast acoustic processes in gas and two–phase mixtures in a complex geometry. The experiments were performed by Meyer and Kirstahler [40,41] (1987,1988).

### 5.2.1 DESCRIPTION OF EXPERIMENT AND IVA3 GEOMETRY REPRESENTATION

The complete description of experimental facility, instrumentation, and experimental procedure is documented in Refs. 40 and 42. Only the important initial and boundary conditions relevant to the simulation are summarized here.

An axisymmetric vessel simulating a geometry of typical fast breeder reactor in 1:20 scale was used. Before starting the experiment, the vessel was divided into high– and low pressure regions by sliding doors. Above the sliding doors an aluminum burst foil separates the low pressure region from the rest of the facility. The high pressure region consists of a 0.6 MPa nitrogen source that simulates the expansion characteristics of hot fuel and sodium in the reactor. The low pressure region consists of degassed water simulating the sodium coolant [air volumetric fraction typically 0.002 to 0.005 (Ref.42)] (see Fig. 9 a through 9 c) and air at p=0.1 MPa and room temperature above the water simulating the cover gas. The low pressure region is transparent. Two high speed film cameras (90 deg apart, 7 frames/ms) were used to record the "bubble growth" from the region at the nozzle entrance. The experiment is initiated by igniting an oxigen–hydrogen gas mixture in the sliding door driving mechanism. The sliding doors are accelerated and open the cross section beginning in the center rapidly within 0,4 ms. The pressure was measured in different positions shown in Fig. 9 a.

The experimental observations show bubble growth, quantitatively measured in Ref.40 p. 868, entrainment of droplets from the "bubble surface" due to instability, and disintegration of the massive liquid after reaching the top and the outer wall into dispersed droplets.

In the computational simulation we assume a symmetrical process, neglecting the asymmetries observed in Ref.40. The geometry was represented by 1144 cells (26x44) in only one angular sector in cylindrical coordinates. Variable surface permeabilities are used to simulate the opening process of the sliding doors. The Poisson like equation was solved for the whole (r, z) plane directly.

One run sumulating about 20 ms physical time (for the two–phase case) takes typically 1 h of CPU time.

### 5.2.2 GAS JET EXPANSION IN GAS WITH INTERNALS

In order to separate the effect that the constitutive equations have on the solutions from the effect of the numerical method used in IVA3, we first simulate an experiment as described in Ch. 5.2.1 with the only difference that instead of being filled with liquid and gas, the low pressure region was filled with gas only. Only the code architecture and the code integrator are addressed in this simulation: no empirical correlation except the state and transport properties of the gas are necessary for this case. Such an experiment was performed in Ref. 41 as a counterpart to the experiment by Meyer and Kirstahler [41]. The

comparison between the predicted and the measured pressures is shown in Figs. 10, 11, and 12. In general IVA3 predicts very well the trends of the pressures at the locations (IVA3: r=0.025, z=0.69175; Exp.: r=0.022, z=0.693), (IVA3: r=0.067, z=0.69175; Exp.: r=0.07, z=0.693), (IVA3: r=0.148, z=0.686; Exp.: r=0.148, z=0.693), respectively. The agreement concerning absolute values of pressure maximum and frequencies is very good during the first 3 seconds. The discrepancy in the period from 6 to 14 seconds is a result of numerical diffusion with the IVA3 method.

### 5.2.3 GAS JET EXPANSION IN LIQUID WITH INTERNALS

Now we repeat the calculation for the same geometry with the same discretization and the same initial and boundary conditions, but with liquid in the low pressure region in the beginning. Figure 13 shows the computed total pressure at the location (r=0.025, z=0.69175) compared with the measured total pressure at the location (r=0.022, z=0.693) on the top. The result for the middle position at the top (IVA3: r=0.067, z=0.69175; Exp.: r=0.07, z=0.693) presented in Fig. 14 is similar. Figure 15 presents the comparison of the pressures at the upper corner (IVA3: r=0.148, z=0.686; Exp.: r=0.148, z=0.693) and on the side wall (IVA3: r=0.112, z=0.1265; Exp.: r=0.1143, z=0.197) of the high pressure vessel. Figure 16 presents the comparison of the pressure on the nozzle wall. We see that the pressures maximum was underpredicted by IVA3 and a second peak, not observed in the experiment, was predicted on both top positions (near the center line and in the middle). The time when the pressure maxima occur in Figures 13, 14 and 15 is very well predicted by IVA3. As already discussed in [45, 46] (1987,1988) and confirmed by this analysis, the second peaks that are marked by A on Figures 13 and 14 are results of the radial reflection of the two–phase mixture from the side walls to the axis by continuing energy supply in axial direction from the pressure source. They occur in the simulation exactly in that moment at which the radial reflection wave reaches the corresponding location. The time when these peaks occur is overestimated by IVA3, which is a clear consequence of the reflection velocity being predicted smaller than the measured one. The smaller reflection velocity is probably caused by smaller disintegration of the mixture predicted by IVA3 constitutive models. The maxima of the first pressure peaks are underestimated for the internal regions, see Figure 13 and 14. In order to show the influence of the integration accuracy on the magnitude of the peaks we performed two calculations: one with time step 0.000025 s and one with 0.0000125 s. As shown on Figures 13 through 15 the increased accuracy of integration increases the magnitude of the predicted pressure peaks. Obviously the region of occurrence of the first peak should be integrated with an order of magnitude higher resolution (accuracy). The small differences between predicted and measured pressures in the high pressure vessel are explained by the different locations of the compared pressures. The measured oscillations on the nozzle are induced by the opening mechanism of the sliding doors (hydrogen–oxygen explosion) as reported in [40–42] and are not simulated by IVA3. The phase displacement of ≈1s of the average curve in the region after 10 s is a consequence of the accumulative error of all code elements during the integration. In Fig. 17 a,b,c we compare the observed gas distribution in the nozzle entrance region with the predicted one for three different times: 0.0029, 0.0039, and 0.0049. The dashed regions are predicted to be occupied by water. The line represents the experimentally observed form of the visible two phase bubble. Note that the graphical presentation in Figs. 17, 18 is confined to the nozzle entrance region and up to z = 0.53 m only so that the deformation of the moving upper water–gas interface is not presented. For comparison, in Figures 18 a,b,c we present the results for the same times but for a source of pressure 1.1 MPa. The higher the source pressure the faster the two–phase bubble growth. This behavior was correctly predicted by IVA3. In general we

find good agreement between prediction and experiment.

Much stronger water acceleration was achieved experimentally by Mayer and Kirstahler if the diameter of the internal structure was reduced to the diameter of the nozzle – see Figure 19. The results of a simulation of this experiment with IVA3 are compared in Figure 20 with the measurements. Compared to the previous presentations we present in addition the computed boundaries (1) between the dispersed droplet flow and the churn turbulent flow and (2) between the two–phase region and the water region including the speeded numerical diffusion. The experimentally measured visible "bubble" boundary is entered too and lies between these two curves which shows the correctness of the prediction.

Comparing these results with the results obtained by simulating the same experiment with the previous computer code IVA2 (see [45,46]) we found a significant improvement of the predictive capability of the technique used in IVA3.

### 5.2.4 GAS JET EXPANSION IN LIQUID WITHOUT INTERNALS

Next we compare the prediction of IVA3 with the results from an experiment with the same pressure source (6 bar), with the same liquid level, but without Plexiglass internals. The geometry was presented in Fig. 7c.

The results of the reference calculation are presented in Figs. 21 through 24 b. In order to reveal the uncertainties we vary the initial volumetric content of the dissolved gases from 0.001 to 0.004. The result for the pressure near the top centerline is depicted in Fig. 25. We see that the more dissolved gases, the smaller the pressure peaks. Another calculation was performed with, and without taking into the account the opening time of the sliding doors varying it from 0 s to 0.0004 s. The results are shown in Fig. 26.

The measured pressures at the nozzle differ from each other (compare Figs. 24 a and 24 b) which is an evidence of the three–dimensional nature of the flow not taken into account in IVA3 in this particular comparison. The oscillations in the initial times are induced by the explosion mechanism during opening of sliding doors and cannot be predicted by the code.

Having in mind the above discussed uncertainties we see a very good agreement between IVA3 predictions and measurements. From this agreement we conclude that the new IVA3 solution method is capable to simulate fast running processes in two–phase two component flows in a complex geometry. Furthermore, this comparison proves that the models describing the momentum interactions between the gas and liquid velocity fields adequately describe the physics.

## 5.3 DAM BREAK RELEASE OF LIQUID

Next we simulate one of the interesting experiments performed by Maschek et al. [43] (1990) at ambient pressure and temperature. Water was initially held in a cylinder with 11 cm diameter and 20 cm height coaxially within an outer transparent cylinder of 44.4 cm diameter and 55 cm height. The experiments start with the abrupt vertical removal of the cylinder holding the water. The water flowing down under gravitation deforms its initial vertical cross section from rectangular to bell/shaped. After reaching the bottom the significant radial inertia moves the water to the outer boundary increasing the level there to a certain maximum. Again gravitation moves the water down and the potential energy transformed into mechanical energy accelerates the water from the corner towards the center, building a turbulent water peak in the center. Thereafterthe water forms a pool due to friction with the bottom and due to viscous dissipation. This behavior was recorded by means of a high speed film camera. The predicted water volume fraction as a function of radius and height for different times is presented in figure 27. The dashed regions are predicted to be occupied by water. The line entered on the picture is the experimentally observed surface of the water. For the part of the experiment from the beginning to the moment in which the water reaches the external boundary we find very good agreement between IVA3 prediction and experiments – see Figs. 27 a,b,c,d. The next part of the experiment is associated with growth of the surface instabilities and strong turbulization of the mixture. Note that the form of the observed structure in Fig. 27 g resembles 16 to 18 eruptions with peaks being placed about equidistantly in one circle. Obviously they cannot be predicted properly by IVA3 without including appropriate turbulence models in the code. Instead of that, the code predicts relatively compact movement of the water with less strong turbulization and fragmentation of the surface than experimentally observed. In the computation, instead of loosing energy for turbulization,

and fragmentation, the flow transfers potential energy directly into kinetic energy and the reflection from the wall to the center line happens faster than actually observed – see Figs. 27 e,f,g. From this comparison we conclude that the hydraulic model of IVA3 works properly for cases in which the acceleration is the governing effect and taht it needs improvement for cases in which strong surface turbulence and fragmentation occur. It is interesting to note that the turbulent pulsation of the liquid volumetric fraction associated with velocity pulsations causes significant differences to the one–phase flow turbulence.

## 5.4 FALSE DIFFUSION

In fact the mutual macroscopic diffusion of the gas and water across the "bubble surface" as described in section 5.2 is caused by the considerable spatial pressure difference across the two continua. The same pressure difference causes different accelerations of liquid and gas due to the different densities. At this moment all other effects are secondary. Surface tension starts to be important after water droplets are surrounded by gas. Surface tension balances the hydrodynamic destruction forces and governs the drop size. The higher the pressure gradient the less important are surface tension effects on the fictitious "bubble surface". The smaller the pressure gradient (as in case of section 5.3) the stronger the surface tension effects. Even for relatively small spatial pressure gradient the so–called nonphysical discontinuity smearing should be addressed more carefully in the future models than done in IVA3.

The false diffusion of IVA3 – method for such cases, consists of three components (a) pure numerical diffusion, (b) nonphysical discontinuity smearing due to absence of models for flow patterns like free surface flow within a computational cell with six possible predominant orientations of the continuum–continuum interface (anisotropy of the volume fraction distribution) and (c) the smearing effect of the staggered grid formulation. The pure numerical diffusion due to neglected of high order derivatives in the numerical representation of the convective terms has a negligible contribution to the particular case considered in sections 5.2 and 5.3 in contrast with the latter two effects. Therefore "simply" increasing the order of the discretization does not solve the problem. This statement is strongly supported by the comparison of the IVA3 prediction given in Figs. 27 with the prediction of the experiment discussed in Ch.5.3 reported by Maschek, Munz and Mayer in [43] (1990) and performed with the 2D–AFDM computer code. AFDM uses namely second order finite difference approximation of the convective terms. Consequently future model improvement should:

(a) Include free surface flow pattern models within the cell. The best way to do so seems to be the extension of the volume–of–fluid method as introduced by Hirt and Nichols [44] (1981) for 2D liquid gas incompressible flow to multiphase 3D flows;

(b) Avoid the smearing effect of the staggered grid introducing new modeling techniques.

## 5.5 ABOLFADL AND THEOFANOUS BENCHMARK – THREE FLUIDS IN 2D GEOMETRY WITHOUT INTERNALS

In the next step of the verification of IVA3 we use a benchmark problem first introduced by Abolfadl and Theofanous in [62] (1987). The purpose of this simulation is to demonstrate the capability of IVA3 to model three–velocity–fields three–phase flows of solid particles, water, and steam in 2D geometry with strong thermal and mechanical interaction between the velocity fields.

The geometry, initial, and boundary conditions are defined as follows: A cylindrical interaction volume of 1.7 m height and 2.2 m radius is initially filled with a saturated water–steam mixture at ambient pressure of 0.1 MPa. The steam volume fraction is 0.05. The computational space communicates with the environment by a free cylindrical surface 0.19 m wide placed at the upper part of the volume. Velocity boundary conditions are imposed at a circle of 1.76 m diameter placed at the top where solid particles of corium with a prefragmented size of 2 cm and a temperature of 2500 K enter the integration region with a vertical downward velocity of 1 m/s and volume fraction 0.5.

We simulate 1.5 s physical time in a $\pi/4$ segment with 11x10 computational cells in cylindrical geometry.

In what follows we discuss the results: Figure 28 presents the particle, water, and steam volume fractions as functions of the radius, r, and of the distance from the bottom, z, for times 0, 0.5, 1. and 1.5 s, respectively. We present the volumetric concentrations in each computational cell in the following manner: The volumetric fraction of each cell occupied by particles is presented by black regions, the volumetric fraction occupied by water is represented by a dashed region, and the residual volume fraction, occupied by steam, remains blank. This kind of presentation is quantitative. After entering the computational region, the solid particles are transported downwards mainly by inertia and gravity and they produce steam by film boiling and radiation. The increased specific volume of the mixture is easily compensated by the volumetric flow leaving the computational region. Note that for this example the water–steam mixture will flow out from the computational region due to gravity without any perturbation until reaching the lower edge of the opening cross section. Approximately at 0.4 s the first solid particles reach the bottom. Thereafter the particles form a cone at the bottom and start to spread to the both sides. This process is associated with steam production. Approximately at 1.1 s the first solid particles reach the lower right corner. After this moment the particle level at the bottom starts to increase. After 0.8 s the downwards falling hot particles are completely surrounded by steam. The voided region expands its volume with time. The rest of the water not yet evaporated predominantly occupies regions in which no hot particles are present.

Figure 29 presents the predictions of the volume fractions at 0.5 and 1 s of IVA3 and PM–ALPHA. The latter are reported by Amarasooria and Theofanous [63] (1988). In order to facilitate exact data comparison also for future analysis of this benchmark we give the tables with the numerical results in Appendix 1. Some integral results as a function of time are presented in Figure 30. We see that the theoretical solid particle mass compares perfectly with the predicted total solid particle mass in the computational region. This is an evidence for the good accuracy of the integration of the conservation equations. Abolfadl and Theofanous [62] (1987) investigated the question how large is the amount of hot particles premixed with continuous water was. The situation of hot particles being in film boiling and surrounded completely by water is considered as a starting point for violent mechanical energy release during steam explosion in the literature. As a criterion of

premixing the authors introduced the limit $\alpha_1/(\alpha_1+\alpha_2) < 0.5$, which means that particles in cells having volume fractions satisfying the above criterion are available for possible steam explosion. This criterion in fact approximately coincidences with the criterion used in IVA3 for predicting that a three phase mixture involves continuous water, namely $\alpha_1/(\alpha_1+\alpha_2) < 0.52$. The sum of the particle masses being in this flow regime is presented in Figure 30 as a function of time and compared with the predicted sum by PM–ALPHA. Obviously, IVA3 predicts considerably less particle mass to be in three–phase bubble flow than the PM–ALPHA code. If one examined carefully the models used for heat and mass transfer due to film boiling and the approximations of the drag coefficients in both codes one should find many differences which explain the difference between both results. For comparison we present in Figure 30 an additional curve obtained as follows: Isolate a control volume from all surrounding cells as shown in Figure 31 and measure the amount of particles surrounded by water after complete mechanical separation. This "stagnant" particle volume fraction is considered as the absolute theoretical maximum amount of particle mass which can be surrounded by liquid. Sum the so obtained mass over the integration region. As expected this amount is larger than the amount being in three–phase bubble flow.

Figure 32 presents the pressure in four cells at the bottom. After initial increase up to about 0.17 MPa and some oscillations, the pressure reaches the ambient level. Three small pressure spikes are observed in the central cells after entrapment of water. Because the surrounding cells are predominantly occupied by steam and the flow patterns are disperse, the energy of the pressure spikes is not sufficient to cause global pressure increase of the computational region. On the same figure we enter the results by Amarasooria et al. Not knowing exactly from [63] (1978) the location of this pressure we compare it with pressures recorded at the vertical wall, Figure 33, and at the top wall, Figure 34, respectively. In general we do not observe a comparable pressure increase in these positions. The differences are explained less by the differences in the locations of the compared values than by the differences in the constitutive models for mechanical and thermal interaction used in IVA3 and PM–ALPHA. It is not the purpose of this comparison to claim which of the two simulations is closer to reality. The answer of this question needs experiments. We only state at this place that IVA3 is capable of three–fluid modeling in 2D geometry and that it provides meaningful results. In Chapter 8 we will continue the IVA3 verification by comparison with real melt–water interaction processes in 3D geometry and make more conclusions about the three–fluid modeling capability of the code.

## 5.6 THREE–FLUID TEST IN 2D GEOMETRY WITH COMPLEX INTERNALS

The purpose of the next test is to check the functional capability of IVA3 to handle three fluids in complicated 2D geometry. This example has the same features as the previous one but is somewhat more nuclear safety oriented in the sense that a real 1300 MWe PWR reactor geometry is used and the particles are interacting with the water region being driven initially only by gravity and later by all arising hydrodynamic forces between particles, water, and steam even in regions outsides of the lower plenum. Modeling obstacles in reactor safety applications for melt water interaction analysis is very important because obstacles resists the escaping water and facilitate melt water intermixing which considerably influences the pressure history.

Next we describe briefly the geometry, initial, and boundary conditions. Consider a

cylindrical pool of solid, pre fragmented particles of corium having diameters of 2 cm and initial temperatures of 2500 K. The dimensions of the pool are assumed to be 3 m diameter and 1.4 m height. The cylindrical walls are not permeable nor is the bottom of the pool except for a circle of 1.611 m diameter which has 50 % axial permeability. Only 67% of the pool are occupied by solid particles ($\approx$ 52 tones). This pool is located symmetrically in a typical 1300 MWe PWR reactor vessel at the bottom of a degraded core (2 m level in the computational geometry). Outsides the pool the core and all other structures presented in fig 35 are intact. We assume saturated water in the lower plenum with 1.7 m depth and 0.1 % volumetric fraction of dissolved gases. The system pressure in the voided regions is assumed to be 0.1 MPa. The radial flow at radius 1.5 m between 0.7 and 1.5 m height is restricted by perforated sieve barrel. The downcomer and the upper plenum are assumed to communicate with the environment being at 0.1 MPa pressure.

We make use of the symmetry and simulate only a $\pi/4$ 2D sector with 11 x 28 computational cells.

The initial state at time zero is presented in figure 35 together with the cell noding diagram including 22 of the 28 horizontal cell rows. Figure 36 presents the volumetric concentrations of the three components particles, water, and steam at different times. Thess pictures reveal the following physical process. After about 0.2 s the particles reach the water surface and cause intensive evaporation. Both, the impulse introduced by the falling particles into the water pool and the intensive steam production cause the first pressure peak in the middle at about 0.26 s – see Figure 37. The intensive evaporation increases the local pressure insides the region that is rich on hot particles and tries to push the water out from the lower plenum. The resistance forces caused by the water inertia (approximately 16 t), flow direction change, sieve barrel, flow distribution plate etc. cause an global pressure increase in the lower plenum. Thus the first pressure peak of about 0.7 MPa is reached. This pressure increase affects significantly the further process development. Particles, water, and steam are accelerated from the origin of the explosion to the peripheral regions. Consequently steam is blown into the core region and the particles are accelerated upwards into the cavity – see figure 36 for times between 0.52 through 0.74 s. The counter current flow into the core region increases the upwards drag on the particles and changes the rate at which the particle mass penetrates into the lower plenum as it can be seen from Figure 38. Simultaneously the velocities of the particles already surrounded by water increase after the first small explosion which causes increase of the convective evaporation. This and the increased particle concentration in regions with particle–water bubble flow causes further 5 pressure peaks to be observed at the bottom. Figure 36 contains the occurrence times and the magnitude of the peaks. All these successive pressure peaks accelerate water from the lower plenum into the downcomer. The evidence is given in Figure 38 where the total water mass in the computational volume and the water mass being below the core bottom level are plotted versus time. The evaporated water mass is much lower than the water mass leaving the lower plenum.

After the first explosion the core is partially disintegrated and accelerated upwards mainly in the central region. Thereafter the particles fall down, predominantly occupying the right corner, and leave the core region.

The fuel mass in the lower plenum reaching the bottom starts to form a pool. As long as water is available in this region, further explosions are possible – see Figure 37, the last three peaks. But they *did not propagate into the lower plenum because that is predominantly occupied by gas.*

Figure 38 presents the particle mass being in bubble–liquid three phase flow. This mass is reaching a maximum. Thereafter it starts to decrease due to the absence of water

around the hot particle regions. In the same picture the theoretical maximum of stagnant particle mass which can be surrounded by water is entered for comparison. In figures 39, 40 and 42 similar information is entered for the cases B, C, and D as described in Table 8.1 and some comparisons between different cases are given in Figure 41 and 43. Table 8.1 also contains information about the obtained maxima and the times when these maxima occur.

Table 5.6.1 Different 2D hot particle – water interaction cases in reactor geometry computed with IVA3.

| Case | A | B | C | D |
|---|---|---|---|---|
| Water mass, t: | 16. | 16. | 16. | 16. |
| Water temperature, C: | 100. | 100. | 100. | 100. |
| Sieve barrel | Yes | Yes | Yes | Yes |
| Sieve barrel axial permeability, –: | 0.5 | 0.5 | 0.5 | 0.5 |
| Flow distribution plate | Yes | No | No | No |
| Particles mass, t: | 52. | 80. | 80. | 80. |
| Particle temperature, K: | 2500. | 3000. | 3000. | 3000. |
| Particle material | Corium | $UO_2$ | $UO_2$ | $UO_2$ |
| Prefragmented particles | Yes | Yes | Yes | Yes |
| Particle diameter, m: | 0.02 | 0.01 | 0.02 | 0.02 |
| Circle diameter of the particle release cross section, m: | 1.6 | 1.8 | 1.8 | 1.2 |
| Axial permeability of discharge circle, –: | 0.5 | 0.5 | 0.5 | 0.5 |
| Results | | | | |
| Maximum particle mass being in water–bubble environment, t ± 0.25 t: | 1. | 4.44 | 8.7 | 1.6 |
| Time, s: | 0.55 | 0.73 | 0.84 | 0.68 |
| Theoretical maximum stagnant particle mass which may be wetted by the surrounding water, t, ± 0.25 t: | 4.9 | 9.8 | 10.2 | 3.47 |
| Time, s: | 0.7 | 0.85 | 0.84 | 0.85 |

The accuracy of the presented computations is characterized by 0.22 % of fuel mass lost in the entire computational region due to numerical and nonphysical diffusion inherent to the IVA3 computer code at the end of the considered processes.

What we learn from this analysis is:

(a) The processes caused by hot particle–water interaction in the lower plenum of a PWR

reactor strongly influence the overall particle transport of the reactor;

(b) Even considering the particles as prefragmented and not allowing for further fragmentation during the particle–water interaction we observe local pressure excursions of small magnitude which in fact prevent larger particle–water intermixing;

(c) The geometrical structures like flow distribution plate, sieve barrel, and downcomer significantly prevent the water from escaping from the lower plenum and enable buildup of pressure peaks at an early stage of the premixing. The pressure peaks facilitate the removal of water from regions rich in hot particles and in fact additionally limit the contact between hot particles and water;

(d) For the considered variation of the geometry and initial conditions, the maximum of the hot particle mass being in three–phase bubble flow was between 1. and 8.7 t ± 250 kg. The theoretical maximum of stagnant mass of particles which can be surrounded by liquid was between 3.47 and 10.2 t.

Finally this computation is an evidence for the capability of IVA3 to model three–phase flow in complicated 2D geometry with strong thermal and mechanical interaction between the fields. In the next Chapter we will continue the verification with a much more complicated case, in which molten metal isto a injected in water pool with three dimensional geometry.

## 5.7 MODELING OF MOLTEN CORIUM–WATER INTERACTION IN A DEEP POOL

Recently physical phenomena affecting the consequences of postulated severe accidents in light water reactors (LWR's) are investigated. Included among these investigations is the analysis of corium–water thermal interaction (CWTI). During CWTI molten core material, denoted as corium, comes into contact with water under a variety of mixing conditions. Experiments performed in this field are reported in [57–64] (1983–1985) among others. Parallel to the experimental investigation mathematical models for the description of the phenomena are developed. The final purpose of such models is to adequately describe the release of molten corium into water, fragmentation, interfacial heat, mass, and momentum transfer, transport of the participating materials, the resulting pressure history and consequently the loads acting on the construction – all phenomena directly or indirectly observed in the experiments, and to use the resulting computer code for the design of measures mitigating the consequences of such accidents in real systems. On this way frequently problems are revealed concerning missing knowledge in different subfields.

Theoretical 2D analysis of prefragmented CWTI have already been reported by Abolfadl and Theofanous et al. [62] (1987), Amarasooriya and Theofanous [63] (1988) and Thyagaraja and Fletcher et al. [64] (1988). The purpose of this work is to illustrate a 3D analysis of CWTI with not prefragmented corium, which means that the development of the corium structure from a continuum to dispersed particles and vice versa is described by means of mathematical models. We choose for our analysis an excellently documented test performed by Spencer et al. in [57] (1985). What makes this test interesting is that the corium mass flow inserted into the so–called interaction vessel is measured so that it can be used as an outer boundary condition. Furthermore, all details that are necessary for modeling are documented in [57].

We perform the modeling with the computer code IVA3.

In this work we will present the results of the comparison between theory and experiment.

### 5.7.1 EXPERIMENT DESCRIPTION

The results of corium–water thermal interaction (CWTI) tests are reported in [57] (1985). The basic elements of the experimental apparatus, illustrated in Figure 44, include: (a) the corium thermite vessel (TV) in which thermite reaction powders are ignited to generate the corium melt, (b) a corium release assembly which when actuated opens a path for the corium melt to pour into the interaction vessel, (c) the interaction vessel (IV), 0.212 m I.D. x 0.511 m high, which contains the preheated pool of water ( 0.32 m depth), (d) an expansion 0.108 m I.D. pipeway which provides a path for the steam to expand into a large volume, and (e) the expansion vessel (EV), 0.76 m I.D. x 3 m high, which provides the system with a large volume of 1.42 $m^3$ for steam accumulation to avoid pressurization of the system.

A stream of molten corium was poured into a deep pool of water in order to determine the mixing behavior, the corium to water heat transfer, and the characteristic sizes of the quenched debris. The corium composition was 60% $UO_2$, 16% $ZrO_2$, and 24 %

stainless steel by weight; the initial melt temperature was 3080 K, i.e. ≈ 160 K above the oxide phase liquidus temperature. This corium mixture is representative of the meltdown products in the rector core in which the zircaloy cladding has been completely oxidized, plus provision for molten steel from the downward melt progression through the core support structure. Typically there was a distribution of very small argon gas bubbles in the melt, a residual of the initial gas fraction in the packed powders. The corium pour stream was a single–phase 2.2 cm diameter liquid column which entered the water pool in film boiling at 4 m/s. The water subcooling was 6 K. The cover gas temperature in the interaction vessel was 93 C and in the expansion vessel 141 C.

A flush X–ray system was used for visual diagnostics of events in the steel interaction vessel. The measured melt mass flow entering the IV was reported in [57] and used here as a boundary condition. The measured integral melt mass entering the IV was 2.39 kg.

Note that the expansion pipeway cross section was not uniformly distributed around the IV perimeter which made the process threedimensional.

## 5.7.2 GEOMETRY MODELING, INITIAL AND BOUNDARY CONDITIONS

The experimental facility is symmetric with respect to the vertical plane defined by the IV axis and the center of the expansion pipeway cross section. To save computer cost this symmetry is used and only one half of the facility is modeled by means of 7 coaxial segments, 2 angular sectors and 13 axial layers. The first angular sector, 0.534 rad, contains the expansion pipe cross section at the interaction vessel side. The second angular sector, $\pi$–0.534 rad, contains the region of the impermeable vertical IV wall. Thus, this is a fully three–dimensional geometry model. An attempt to model this process simplifying the 3D geometry to 2D geometry by using only one angular sector and a uniformly distributed escape pipeway cross section along the IV – perimeter would replace the real physical intermixing process with a reduced, unphysical intermixing of melt and water. The IV was modelled with 4 x 2 x 13 cells.
The EV is not modeled in detail and in the real geodetical level. Only the outer radius of the computational region was chosen so as to ensure a passive volume of 1.42 $m^3$ for the EV.

The measured fuel mass flow rate as a function of time given in Fig. 6 in [57] and reproduced here in Fig. 45 was used as a boundary condition for the upper central cell having a radius of 0.0127 m – the measured radius of the observed corium jet. The integral of the melt mass flow as a function of time is given in Fig. 46. The final constant value corresponds exactly to the measured 2.39 kg melt that have entered the IV. The density of the model corium corresponds to 60% $UO_2$, 16% $ZrO_2$, and 24% stainless steel (67% Fe, 21% Cr, 12% Ni). The liquidus temperature of the model corium was 2920 K. The initial temperature of the model corium was 3080 K. The water mass in the IV was approximately 11 kg and the water temperature 94 C.

The results presented in this chapter are obtained with the fragmentation and coalescence models presented in Chapter 2.

### 5.7.3 RESULTS OF THE MODELING AND DATA COMPARISON

The simulation of 2.4 s physical time was performed with IVA3 on an IBM 3090 within 3 h CPU time. Some of the results are presented in Figures 47 through 52. The computation was performed tolerating a prescribed mass conservation error in the IVA3 method of 3% locally. The result of this is clearly presented in Fig. 46 in which the total melt mass in the computational region is plotted versus time and compared with the theoretical one. Obviously the tolerated total mass imbalance of 6.5% at maximum cannot influence the results substantially. The high–velocity steam–water mixture caused sweepout of corium from the IV into the EV. The results of the computation containing the sweep out are presented in Fig. 47. The computed final sweepout was 320 ± 20 g and the measured one 318 g. Fig. 48 presents the melt mass being in three–phase bubble flow as a function of time. We see that only between approximately 0.3 and 0.7 s there was three–phase bubble flow in the computational region. Just during this time the pressure peak in the IV occurs. In the same figure the fictitious melt mass which can be theoretically surrounded by water in adiabatic and stagnant case is presented too. Figure 49 presents the water mass in the computational region and in the IV versus time. The difference between the initial water mass and the mass actually observed in the computational region is the evaporated mass. We see that after one second approximately 9 kg water were swept out into the EV.

The physical picture leading to the quantitative results presented up to now is revealed by visualization the volumetric fractions of the three components in the IV as presented in Figure 50 for different times and for the first angular sector containing the escape pipeway. The dicretization net is also clearly seen. The volume of each particular computational cell occupied by corium is presented by black, the volume occupied by steam by blank and the residuals, the volume occupied by water, by dashed regions. In this way we present in each cell the quantitative information. The expected complex physical phenomena are obviously appropriately modelled by IVA3. We clearly see the core jet formation, the jet–water thermo–mechanical interaction leading to jet fragmentation, the intensive evaporation accelerating gas, droplets, and small fuel particles upwards, the gravitational melt separation at the bottom, the sloshing movement of the disintegrated fuel at the bottom etc. The pressure increase in the lower half of the liquid pool and the resulting upward acceleration of the liquid lead to an important 3D effect modelled here. While the water being in the immediate neighborhood of the expansion pipeway is swept out of the IV region without further interaction with the jet, the water being behind the jet and swept out into the expansion pipe is forced to interact with the jet.

Two important results of the ANL experiment analyzed here are the pressure–time histories in the IV and in the EV as presented in Figs. 51 and 52. Both figures also present the computational results. Since it is not known from [57] where exactly the pressure transducer was mounted in the IV we give in Figure 51 three different pressures as computed in the outer cells of the IV corresponding to bottom, middle and top positions. These two figures clearly illustrate

(a) that the processes controlling separate phenomena are appropriately modelled in IVA3;

(b) that IVA3 is able to reproduce a very complicated interaction between different thermal and mechanical flow phenomena in a 3D geometry.

The quantitative differences in the pressures depend essentially on the models used

(a) for drag forces in the three phase mixture responsible for the adjustment of the relative

velocities during the process,

(b) for flow regime identification depending on the relative velocities and on the volumetric fractions, and

(c) of fragmentation and coalescence.

There are complicated interactions among the above mentioned constitutive models themselves and between the constitutive models and the overall flow model. Further improvement of the particular models should improve the modeling feature. A more accurate geometrical representation of the expansion vessel geometry should improve the modeled asymptotic pressure behavior.

### 5.7.4 CONCLUSIONS

The results of the ANL corium–water thermal interaction test called CWTI–9 and reported by Spencer et al. in [57] (1985) are compared with the results of a 3D simulation performed with the IVA3 code. We draw the following conclusions from this comparison:

(1) The separate phenomena controlling the process like

– core jet formation,
– jet–water thermo–mechanical interaction leading to jet fragmentation,
– droplet and bubble fragmentation and coalescence,
– mechanical interaction within the three–phase mixture,
– thermal interaction within the three–phase mixture,
– gravitational melt separation at the bottom,
– sloshing of the disintegrated fuel at the bottom etc.,

are appropriately modelled in IVA3;

(2) IVA3 is able to reproduce very complicated interactions between different separate thermal and mechanical flow phenomena in a complex 3D geometry.

The quantitative differences in the pressures observed during this comparison depend on the models of fragmentation and coalescence used. Further separate model improvment is expected to improve the overall modeling capability of IVA3.

## 5.8 MODELING OF MOLTEN CORIUM – WATER INTERACTION IN PWR GEOMETRY

Let us summarize the successful tests performed so far with IVA3 for checking the three–fluid modeling capability:

1) Steady state forces in real three–fluid systems performed by Kolev, Tomiyama and Sakaguchi in [32] (1990);

2) Abolfadl and Theofanous benchmark – three fluids in 2D geometry without

internals performed in Chapter 7;

3) Four three–fluid tests in 2D geometry with complex internals with dynamic fragmentation and coalescence of water and steam performed in Chapter 8;

4) Three–fluid test in 3D geometry with dynamic fragmentation and coalescence of water, steam, and molten metal including successive freezing of the metal fragments.

This series of three–fluid test shows definitely the capabilities of the IVA3 architecture, numerics, and models to describe successfully transient three–fluid flows in simple and complex geometries with weak to very strong interfacial interactions.

Relying on this experience we perform an analysis relevant to the safety of PWR nuclear reactors, namely release of a molten pool of corium into the lower plenum filled with water in a real 1300 MWe PWR geometry as described in Chapter 5.6. The initial conditions and some important geometrical characteristics are given below:

Table 5.8.1 Molten corium–water interaction in 1300 MWe PWR reactor geometry

| Case | E |
|---|---|
| Water mass, t: | 15.6 |
| Water temperature, C: | 100. |
| Sieve barrel | Yes |
| Sieve barrel axial permeability, –: | 0.5 |
| Flow distribution plate | No |
| Melt mass, t: | |
| Melt temperature, K: | 3080. |
| Melt material | Corium: 60% $UO_2$, 16% $ZrO_2$, and 24% stainless steel (67% Fe, 21% Cr, 12% Ni) |
| Prefragmented particles | No |
| Circle diameter of the particle release cross section, m: | 1.61 |
| Axial permeability of discharge circle, –: | 0.5 |
| Results | |
| Maximum particle mass being in water–bubble environment, t ± 3%: | 0.547 |
| Time, s: | 1.34 |
| Theoretical maximum stagnant particle mass which may be wetted | |

| | |
|---|---|
| by the surrounded water, t, ± 3%: | 1.96 |
| Time, s: | 1.11 |

As far as the author knows, this is the first numerical simulation of this kind for complex PWR reactor geometry with complicated internal structures. Note that the particle sizes of melt, water and bubbles is described by dynamical models of fragmentation and coalescence.

We use the symmetry and simulate only $\pi/4$ 2D sector with 11 x 28 computational cells.

Figure 53 shows the geometry, the cell noding diagram used in IVA3 for this simulation, and the initial conditions.

In what follows we discuss the results of the simulation.

Figure 54 shows the volumetric concentrations of the participating flow components, namely corium, water, and steam at different times. The accuracy of the mass conservation is presented in figure 56. The maximum melt mass conservation error is less than about 3%. Figure 55 presents pressures as functions of time at different positions at the inner vessel wall. Figure 56 presents the integral distribution of melt and water as functions of time. The above mentioned figures reveal the following physical phenomena taking place in this theoretical simulation.

Melt reaches the water surface after exerting already some fragmentation. The melt mass being in bubbly three–phase flow with film boiling increases and reaches a first local maximum of about 300 kg at 0.38 s. Before this maximum is reached the first explosion event occurs. Obviously the origin of the pressure wave is immediately below the core at half water depth. The pressure wave propagates through the lower plenum, see figures 55 a through d, through the downcomer, see fig. 55 e, and partially through the core region. The expanding pressure wave accelerates material in all directions available for the flow. Water is pushed into the downcomer and into the free reactor regions. It is clearly seen from fig. 56 that the water mass below the core bottom level dramatically decreases. In that time the melt mass being below the core bottom level decreases too due to the upward acceleration of the melt carried by gas mainly. During the period between about 0.4 and 0.9 s the molten core is partially disintegrated and melt is projected into the upper part of the reactor vessel. After that time the melt in the upper part settles down and continues to flood the lower plenum as it can be see from the curve presenting the melt mass below the reactor bottom level in fig. 56. The melt mass being in bubble three phase flow reaches a maximum of 547 kg at about 1.34 s. The pessimistically estimated maximum of the stagnant melt mass which can be surrounded by water is about 1960 kg and is reached at 1.11 s.

Obviously the intact structure of the upper part of the core dissipates mechanical energy transported by the upwards accelerated material and hinders the attack of the top of the reactor by this material. As a result only a monotonic and slow increase of the pressure is predicted at the top wall inside the vessel, see fig. 55 f through h. The very short lasting pressure peak in fig. 55 a is due to a sloshing acceleration from the periphery to the center of the heavy melt mass (focussing of the slushing mechanical energy). It does not influence the surroundings.

Note that in this case the computation was performed with the assumption that the core distribution plate is intact and has an axial permeability of 0.5. In this case the feared steam explosion has no serious consequences because it happens too early and in fact hinders further melt–water intermixing by pushing the water out of the lower plenum. Further violent explosions are hardly to be expected under these conditions. The predicted melt–water intermixing is much smaller than in the case with solid prefragmented particles.

Next we perform a similar analysis assuming that the lower ends of the fuel elements and the flow distribution plate are molten and give free the same cross section of 1.61 m diameter as before without any additional resistance and the possibility of multiple jetting of the molten fuel. The results are presented in the same manner as before in FIGURES 57 through 60. We observe later but much more violent pressure increase in the lower plenum disintegrating in fact the melt pool totally and accelerating all flow components in all directions available to the flow. The maximum of the pressure in the lower plenum is of the order of 4.2 MPa. We see again that as long as some upper core structures are intact, the impact on the top of the reactor vessel is avoided by considerable dissipation of the mechanical energy of the flow by these upper structures. FIGURE 61 presents a comparison between the maximum pressures obtained with different assumptions about the initial state (1.61 diam of the release cross section): prefragmented fuel and intact structures below the core, non prefragmented fuel with and without intact structures below the core. From this figure we draw the following conclusion: None of the considered events is dangerous for the integrity of the reactor vessel under such initial and boundary conditions. This does not mean that other initial conditions and kinds of pouring of melt into the lower plenum will not cause violent steam explosions. Such cases remain to be investigated in the future use of the IVA3 code in addition to experiments.

What we demonstrated with this IVA3 application is that the code is able to describe three–field flows with strong thermo–mechanical interactions including fragmentation and coalescence in complicated reactor geometries. At different stages of this computation all code elements except for the nuclear reactor core heat conduction model and the fuel rod–flow heat transfer models were addressed and reasonable interactions were found.

## 6. FINAL REMARKS

The further application of the code in different fields in science and technology will certainly need improvement of some constitutive models or replacement of some of the existing models with new ones. Nevertheless the results obtained with IVA3 are very encouraging and show that the code possesses a versatile code architecture and organization and allows for solution of very complicated tasks of practical interest with reasonable computation cost and stability not only in nuclear safety analysis.

## ACKNOWLEDGMENTS

The author is greatly indebted to Prof. K.Rehme for the valuable discussions during the development of IVA3, and to Prof. Kessler for the motivation to perform this study.

Appendix 1.

Table 1 Flow regime map for $\tau = 0.5$

| K | Read the following Table using Table 1 in Ch.1 |
|---|---|
| 11 | 14 14 14 14 16 16 16 16 15 15 07 |
| 10 | 14 14 14 14 16 16 16 16 16 15 16 |
| 9 | 16 16 16 16 16 16 16 16 15 15 05 |
| 8 | 16 16 16 16 16 16 16 16 15 15 05 |
| 7 | 16 16 16 16 16 16 16 15 15 15 15 |
| 6 | 16 16 16 16 16 16 16 15 15 15 15 |
| 5 | 16 16 16 16 16 16 15 15 15 15 15 |
| 4 | 16 16 16 16 16 16 15 15 15 15 15 |
| 3 | 16 16 15 15 15 15 15 15 15 15 15 |
| 2 | 16 16 16 16 15 15 15 15 15 15 15 |

Table 2. Particle temperature at $\tau = 0.5$ s

| K | |
|---|---|
| 11 | 2489. 2489. 2489. 2489. 2485. 2483. 2479. 2473. 2469. 2467. 2500. |
| 10 | 2489. 2489. 2489. 2489. 2485. 2480. 2477. 2472. 2464. 2445. 2500. |
| 9 | 2488. 2487. 2487. 2487. 2484. 2478. 2474. 2465. 2455. 2440. 2431. |
| 8 | 2483. 2482. 2481. 2481. 2475. 2471. 2462. 2450. 2441. 2434. 2429. |
| 7 | 2477. 2474. 2473. 2473. 2468. 2465. 2454. 2441. 2434. 2430. 2428. |
| 6 | 2469. 2466. 2465. 2464. 2459. 2455. 2445. 2434. 2430. 2427. 2429. |
| 5 | 2460. 2457. 2457. 2454. 2451. 2447. 2438. 2431. 2428. 2425. 2434. |
| 4 | 2451. 2447. 2446. 2445. 2445. 2441. 2433. 2429. 2427. 2427. 2450. |
| 3 | 2444. 2442. 2441. 2441. 2441. 2435. 2429. 2428. 2426. 2437. 2484. |
| 2 | 2440. 2438. 2438. 2437. 2435. 2430. 2427. 2429. 2432. 2453. 2488. |

Table 3 Volumetric fraction of steam at $\tau = 0.5$ s

| K | |
|---|---|
| 11 | 0.694 0.695 0.696 0.697 0.991 0.969 0.855 0.576 0.344 0.139 0.904 |
| 10 | 0.765 0.767 0.769 0.771 0.985 0.978 0.918 0.812 0.535 0.230 0.786 |
| 9 | 0.788 0.797 0.804 0.813 0.975 0.955 0.883 0.743 0.448 0.303 0.200 |
| 8 | 0.761 0.764 0.770 0.773 0.911 0.880 0.809 0.675 0.394 0.257 0.158 |
| 7 | 0.685 0.689 0.703 0.702 0.784 0.766 0.672 0.403 0.288 0.185 0.119 |
| 6 | 0.683 0.690 0.702 0.691 0.748 0.726 0.520 0.365 0.230 0.138 0.098 |
| 5 | 0.716 0.717 0.733 0.718 0.757 0.680 0.512 0.297 0.172 0.108 0.086 |
| 4 | 0.629 0.640 0.647 0.627 0.652 0.563 0.409 0.230 0.128 0.090 0.077 |
| 3 | 0.556 0.519 0.482 0.434 0.376 0.378 0.247 0.143 0.093 0.074 0.067 |
| 2 | 0.637 0.618 0.591 0.535 0.480 0.311 0.172 0.097 0.067 0.054 0.047 |

Table 4 Volumetric fraction of water at $\tau = 0.5$ s

| K | | | | | | | | | | | |
|---|---|---|---|---|---|---|---|---|---|---|---|
| 11 | 0.000 | 0.000 | 0.000 | 0.000 | 0.000 | 0.029 | 0.145 | 0.424 | 0.656 | 0.861 | 0.096 |
| 10 | 0.000 | 0.000 | 0.000 | 0.000 | 0.000 | 0.019 | 0.081 | 0.188 | 0.465 | 0.769 | 0.214 |
| 9 | 0.018 | 0.012 | 0.007 | 0.002 | 0.002 | 0.040 | 0.115 | 0.256 | 0.551 | 0.697 | 0.799 |
| 8 | 0.052 | 0.055 | 0.055 | 0.057 | 0.044 | 0.108 | 0.186 | 0.322 | 0.605 | 0.742 | 0.841 |
| 7 | 0.141 | 0.149 | 0.145 | 0.152 | 0.155 | 0.214 | 0.321 | 0.593 | 0.710 | 0.814 | 0.880 |
| 6 | 0.175 | 0.182 | 0.179 | 0.197 | 0.192 | 0.253 | 0.470 | 0.631 | 0.768 | 0.861 | 0.901 |
| 5 | 0.177 | 0.188 | 0.181 | 0.204 | 0.196 | 0.301 | 0.479 | 0.699 | 0.826 | 0.891 | 0.913 |
| 4 | 0.293 | 0.291 | 0.292 | 0.319 | 0.313 | 0.421 | 0.584 | 0.767 | 0.871 | 0.910 | 0.922 |
| 3 | 0.388 | 0.433 | 0.475 | 0.531 | 0.601 | 0.612 | 0.749 | 0.856 | 0.906 | 0.926 | 0.933 |
| 2 | 0.308 | 0.336 | 0.369 | 0.435 | 0.499 | 0.679 | 0.824 | 0.901 | 0.933 | 0.946 | 0.953 |

Table 5 Volumetric fraction of solid particles at $\tau = 0.5$ s

| K | | | | | | | | | | | |
|---|---|---|---|---|---|---|---|---|---|---|---|
| 11 | 0.306 | 0.305 | 0.304 | 0.303 | 0.009 | 0.002 | 0.001 | 0.000 | 0.000 | 0.000 | 0.000 |
| 10 | 0.235 | 0.233 | 0.231 | 0.229 | 0.015 | 0.003 | 0.001 | 0.001 | 0.000 | 0.000 | 0.000 |
| 9 | 0.193 | 0.192 | 0.189 | 0.186 | 0.023 | 0.005 | 0.002 | 0.001 | 0.001 | 0.001 | 0.001 |
| 8 | 0.187 | 0.182 | 0.175 | 0.170 | 0.045 | 0.013 | 0.005 | 0.002 | 0.002 | 0.001 | 0.001 |
| 7 | 0.174 | 0.162 | 0.152 | 0.146 | 0.061 | 0.019 | 0.007 | 0.004 | 0.002 | 0.001 | 0.001 |
| 6 | 0.142 | 0.129 | 0.119 | 0.112 | 0.060 | 0.022 | 0.010 | 0.004 | 0.002 | 0.001 | 0.001 |
| 5 | 0.107 | 0.095 | 0.086 | 0.078 | 0.048 | 0.020 | 0.009 | 0.004 | 0.001 | 0.001 | 0.000 |
| 4 | 0.079 | 0.069 | 0.062 | 0.054 | 0.035 | 0.016 | 0.006 | 0.002 | 0.001 | 0.000 | 0.000 |
| 3 | 0.056 | 0.049 | 0.043 | 0.035 | 0.024 | 0.010 | 0.004 | 0.001 | 0.001 | 0.000 | 0.000 |
| 2 | 0.055 | 0.046 | 0.040 | 0.029 | 0.021 | 0.010 | 0.004 | 0.001 | 0.001 | 0.000 | 0.000 |

Table 6 Flow regime map at $\tau$ =1.0 s

| K | Read the following Table using Table 1 in Ch.1 | | | | | | | | | | |
|---|---|---|---|---|---|---|---|---|---|---|---|
| 11 | 14 | 14 | 14 | 14 | 14 | 16 | 16 | 16 | 07 | 07 | 07 |
| 10 | 14 | 14 | 14 | 14 | 16 | 16 | 16 | 16 | 16 | 16 | 16 |
| 9 | 16 | 16 | 16 | 16 | 16 | 16 | 16 | 16 | 16 | 16 | 16 |
| 8 | 16 | 16 | 16 | 16 | 16 | 16 | 16 | 16 | 16 | 16 | 16 |
| 7 | 16 | 16 | 16 | 16 | 16 | 16 | 16 | 16 | 16 | 16 | 15 |
| 6 | 16 | 16 | 16 | 16 | 16 | 16 | 16 | 16 | 16 | 15 | 15 |
| 5 | 16 | 16 | 16 | 16 | 16 | 16 | 16 | 16 | 15 | 15 | 15 |
| 4 | 16 | 16 | 16 | 16 | 16 | 16 | 16 | 16 | 15 | 15 | 15 |
| 3 | 16 | 16 | 16 | 16 | 16 | 16 | 16 | 16 | 15 | 15 | 15 |
| 2 | 16 | 16 | 16 | 16 | 16 | 16 | 16 | 16 | 16 | 16 | 16 |

Table 7 Solid particle temperature at $\tau$ =1.0 s

| K | | | | | | | | | | |
|---|---|---|---|---|---|---|---|---|---|---|
| 11 | 2489. | 2489. | 2489. | 2489. | 2487. | 2482. | 2478. | 2474. | 2469. | 2456. | 2500. |
| 10 | 2490. | 2489. | 2489. | 2489. | 2484. | 2481. | 2476. | 2474. | 2468. | 2422. | 2388. |
| 9 | 2488. | 2487. | 2487. | 2487. | 2483. | 2480. | 2474. | 2473. | 2465. | 2426. | 2382. |
| 8 | 2484. | 2483. | 2482. | 2482. | 2479. | 2472. | 2469. | 2464. | 2455. | 2422. | 2382. |
| 7 | 2479. | 2477. | 2478. | 2478. | 2476. | 2467. | 2465. | 2460. | 2446. | 2410. | 2375. |
| 6 | 2474. | 2472. | 2474. | 2473. | 2472. | 2464. | 2459. | 2451. | 2429. | 2393. | 2364. |
| 5 | 2470. | 2468. | 2469. | 2468. | 2468. | 2460. | 2450. | 2437. | 2407. | 2379. | 2361. |
| 4 | 2466. | 2463. | 2463. | 2464. | 2463. | 2456. | 2444. | 2426. | 2396. | 2374. | 2358. |
| 3 | 2461. | 2458. | 2458. | 2459. | 2454. | 2450. | 2440. | 2420. | 2393. | 2372. | 2357. |
| 2 | 2442. | 2435. | 2436. | 2438. | 2435. | 2427. | 2417. | 2401. | 2385. | 2377. | 2366. |

Table 8 Volumetric fraction of steam at $\tau$ =1.0 s

| K | | | | | | | | | | | |
|---|---|---|---|---|---|---|---|---|---|---|---|
| 11 | 0.694 | 0.694 | 0.695 | 0.695 | 0.996 | 0.996 | 0.988 | 0.977 | 0.961 | 0.911 | 0.974 |
| 10 | 0.761 | 0.762 | 0.763 | 0.763 | 0.994 | 0.993 | 0.986 | 0.972 | 0.951 | 0.872 | 0.933 |
| 9 | 0.782 | 0.800 | 0.807 | 0.810 | 0.986 | 0.990 | 0.981 | 0.962 | 0.928 | 0.841 | 0.575 |
| 8 | 0.833 | 0.838 | 0.846 | 0.849 | 0.983 | 0.988 | 0.977 | 0.948 | 0.897 | 0.782 | 0.545 |
| 7 | 0.863 | 0.863 | 0.869 | 0.872 | 0.979 | 0.986 | 0.968 | 0.922 | 0.830 | 0.641 | 0.453 |
| 6 | 0.876 | 0.876 | 0.884 | 0.888 | 0.976 | 0.984 | 0.963 | 0.889 | 0.717 | 0.463 | 0.391 |
| 5 | 0.877 | 0.881 | 0.892 | 0.899 | 0.972 | 0.982 | 0.961 | 0.843 | 0.382 | 0.400 | 0.380 |
| 4 | 0.873 | 0.881 | 0.880 | 0.905 | 0.970 | 0.980 | 0.960 | 0.770 | 0.311 | 0.418 | 0.361 |
| 3 | 0.855 | 0.826 | 0.799 | 0.817 | 0.861 | 0.941 | 0.958 | 0.690 | 0.391 | 0.487 | 0.356 |
| 2 | 0.226 | 0.290 | 0.302 | 0.340 | 0.575 | 0.589 | 0.585 | 0.592 | 0.571 | 0.664 | 0.544 |

Table 9 Volumetric fraction of water at $\tau$ =1.0 s

| K | | | | | | | | | | | |
|---|---|---|---|---|---|---|---|---|---|---|---|
| 11 | 0.000 | 0.000 | 0.000 | 0.000 | 0.000 | 0.004 | 0.012 | 0.023 | 0.039 | 0.089 | 0.026 |
| 10 | 0.000 | 0.000 | 0.000 | 0.000 | 0.000 | 0.006 | 0.014 | 0.028 | 0.049 | 0.128 | 0.067 |
| 9 | 0.030 | 0.012 | 0.007 | 0.005 | 0.006 | 0.009 | 0.019 | 0.038 | 0.072 | 0.159 | 0.423 |
| 8 | 0.014 | 0.011 | 0.006 | 0.003 | 0.004 | 0.009 | 0.023 | 0.051 | 0.103 | 0.218 | 0.453 |
| 7 | 0.006 | 0.008 | 0.005 | 0.003 | 0.004 | 0.011 | 0.030 | 0.078 | 0.169 | 0.358 | 0.545 |
| 6 | 0.008 | 0.011 | 0.006 | 0.004 | 0.004 | 0.011 | 0.036 | 0.110 | 0.283 | 0.536 | 0.605 |
| 5 | 0.017 | 0.017 | 0.009 | 0.005 | 0.005 | 0.011 | 0.037 | 0.155 | 0.616 | 0.598 | 0.616 |
| 4 | 0.026 | 0.021 | 0.027 | 0.002 | 0.004 | 0.012 | 0.036 | 0.227 | 0.685 | 0.579 | 0.635 |
| 3 | 0.012 | 0.047 | 0.086 | 0.084 | 0.103 | 0.045 | 0.035 | 0.305 | 0.604 | 0.509 | 0.640 |
| 2 | 0.001 | 0.019 | 0.021 | 0.046 | 0.021 | 0.146 | 0.208 | 0.269 | 0.351 | 0.303 | 0.435 |

Table 10 Volumetric fraction of solid particles at $\tau$ =1.0 s

| K | | | | | | | | | | | |
|---|---|---|---|---|---|---|---|---|---|---|---|
| 11 | 0.306 | 0.306 | 0.305 | 0.305 | 0.004 | 0.000 | 0.000 | 0.000 | 0.000 | 0.000 | 0.000 |
| 10 | 0.239 | 0.238 | 0.237 | 0.237 | 0.006 | 0.001 | 0.000 | 0.000 | 0.000 | 0.000 | 0.000 |
| 9 | 0.188 | 0.187 | 0.186 | 0.186 | 0.008 | 0.001 | 0.000 | 0.000 | 0.000 | 0.000 | 0.001 |
| 8 | 0.153 | 0.151 | 0.149 | 0.148 | 0.013 | 0.002 | 0.001 | 0.000 | 0.000 | 0.000 | 0.001 |
| 7 | 0.131 | 0.129 | 0.126 | 0.125 | 0.017 | 0.004 | 0.001 | 0.000 | 0.000 | 0.001 | 0.002 |
| 6 | 0.116 | 0.113 | 0.110 | 0.108 | 0.020 | 0.005 | 0.002 | 0.001 | 0.001 | 0.001 | 0.003 |
| 5 | 0.106 | 0.102 | 0.099 | 0.097 | 0.023 | 0.006 | 0.003 | 0.002 | 0.002 | 0.002 | 0.004 |
| 4 | 0.100 | 0.098 | 0.093 | 0.093 | 0.027 | 0.008 | 0.004 | 0.003 | 0.004 | 0.003 | 0.005 |
| 3 | 0.133 | 0.126 | 0.115 | 0.099 | 0.036 | 0.014 | 0.007 | 0.005 | 0.005 | 0.004 | 0.004 |
| 2 | 0.773 | 0.690 | 0.677 | 0.615 | 0.403 | 0.264 | 0.208 | 0.139 | 0.079 | 0.033 | 0.021 |

Table 11 Flow regime map at $\tau = 1.5$ s

| K | Read the following Table using Table 1 in Ch.1 |
|---|---|
| 11 | 14 14 14 14 16 16 16 16 07 07 07 |
| 10 | 14 14 14 16 16 16 16 16 16 07 16 |
| 9 | 14 14 14 16 16 16 16 16 16 07 16 |
| 8 | 14 14 14 16 16 16 16 16 16 16 16 |
| 7 | 14 14 14 16 16 16 16 16 16 16 16 |
| 6 | 14 14 14 16 16 16 16 16 16 16 16 |
| 5 | 14 14 16 16 16 16 16 16 16 16 16 |
| 4 | 14 16 16 16 16 16 16 16 16 16 16 |
| 3 | 16 16 16 16 16 16 16 16 16 16 16 |
| 2 | 16 16 16 16 16 16 16 16 16 16 16 |

Table 12 Solid particle temperature at $\tau = 1.5$ s

| K | |
|---|---|
| 11 | 2489. 2489. 2489. 2489. 2486. 2483. 2478. 2474. 2469. 2456. 2500. |
| 10 | 2489. 2488. 2488. 2486. 2483. 2481. 2476. 2474. 2468. 2422. 2388. |
| 9 | 2487. 2487. 2487. 2484. 2481. 2478. 2476. 2473. 2465. 2426. 2336. |
| 8 | 2485. 2484. 2484. 2479. 2477. 2475. 2471. 2467. 2455. 2426. 2338. |
| 7 | 2483. 2481. 2481. 2475. 2473. 2471. 2466. 2463. 2453. 2425. 2341. |
| 6 | 2482. 2480. 2479. 2471. 2469. 2467. 2462. 2458. 2447. 2410. 2346. |
| 5 | 2480. 2477. 2476. 2467. 2466. 2464. 2459. 2453. 2432. 2393. 2341. |
| 4 | 2478. 2473. 2472. 2464. 2464. 2460. 2456. 2447. 2416. 2379. 2332. |
| 3 | 2471. 2468. 2467. 2460. 2461. 2458. 2454. 2444. 2409. 2373. 2320. |
| 2 | 2451. 2444. 2444. 2445. 2443. 2436. 2424. 2410. 2388. 2365. 2335. |

Table 13 Volumetric fraction of gas $\tau = 1.5$ s

| K | |
|---|---|
| 11 | 0.694 0.694 0.695 0.695 0.996 0.997 0.991 0.979 0.955 0.772 0.965 |
| 10 | 0.762 0.762 0.763 0.764 0.993 0.992 0.980 0.956 0.905 0.851 0.957 |
| 9 | 0.812 0.813 0.813 0.813 0.989 0.982 0.955 0.905 0.849 0.842 0.864 |
| 8 | 0.847 0.849 0.850 0.847 0.979 0.956 0.908 0.860 0.838 0.856 0.890 |
| 7 | 0.868 0.870 0.872 0.867 0.967 0.890 0.843 0.857 0.878 0.892 0.908 |
| 6 | 0.883 0.885 0.887 0.875 0.902 0.807 0.880 0.917 0.939 0.916 0.899 |
| 5 | 0.894 0.896 0.898 0.840 0.805 0.886 0.940 0.962 0.968 0.918 0.875 |
| 4 | 0.904 0.906 0.906 0.871 0.838 0.958 0.973 0.984 0.977 0.896 0.810 |
| 3 | 0.855 0.857 0.843 0.819 0.898 0.991 0.993 0.976 0.982 0.895 0.716 |
| 2 | 0.000 0.043 0.125 0.178 0.170 0.345 0.525 0.570 0.579 0.610 0.551 |

Table 14 Volumetric fraction of water $\tau = 1.5$ s

| K | | | | | | | | | | | |
|---|---|---|---|---|---|---|---|---|---|---|---|
| 11 | 0.000 | 0.000 | 0.000 | 0.000 | 0.000 | 0.003 | 0.009 | 0.021 | 0.045 | 0.228 | 0.035 |
| 10 | 0.000 | 0.000 | 0.000 | 0.000 | 0.001 | 0.007 | 0.019 | 0.044 | 0.095 | 0.149 | 0.043 |
| 9 | 0.000 | 0.000 | 0.000 | 0.002 | 0.003 | 0.017 | 0.045 | 0.095 | 0.151 | 0.158 | 0.135 |
| 8 | 0.000 | 0.000 | 0.000 | 0.004 | 0.010 | 0.042 | 0.092 | 0.140 | 0.162 | 0.144 | 0.110 |
| 7 | 0.000 | 0.000 | 0.000 | 0.007 | 0.020 | 0.108 | 0.157 | 0.143 | 0.122 | 0.108 | 0.092 |
| 6 | 0.000 | 0.000 | 0.000 | 0.014 | 0.082 | 0.189 | 0.119 | 0.082 | 0.061 | 0.084 | 0.100 |
| 5 | 0.000 | 0.000 | 0.000 | 0.062 | 0.177 | 0.110 | 0.059 | 0.037 | 0.032 | 0.082 | 0.125 |
| 4 | 0.000 | 0.000 | 0.002 | 0.039 | 0.143 | 0.038 | 0.025 | 0.016 | 0.023 | 0.104 | 0.189 |
| 3 | 0.000 | 0.004 | 0.028 | 0.077 | 0.083 | 0.005 | 0.006 | 0.024 | 0.018 | 0.105 | 0.282 |
| 2 | 0.000 | 0.003 | 0.014 | 0.024 | 0.008 | 0.000 | 0.057 | 0.136 | 0.204 | 0.218 | 0.212 |

Table 15 Volumetric fraction of solid particles $\tau = 1.5$ s

| K | | | | | | | | | | | |
|---|---|---|---|---|---|---|---|---|---|---|---|
| 11 | 0.306 | 0.306 | 0.305 | 0.305 | 0.004 | 0.000 | 0.000 | 0.000 | 0.000 | 0.000 | 0.000 |
| 10 | 0.238 | 0.238 | 0.237 | 0.236 | 0.006 | 0.000 | 0.000 | 0.000 | 0.000 | 0.000 | 0.000 |
| 9 | 0.188 | 0.187 | 0.187 | 0.185 | 0.008 | 0.001 | 0.000 | 0.000 | 0.000 | 0.000 | 0.000 |
| 8 | 0.153 | 0.151 | 0.150 | 0.148 | 0.011 | 0.001 | 0.000 | 0.000 | 0.000 | 0.000 | 0.000 |
| 7 | 0.132 | 0.130 | 0.128 | 0.126 | 0.013 | 0.002 | 0.001 | 0.000 | 0.000 | 0.000 | 0.001 |
| 6 | 0.117 | 0.115 | 0.113 | 0.110 | 0.016 | 0.003 | 0.001 | 0.000 | 0.000 | 0.000 | 0.001 |
| 5 | 0.106 | 0.104 | 0.102 | 0.099 | 0.018 | 0.004 | 0.001 | 0.000 | 0.000 | 0.000 | 0.001 |
| 4 | 0.096 | 0.093 | 0.092 | 0.090 | 0.019 | 0.004 | 0.001 | 0.001 | 0.000 | 0.000 | 0.001 |
| 3 | 0.145 | 0.139 | 0.129 | 0.104 | 0.019 | 0.004 | 0.001 | 0.000 | 0.000 | 0.000 | 0.001 |
| 2 | 1.000 | 0.954 | 0.861 | 0.798 | 0.821 | 0.655 | 0.418 | 0.294 | 0.218 | 0.172 | 0.238 |

## NOMENCLATURE

| Symbol | Dimension | Meaning |
|---|---|---|
| A | $m^2$ | cross section |
| A,a | – | matrix, constant |
| a | $m^2/s$ | thermal diffusivity |
| a | m/s | speed of sound |
| B,b | – | matrix, constant |
| $C_{nl}$ | – | mass concentration of the inert component n in the velocity field l |
| $C_{Ml}$ | – | mass concentration of the not inert component M in the velocity field l |
| C,c | – | vector, constant |
| $c_p$ | J/(kgK) | specific heat at constant pressure |
| D,d | m | diameter |
| D* | $m^2/s$ | diffusivity |
| $D^s$ | $Km^2/s$ | diffusivity based on entropy driving force |
| d | – | total differential |
| $(\rho w)_{32}$ | $kg/(m^2s)$ | mass flow rate perpendicular to the interface – drop deposition |
| E | – | unit matrix |
| e | J/kg | specific internal energy |
| F | N | force |
| f | $N/m^3$ | force per unit mixture volume |
| =F,f(... | – | function of (... |
| f | 1/s | frequency |
| G | $kg/(m^2s)$ | mass flow rate |
| g | $m/s^2$ | gravitational acceleration |
| H | J | enthalpy |
| h | J/kg | specific enthalpy |
| j | m/s | volume flux density |
| k | m | roughness |
| k | J/kg | specific kinetic energy of the turbulent pulsations |
| n | $m^{-3}$ | number of nuclei per unit flow volume, number of particles per unit flow volume |
| $\dot{n}$ | $1/(m^3s)$ | change of the number of nuclei or particles per unit time and unit volume of the mixture |
| $P_k$ | J/kg | direct dissipation of kinetic energy and simultaneous direct production of turbulent kinetic energy per unit mass |
| p | Pa | pressure |
| $\dot{q}'''$ | $W/m^3$ | thermal power per unit flow volume |
| | | Postulated interface heat transfer in IVA3: |

$\dot{q}_1''' = \dot{q}_{w1}''' - \dot{q}_{13}''' - \dot{q}_{12}''' + \dot{q}_{i21}''' + \dot{q}_{i31}'''$ thermal power per cubic meter of the mixture introduced into the first velocity field

$\dot{q}_{w1}'''$ $W/m^3$ thermal power per cubic meter of the mixture introduced into the first velocity field from the wall

$\dot{q}_{13}'''$ $W/m^3$ thermal power per cubic meter of the mixture transported from the first into the third velocity field

$\dot{q}_{12}'''$ $W/m^3$ thermal power per cubic meter of the mixture transported from the first into the second velocity field

$\dot{q}_{23}'''$ $W/m^3$ thermal power per cubic meter of the mixture transported from the second into the third velocity field

$\dot{q}_{i21}'''$ $W/m^3$ thermal power per cubic meter of the mixture transported from the interface of the second velocity field into the first velocity field due to mass transfer processes

$\dot{q}_{i31}'''$ $W/m^3$ thermal power per cubic meter of the mixture transported from the interface of the third velocity field into the first velocity field due to mass transfer processes

$\dot{q}_2''' = \dot{q}_{w2}''' - \dot{q}_{23}''' + \dot{q}_{12}''' + \dot{q}_{i2}'''$ thermal power per cubic meter of the mixture introduced into the second velocity field

$\dot{q}_{w2}'''$ $W/m^3$ thermal power per cubic meter of the mixture introduced into the second velocity field from the wall

$\dot{q}_{23}'''$ $W/m^3$ thermal power per cubic meter of the mixture transported from the second into the third velocity field

$\dot{q}_{i2}'''$ $W/m^3$ thermal power per cubic meter of the mixture transported from the interface of the second velocity field into the bulk of the second velocity field due to mass transfer processes

$\dot{q}_3''' = \dot{q}_{w3}''' + \dot{q}_{13}''' + \dot{q}_{i3}'''$ thermal power per cubic meter of the mixture introduced into the third velocity field

$\dot{q}_{w3}'''$ $W/m^3$ thermal power per cubic meter of the mixture introduced into the third velocity field from the wall

$\dot{q}_{i3}'''$ $W/m^3$ thermal power per cubic meter of the mixture transported from the interface of the third velocity field into the bulk of the third velocity field due to mass transfer processes

| | | |
|---|---|---|
| $\dot{q}''$ | $W/m^2$ | heat flux density |
| R | $N/m^3$ | pressure drop per unit length due to friction |
| R | J/(kgK) | (with indexes) gas constant |
| r | m | radius |
| s | J/(kgK) | specific entropy |
| T | K | absolute temperature |
| t | C | temperature |
| U | – | dependent variable vector |
| u | m/s | radial velocity |
| V | m/s | velocity vector |
| v | m/s | azimuthal velocity |
| v | $m^3/kg$ | specific volume |
| z | m | axial coordinate |

Greek

| | | |
|---|---|---|
| $\alpha_l$ | $m^3/m^3$ | volume fraction of field l in the flow mixture |
| $\alpha$ | $W/(m^2K)$ | heat transfer coefficient |
| $\gamma_v$ | – | volume porosity |
| $\gamma_{r,\theta,z}$ | – | permeabilities in r, $\theta$, and z directions |
| $\Delta$ | – | finite difference |
| $\Delta u$, $\Delta v$, $\Delta w$ | m/s | diffusion velocities in r, $\theta$, and z directions |
| $\delta$ | – | small deviation with respect to the average value |
| $\partial$ | – | partial differential |
| $(\rho w)_{23}$ | $kg/(m^2s)$ | entrainment mass flow rate perpendicular to the interface |
| $\epsilon$ | J/kg | dissipated kinetic energy of turbulent pulsations |
| $\varphi$ | rad | angle between upward vertical direction and V |
| $\zeta,\lambda_R$ | – | friction coefficient |
| $\eta$ | kg/(ms) | dynamic viscosity |
| $\theta$ | rad | azimuth a coordinate |
| $\kappa$ | – | isentropic exponent |
| $\lambda$ | W/(mK) | thermal conductivity |
| $\mu$ | $kg/(m^3s)$ | mass source term for velocity field l (mass introduced into the field l per unit time and unit mixture volume) |
| $\nu$ | $m^2/s$ | kinematic viscosity |
| $\Pi$ | m | perimeter |
| $\pi$ | – | 3.141592.... |
| $\rho$ | $kg/m^3$ | density; without indeces: mixture density |
| $\Sigma$ | – | sum |
| $\sigma$ | N/m | surface tension |
| $\tau$ | s | time |
| $\tau$ | $N/m^2$ | with indeces – tension |

Dimensionles numbers

| | |
|---|---|
| Ar | Archimed number |
| Fo | Fourier number |
| Fr | Froude number |
| Gb | Gibbs number |
| Gr | Grashof number |
| Ku | Kutateladze number |
| La | capillary constant of Laplace |
| Le | Lewis number |
| M | Mach number |
| Nu | Nusselt number |
| Pe | Peclet number |
| Pr | Prandtl number |
| Ra | Rayleigh number |
| Re | Reynolds number |
| Sc | Schmidt number |
| Sh | Sherwood number |
| Sp | Spalding number |
| We | Weber number |
| Z | Zeldovich number |

Superscripts

| | |
|---|---|
| ''' | saturated solid |
| '' | saturated steam |
| ' | saturated liquid |
| ' | for velocities: fluctuation |
| n | for the time $\tau$ |
| n+1 | for the time $\tau+\Delta\tau$ |
| t | turbulent |
| l | laminar |

Subscripts

| | |
|---|---|
| A | outsides of the definition region |
| nl | inert component (either non condensing gas or solid particles) of the velocity field l |
| Ml | not inert component (e.g. water or water steam) |
| l | velocity field l |
| i,j,k | integer indeces for the three coordinates r, $\theta$, z |
| w | wall |
| c | continuous |
| d | dispersed |
| h | hydraulic |
| heat | heated |
| 1 | gas, bubble |
| 2 | continuous liquid plus microscopic solid particles |
| 3 | dispersed liquid plus microscopic solid particles, drops |

Summary of all thermodynamic and thermophysical properties needed for the description of multiphase flows consisting of water, steam, air and metallic materials being in liquid or in liquid–solid or in solid state.

Water–steam saturation line

| | | |
|---|---|---|
| $T'$ | K | saturation temperature at system pressure. |
| $v'$ | $m^3/kg$ | water specific volume at the saturation line. |
| $v''$ | $m^3/kg$ | steam specific volume at the saturation line. |
| $h'$ | J/kg | specific water enthalpy at the saturation line. |
| $h''$ | J/kg | specific steam enthalpy at the saturation line. |
| $h''-h'$ | J/kg | latent heat of vaporization. |
| $s'$ | J/(kgK) | specific water entropy at the saturation line. |
| $s''$ | J/(kgK) | specific steam entropy at the saturation line. |
| $dT'/dp$ | K/Pa | derivative of the temperature with respect to pressure at the saturation line. |
| $c'_p$ | J/(kgK) | water specific heat at constant pressure at the saturation line. |
| $c''_p$ | J/(kgK) | steam specific heat at constant pressure at the saturation line. |
| $\eta'$ | kg/(ms) | water dynamic viscosity at the saturation line. |
| $\eta''$ | kg/(ms) | steam dynamic viscosity at the saturation line. |
| $\lambda'$ | kg/(ms) | water thermal conductivity at the saturation line. |
| $\lambda''$ | kg/(ms) | steam thermal conductivity at the saturation line. |
| $\sigma'$ | N/m | surface tension water steam at the saturation line. |

The above mentioned properties can be computed either as a function of temperature T' in K or as a function of pressure P' in Pa, respectively.

The thermodynamic and thermophysical properties of water are computed as functions of temperature in K and system pressure in Pa:

| | | |
|---|---|---|
| $\rho_{lM}$ | $kg/m^3$ | density. |
| $h_{lM}$ | J/kg | specific enthalpy. |
| $s_{lM}$ | J/(kgK) | specific entropy. |
| $c_{plM}$ | J/(kgK) | specific heat at constant pressure. |
| $a_{lM}$ | m/s | velocity of sound. |
| $\eta_{lM}$ | kg/(ms) | dynamic viscosity. |
| $\lambda_{lM}$ | W/(mK) | thermal conductivity. |
| $Pr_{lM}$ | – | Prandtl number. |
| $(\frac{\partial h_{lM}}{\partial p})_{T_l}$ | (J/kg)/Pa | specific enthalpy derivative with respect to pressure at constant temperature. |

| | | |
|---|---|---|
| $(\frac{\partial \rho_{1M}}{\partial T_1})_p$ | $kg/(m^3K)$ | density derivative with respect to the temperature at constant pressure. |
| $(\frac{\partial \rho_{1M}}{\partial p})_{T_1}$ | $(kg/m^3)/Pa$ | density derivative with respect to the pressure at constant temperature. |
| $\sigma_{1M}$ | N/m | surface tension metallic phase/gas. |

The thermodynamic and thermophysical properties of air are computed as a function of temperature $T_1$ in K and partial pressure $p_{1n}$ in Pa:

| | | |
|---|---|---|
| $\rho_{1n}$ | $kg/m^3$ | density. |
| $h_{1n}$ | J/kg | specific enthalpy. |
| $s_{1n}$ | J/(kgK) | specific entropy. |
| $c_{p1n}$ | J/(kgK) | specific heat at constant pressure. |
| $a_{1n}$ | m/s | velocity of sound. |
| $\eta_{1n}$ | kg/(ms) | dynamic viscosity. |
| $\lambda_{1n}$ | W/(mK) | thermal conductivity. |
| $Pr_{1n}$ | – | Prandtl number. |

The thermodynamic and thermophysical properties of steam are computed as functions of temperature T in K and of the partial pressure $P_{1M}$ in Pa:

| | | |
|---|---|---|
| $\rho_{1M}$ | $kg/m^3$ | density. |
| $h_{1M}$ | J/kg | specific enthalpy. |
| $s_{1M}$ | J/(kgK) | specific entropy. |
| $c_{p1M}$ | J/(kgK) | specific heat at constant pressure. |
| $a_{1M}$ | m/s | velocity of sound. |
| $\eta_{1M}$ | kg/(ms) | dynamic viscosity. |
| $\lambda_{1M}$ | W/(mK) | thermal conductivity. |
| $Pr_{1M}$ | – | Prandtl number. |
| $(\frac{\partial h_{1M}}{\partial p})_{T_1}$ | (J/kg)/Pa | specific enthalpy derivative with respect to pressure at constant temperature. |
| $(\frac{\partial \rho_{1M}}{\partial T_1})_{p_{1M}}$ | $kg/(m^3K)$ | density derivative with respect to the temperature at constant pressure. |

| | | |
|---|---|---|
| $(\frac{\partial \rho_{1M}}{\partial p_{1M}})_{T_1}$ | $(kg/m^3)/Pa$ | density derivative with respect to the pressure at constant temperature. |

The properties of a binary mixture consisting of inert (solid particles) and not inert (water) components are computed as functions of the field temperature $T_l$ in K, system pressure p in Pa, and inert mass concentration $C_{ln}$ (where l=2,3):

| | | |
|---|---|---|
| $s_l$ | J/(kgK) | specific entropy. |
| $h_{lM}$ | J/kg | specific water enthalpy. |
| $\rho_l$ | $kg/m^3$ | density. |
| $a_l$ | m/s | velocity of sound. |
| $(\frac{\partial \rho_l}{\partial s_l})_{p,C_{ln}}$ | $(kg/m^3)/(J/kgK)$ | density derivative with respect to the specific entropy at constant pressure and inert mass concentrations. |
| $(\frac{\partial \rho_l}{\partial C_{ln}})_{p,s_l}$ | $(kg/m^3)$ | density derivative with respect to the inert mass concentration at constant pressure and specific entropy. |
| $(\frac{\partial T_l}{\partial s_l})_{p,C_{ln}}$ | K/[J/(kgK)] | temperature derivative with respect to the specific entropy at constant pressure and inert mass concentration. |
| $(\frac{\partial T_l}{\partial p})_{s_l,C_{ln}}$ | K/Pa | temperature derivative with respect to the pressure at constant specific entropy and inert mass concentrations. |
| $(\frac{\partial T_l}{\partial C_{ln}})_{p,s_l}$ | K | temperature derivative with respect to the inert mass concentration at constant pressure and specific entropy. |
| $c_{pl}$ | J/(kgK) | specific heat at constant pressure. |
| $\eta_l$ | kg/(ms) | dynamic viscosity. |
| $\lambda_l$ | W/(mK) | thermal conductivity. |
| $Pr_l$ | – | Prandtl number. |
| $\sigma_l$ | N/m | surface tension metallic phase/gas. |
| $s_{ln}$ | J/(kgK) | specific entropy of the inert component. |
| $s_{lM}$ | J/(kgK) | specific entropy of the water component. |
| $h_{ln}$ | J/kg | specific enthalpy of the inert component. |

The properties of a binary gas mixture consisting of inert component (air) and not inert component (steam) are computed as functions of the gas temperature $T_l$ in K, of the system pressure p in Pa and of the inert mass concentration $C_{ln}$:

| | | |
|---|---|---|
| $s_1$ | J/(kgK) | specific entropy. |
| $h_{1M}$ | J/kg | specific steam enthalpy. |
| $\rho_1$ | kg/m$^3$ | density. |
| $a_1$ | m/s | velocity of sound. |
| $(\frac{\partial \rho_1}{\partial s_1})_{p,C_{1n}}$ | (kg/m$^3$)/(J/kgK) | density derivative with respect to the specific entropy at constant pressure and inert mass concentration. |
| $(\frac{\partial \rho_1}{\partial C_{1n}})_{p,s_1}$ | (kg/m$^3$) | density derivative with respect to the inert mass concentration at constant pressure and specific entropy. |
| $(\frac{\partial T_1}{\partial s_1})_{p,C_{1n}}$ | K/[J/(kgK)] | temperature derivative with respect to the specific entropy at constant pressure and inert mass concentration. |
| $(\frac{\partial T_1}{\partial p})_{s_1,C_{1n}}$ | K/Pa | temperature derivative with respect to the pressure at constant specific entropy and inert mass concentrations. |
| $(\frac{\partial T_1}{\partial C_{1n}})_{p,s_1}$ | K | temperature derivative with respect to the inert mass concentration at constant pressure and specific entropy. |
| $c_{p1}$ | J/(kgK) | specific heat at constant pressure. |
| $\eta_1$ | kg/(ms) | dynamic viscosity. |
| $\lambda_1$ | W/(mK) | thermal conductivity. |
| $Pr_1$ | – | Prandtl number. |
| $D_{1n}$ | m$^2$/s | diffusion constant of air in steam. |
| $p_{1n}$ | Pa | partial pressure of the inert component. |
| $s_{1n}$ | J/(kgK) | specific entropy of the inert component. |
| $s_{1M}$ | J/(kgK) | specific entropy of the steam component. |
| $h_{1n}$ | J/kg | specific enthalpy of the inert component. |

The quantities describing the solid–liquid transition are computed as functions of the temperature in K:

| | | |
|---|---|---|
| $T''_{3n}$ | K | liquidus temperature. |
| $\rho''_{3n}$, | kg/m$^3$ | saturated solid phase density. |
| $\rho''_{3n}$ | kg/m$^3$ | saturated liquid density. |
| $d\rho''_{3n}/dT_3$ | kg/(m$^3$K) | density derivative with respect to temperature at the two phase/solid transition line. |

| | | |
|---|---|---|
| $d\rho''_{3n}/dT_3$ | $kg/(m^3K)$ | density derivative with respect to temperature at the liquid/two phase transition line. |
| $h'''_{3n}$ | J/kg | saturated solid phase specific enthalpy. |
| $h''_{3n}$ | K/kg | saturated liquid phase specific enthalpy. |
| $h''_{3n}-h'''_{3n}$ | J/kg | latent heat of solidification. |
| $s'''_{3n}$ | J/(kgK) | saturated solid phase specific entropy. |
| $s''_{3n}$ | J/(kgK) | saturated liquid phase specific entropy. |
| $s''_{3n}-s'''_{3n}$ | J/(kgK) | latent specific solidification entropy. |
| $c'''_{p3n}$ | J/(kgK) | specific heat at constant pressure of the saturated solid phase. |
| $c''_{p3n}$ | J/(kgK) | specific heat at constant pressure of the saturated liquid phase. |
| $\eta'''_{3n}$ | kg/(ms) | saturated solid phase dynamic density. |
| $\eta''_{3n}$ | kg/(ms) | saturated liquid phase dynamic viscosity. |
| $\lambda'''_{3n}$ | W/(mK) | saturated solid phase thermal conductivity. |
| $\lambda''_{3n}$ | W/(mK) | saturated liquid phase thermal conductivity. |
| $\sigma''_{3n}$ | N/m | surface tension liquid metal/gas. |

For description of the thermophysical properties of solid and liquid materials the following approximations are necessary:

| | | |
|---|---|---|
| $T_{3n}$ | K | temperature of the liquid metal as a function of specific entropy in J/(kgK). |
| $\sigma_{3n,solid}$ | N/m | surface tension of the liquid metal as a function of temperature in K. |
| $\eta_{3n,solid}$ | kg/(ms) | solid phase dynamic viscosity as a function of temperature in K. |
| $h_{3n,solid}$ | J/kg | specific enthalpy of the solid phase as a function of temperature in K. |
| $h_{3n,liquid}$ | J/kg | specific liquid metal enthalpy as a function of temperature in K. |
| $c_{p3n,solid}$ | J/(kgK) | specific heat at constant pressure for solid phase as a function of temperature in K. |
| $c_{p3n,liquid}$ | J/(kgK) | specific heat at constant pressure for liquid metal as a function of temperature in K. |

| | | |
|---|---|---|
| $s_{3n,solid}$ | J/(kgK) | specific solid phase entropy as a function of temperature in K. |
| $s_{3n,liquid}$ | J/(kgK) | specific liquid metal entropy as a function of the temperature in K. |
| $\rho_{3n,solid}$ | kg/m$^3$ | solid phase density as a function of temperature in K. |
| $\frac{d\rho_{3n,solid}}{dT_3}$ | kg/(m$^3$K) | solid density derivatives with respect to the temperature as a function of temperature in K. |
| $\rho_{3n,liquid}$ | kg/m$^3$ | liquid metal density as a function of temperature in K. |
| $\frac{d\rho_{3n,liquid}}{dT_3}$ | kg/(m$^3$K) | liquid metal density derivatives with respect to the temperature as a function of temperature in K. |
| $\lambda_{3n,solid}$ | W/(mK) | solid phase thermal conductivity as a function of temperature in K. |
| $\lambda_{3n,liquid}$ | W/(mK) | liquid metal thermal conductivity as a function of temperature. |

Having the entropy one checks in which state the metallic, velocity field is and computes properties either for liquid state or for two–phase liquid–solid equilibrium state or for solid state. The following properties as functions of temperature in K and/or of the specific entropy in J/(kgK) are the result:

| | | |
|---|---|---|
| $\rho_{3n}$ | kg/m$^3$ | density. |
| $h_{3n}$ | J/kg | specific enthalpy. |
| $c_{p3n}$ | J/(kgK) | specific heat at constant pressure. |
| $a_{3n}$ | m/s | velocity of sound. |
| $\eta_{3n}$ | kg/(ms) | dynamic viscosity. |
| $\lambda_{3n}$ | W/(mK) | thermal conductivity. |
| $Pr_{3n}$ | – | Prandtl number. |
| $(\frac{\partial h_{3n}}{\partial p})_{T_3}$ | (J/kg)/Pa | specific enthalpy derivative with respect to pressure at constant temperature. |
| $(\frac{\partial \rho_{3n}}{\partial T_3})_p$ | kg/(m$^3$K) | density derivative with respect to the temperature at constant pressure. |

| | | |
|---|---|---|
| $(\frac{\partial \rho_{3n}}{\partial p})_{T_3}$ | $(kg/m^3)/Pa$ | density derivative with respect to the pressure at constant temperature. |
| $\sigma_{3n}$ | N/m | surface tension metallic phase/gas. |

## REFERENCES

1. J. C. SLATTERY, Interfacial Transport Phenomena, Springer Verlag, 1990.

2. V. P. SKRIPOV, E. N. SINZIN, P. A. PAVLOW et al., Thermal Physical Properties of Liquids in Metastable State, Moskva, Atomisdat (1980). In Russian: Скрипов, В.П.; Е.Н.Синицын, П.А.Павлов и др.: Топлофизические свойства жидкостей в метастабильном состоянии, Москва: Атомиздат (1980)

3. G. HETSRONI, Handbook of Multiphase Systems. Hemisphere Publ. Corp., Washington etc., McGraw–Hill Book Company, New York etc. (1982).

4. W. M. ROHSENOW, J. P. HARTNETT and E. N. GANIC eds., Handbook of Heat Transfer Fundamentals (1985), McGraw Hill.

5. R. K. SHAH, E. N. GANIC and K. T. YANG eds., Experimental Heat Transfer, Fluid Mechanics, and Thermodynamics, (1988) Elsevier

6. K. MISHIMA and M. ISHII, Flow Regime Transition Criteria for Upward Two–Phase Flow in Vertical Tubes, Int. J. Heat Mass Transfer. Vol.27, No.5 (1984) pp.723–737

7. I. KATAOKA and M ISHII, Mechanism and Correlation of Droplet Entrainment and Deposition in Annular Two–Phase Flow. NUREG/CR–2885, ANL–82–44 (July 1982).

8. I. I. PALEEV and B. S. FILIPOVICH, Phenomena of Liquid Transfer in Two–Phase Dispersed Annular Flow. Int. J. Heat Mass Transfer 9 (1966) p.1089.

9. Y. AHMAD, Axial Distribution of Bulk Temperature and Void Fraction in a Heated Channel with Inlet Subcooling, J. Heat Transfer, 92 (1970) 595.

10. G. DE JARLAIS, M. ISHII and J. LINEHAN, Hydrodynamic Stability of Inverted Annular Flow in an Adiabatic Simulation, Transactions of the ASME, Journal of Heat Transfer, Vol.108, Febr.1986, pp.84–92.

11. M. EPSTEIN and K. FAUSKE, Steam Film Instability and the Mixing of Core–Melt Jets and Water, ANS Proceedings, 1985 National Heat Transfer Conference, August 4–7, 1985, Denver, Colorado, pp. 277–284.

12. M. PILCH, C. A. ERDMAN and A. B. REYNOLDS, Acceleration Induced Fragmentation of Liquid Drops, NUREG/CR–2247/ Charlottesville, VA: Department of Nucl. Eng., University of Virginia, August 1981.

13. W. RANZ and W. MARSCHAL Jr., Evaporation from Drops, Ch. Eng. Progress, Vol.48(1952)pp.141–146

14. V. K. DHIR et al., Laminar Film Condensation on Flat and Axisymmetric Bodies in Non Uniform Gravitational Field, Teploenergetika 1 (1972) p.100, Mir, In Russian: Дир, Линхард: Ламинарная пленочная конденсация на плоских и осесимметричных телах в неоднородном гравитационном поле. Теплопередача, Но 1(1972)стр.100, "Мир"

15. M. TANAKA, Heat Transfer of a Spray Droplet in a Nuclear Reactor Containment. Nuclear Technology. Vol.47 (Feb. 1980) p.268.

16. R. I. NIGMATULIN, Basics of the Mechanics of the Heterogeneous Fluids, Moskva, Nauka, 1978. In Russian: Нигматулин, Р.И.: Основый механики гетерогенных сред. Москва, Наука (1978).

17. D. A. LABUNZOV and A. P. KRUKOV, Process of Intensive Flashing, Teploenergetika Vol 24, 4 (1977) pp.8–11. In Russian: Лабунцов, Д.А.; А.П.Крюков: Процессы интенсивного испарения, Теплоенергетика 24(4)(1977)стр.8–11

18. L. D. HUNT, The effect of delayed bubble growth on the depressurisation of vessels containing hight temperature water. UKAEA Report AHSB(S) R 189 (1970)

19. J. ISENBERG and S. SIEDEMAN, Direct contact heat transfer with change of phase: Bubble condensation in immiscible liquids, Int. J. Heat Mass Transfer, Vol.13, June 1970, pp. 997–1011

20. H. HAUSEN, Darstellung des Waermeuebergangesin Roehren durch verallgemeinerte Potenzgleichungen. Verfahrenstechnik 9 H.4/5 (1958) 75–79.

21. A. A. SONIN, A. SHIMKO and J.–H.CHUN, Vapor condensation rate as a function of liquid–side turbulence, Int. J. Heat Mass Transfer, Vol.29, No.9(1986) pp.1319–1332

22. VDI–Waermeatlas, 4. Auflage 1984, VDI–Verlag.

23. Z. L. MIROPOLSKIJ, Heat Transfer in Film Boiling of Steam–Water Mixture in Steam Generating Tubes. Teploenergetika Vol.10 No.5 (1963) pp.49–53.

24. V. K. DHIR and G. P. PUROHIT, Subcooled Film–Boiling Heat Transfer From Spheres, Nuclear Engineering and Design 47(1978)49–66.

25. T. H. K. FREDERKING, Laminar Two–Phase Boundary Layers in Natural Convection Film Boiling of Subcooled Liquids, J. of Applied Math. and Phys., Vol.15 (1964) pp. 388 – 399.

26. J. P. HOLMAN, Heat Transfer. Third Edition, McGraw–Hill Book Company, New York (1972).

27. N. I. KOLEV, IVA2 Ein Computerprogramm zur Modellierung transienter 3D – Dreiphasen Dreikomponenten Stroemungen mittels drei Geschwindigkeitsfeldern in zylindrischer Geometrie mit beliebigen Einbauten einschliesslich der Spaltzone eines PWR/BWR, KfK 4088 (1986).

28. I. E. IDELCHIK, Handbook of Hydraulic Resistances, Moskva, Energia 1975, In Russian: Иделчик И. Е.: Справочник о гидравлических сопротивлениям. Москва Енергия (1975).

29. L. FRIEDEL, New Friction Pressure Drop Correlations for Upward, Horizontal, and Downward Two – Phase Pipe Flow. Presented at the HTFS Symposium, Oxford, September 1979 (Hoechst AG Reference No. 372217/24 698).

30. R. C. MARTINELLI and D. B. NELSON, Prediction of Pressure Drop During Forced / Circulation Boiling of Water, Trans. Am. Mech. Engrs 70, 695 – 702 (1948).

31. M. ISHII and T. C. CHAWLA: Local Drag Laws in Dispersed Two–Phase Flow, NUREG/CR–1230, ANL–79–105 (Dec.1979)

32. N. I. KOLEV, A. TOMIYAMA, T. SAKAGUCHI, Mathematical Modeling of the Mechanical Interaction Between the Velocity Fields in Three Phase Flow, Experimental Thermal and Fluid Science, subm. for publication (1990).

33. S. ERGUN, Fluid Flow Through Packed Columns, Chem. Eng. Prog. Vol. 48, No.2 (1952) 89–94.

34. R. J. LEPINSKI, A Coolability Model for Postaccident Nuclear Reactor Debris, Nucl. Technology Vol. 65 (Apr. 1984) 53–66.

35. G. G. BROWN et al., Unit Operations, J. Wiley and Sons, Inc., New York (1950) pp. 210–228.

36. R. H. BROOKS and A. T. COREY, Properties of Porous Media Affecting Fluid Flow, J. Irrig. and Drainage Div. Proc. ASChE, 92, IR2, 61(1966).

37. A. W. REED, The Effect of Channeling on the Dryout of Heated Particulate Beds Immersed in a Liquid Pool, PhD Thesis, Massachusetts Institute of Technology, Cambridge (Feb. 1982).

38. V. X. TUNG and V. K. DHIR, Finite Element Solution of Multi–Dimensional Two–Phase Flow Through Porous Media with Arbitrary Heating conditions, Int. J. Multiphase Flow, Vol.16, No.6(1990)pp.985–1002.

39. G. A. SOD, A Survey of Several Finite Differential Methods for Systems of Nonlinear Hyperbolic Conservation Laws, J. of Comp. Physics 27, (1978) pp.1–31.

40. L. MEYER and M. KIRSTAHLER, Experimental Investigation of the Fluid Dynamic of a Gas Jet Expansion in a Liquid Pool, Proc. Ist World Conf. Experimental Heat Transfer, Fluid Mechanics, and Thermodynamics, Dubrovnik, Yugoslavia, September 4–9, 1988 pp. 864–871.

41. L. MEYER and M. KIRSTAHLER (unpublished) (1987).

42. D. WILHELM and M. KIRSTAHLER, Versuchsanlage zur schnellen Gasinjektion in einen wassergefühllten Behälter, KfK–4321, Kernforschungszentrum Karsruhe (1987).

43. W. MASCHEK, C. D. MUNZ and L. MEYER, An Assessment of Liquid Sloshing Phenomena in Pools Based on AFDM/SIMMER–II Code Calculations and Experiments, Proc. of the 1990 Int. Fast Reactor safety Meeting, Snowbird, Utah, Aug.12–16,1990pp.395–406.

44. C. W. HIRT and D. NICHOLS, Volume of Fluid (VOF) Method for the Dynamics of Free Boundaries, Journal of Computational Physics 38, 201–225 (1981).

45. N. I. KOLEV, IVA2 Verification Expansion Phase Experiment in SNR Geometry, KfK 4310, September 1987, in abbreviated form Experimental heat transfer, fluid mechanics and thermodynamics 1988, Proc. of the first world conf. held September 4–9, 1988, Dubrovnik, Yugoslavia. Editors R.K.Shah, E.N.Ganic, K.T.Yang, pp.827–881.

46. N. I. KOLEV, IVA2 Verification: High Pressure Gas Injection in a Liquid Pool, NUCLEAR TECHNOLOGY October 1988 Vol.83, Number 1, pp.65–80.

47. W. M. RHOSENOW and H. CHOI, Heat Mass, and Momentum Transfer, Prentice –

Hall, Inc., Engelwood Clifts, New Jersey 1961

48. A. K. ROSENZWEIG, V. P. TRONOV and L. P. PERGUSCHEV, Coaliszencija Kapel Vody v Melkodispersnych Emulsijach Tipa Voda v Nevti, Journal Pricladnoj Chimii, Nr.8(1980)pp.17776–1780.

49. M. v. SMOLUCHOWSKI, Z. Physik. Chem. (Leipzig) 92(1917)129.

50. W. I. HOWARTH, A.I.Ch.E. J. Vol.13, 5 (1967) 1007–1013.

51. C. A. COULALOGLU and L. L. TAVLARIDES, A. I. Ch. E. J. Vol. 22, 2 (1976) 289–297.

52. A. J. MADDEN, A. I. Ch. E. J. Vol. 8 (1962) 233.

53. S. KOMASAWA et al, J. of Chem. Engng. of Japan 2 (1969) 208.

54. K. SZTATECSNY, K. STÖBER and F. MOSER, Chem. Ing. Techn. MS 452/77.

55. S. S. KUTATELADZE, Similarity analyses in thermal physics (in Russian), Novosibirsk, Nauka, 1982

56. H. J. IVEY and D. J. MORRIS, On the Relevance of the Vapor – Liquid exchange Mechanism for Subcooled boiling Heat Transfer at High Pressure, AEEW–R127 (1962).

57. B. W. SPENCER, L. McUMBER, D. GREGORASH, R. AESCHLIMANN and J. J. SIENICKI, Corium Quench in Deep Pool Mixing Experiments, ANS Proc, 1985 Nat. Heat Transfer Conf, ANS 700101, Denver, CO, August 1985.

58. J. J. SIENICKI and B. W. SPENCER, Analysis of Reactor Material Experiments on Corium–Water Thermal Interactions in Ex–Vessel Geometry, Proc. Int. Meeting on Light Water Reactor Severe Accident Evaluation, August 28 to September 1, 1983, Cambridge, Massachusetts, Eds. J. R. Coombe, M. H. Fontana, G. J. Brown, C. A. Logue, ANS, (1983) pp. TS–12.1–1 TS–12–1.8.

59. B. W. SPENCER et al., Overview and Recent Results of ANL/EPRI Corium–Water Thermal Interaction Investigations, Proc. Int. Meeting on Light Water Reactor Severe Accident Evaluation, August 28 to September 1, 1983, Cambridge, Massachusetts, Eds. J. R. Coombe, M. H. Fontana, G. J. Brown, C. A. Logue, ANS, (1983) pp. TS–15.2–1 TS–15–2.6.

60. B. W. SPENCER, D. KILSDONK, and J. J. SIENICKI, Corium/Water Dispersal Phenomena in Ex–Vessel Cavity Interactions, Proc. Int. Meeting on Light Water Reactor Severe Accident Evaluation, August 28 to September 1, 1983, Cambridge, Massachusetts, Eds. J. R. Coombe, M. H. Fontana, G. J. Brown, C. A. Logue, ANS, (1983) pp. TS–15.5–1 TS–15.5–7.

61. B. W. SPENCER, L. McUMBER and J. J. SIENICKI, Simulant Studies of Debris Quenching in Ex–Vessel Geometry and Model Comparison, Proc. Int. Meeting on Light Water Reactor Severe Accident Evaluation, August 28 to September 1, 1983, Cambridge, Massachusetts, Eds. J. R. Coombe, M. H. Fontana, G. J. Brown, C. A. Logue, ANS, (1983) pp. TS–6.2–1 TS–6–2.9.

62. M. A. ABOLFADL and T. G. THEOFANOUS, An Assessment of Steam– Explosion–

Induced Containment Failure. Part II: Premixing Limits, NSE 97 (1987) 282–295.

63. W. H. AMARASOORIYA and T. G. THEOFANOUS, Premixing of Steam Explosions: A Three– Field Model, Proc. 1988 Nat. Heat Transfer Conf. Houston, TX, July 24–24 (1988) pp.191–200.

64. A. THYAGARAJA and D. F. FLETCHER, Buoyancy–Driven, Transient, Two–Dimensional Thermo– Hydrodynamics of a Melt– Water– Steam Mixture, Computers & Fluids Vol.16, No.1 (1988) pp. 59–80.

65. M. STEPHAN and F. MAYINGER, Countercurrent Flow Limitation in Vertical Ducts at High System Pressure, Ed. G. Hetsroni, Proc. of The Ninth International Heat Transfer Conference, Jerusalem, Israel, Vol.6 (August 19–24, 1990) pp.47–52.

66. A. ACRIVOS and T. D. TAYLOR, Heat and mass transfer from single spheres in stokes flow, The Physics of Fluids, Vol.5, No.4 (1962) pp.387–394

## FIGURES

FIGURE 1. Postulated flow regimes in IVA3

FIGURE 2. The calculated mean superficial gas ($j_1$), liquid ($j_2$), and solid particle ($j_3$) velocity with the IVA3 constitutive models versus the measured ones for: $D_3$=1.13÷4.16mm, $D_h$=2.09÷5.05cm, $\rho_3$=2270, 2380, 2400kg/m$^3$, $\alpha_1$ = 0.0108÷0.1341, $\alpha_3$ = 0.00482÷0.0726, $j_1$=0.0079÷0.1201m/s, $j_2$=0.3918÷1.0257m/s, $j_3$=0.0023÷0.0446m/s.

FIGURE 3. Pressure as a function of space 250 $\mu s$ after the beginning of the process.

FIGURE 4. Velocity as a function of space 250 $\mu s$ after the beginning of the process.

FIGURE 5. Specific entropy as a function of space 250 $\mu s$ after the beginning of the process.

FIGURE 6. Temperature as a function of space 250 $\mu s$ after the beginning of the process.

FIGURE 7. Density as a function of space 250 $\mu s$ after the beginning of the process.

FIGURE 8. Sonic velocity as a function of space 250 $\mu s$ after the beginning of the process.

FIGURE 9 a. Geometry of the test section of the Meyer – Kirstahler gas injection experiments: gas jet in gas with internals.

FIGURE 9 b. Geometry of the test section of the Meyer – Kirstahler gas injection experiments: gas jet in liquid with internals.

FIGURE 9 c. Geometry of the test section of the Meyer – Kirstahler gas injection experiments: gas jet in liquid without internals.

FIGURE 10. Pressure as a function of time. Comparison of the IVA3 prediction (26x44 discretization cells) of the total pressure in the center of the computational cell (I=5, K=45) with the measured total pressure on the vessel cover at (r=0.022, z=0.693). Meyer–Kirstahler experiment: gas injection in gas with internals. 0.6 MPa pressure source.

FIGURE 11. Pressure as a function of time. Comparison of the IVA3 prediction (26x44 discretization cells) of the static pressure in the center of the computational cell (I=19, K=2) with the measured total pressure at (r=0.1143, z=0.2). Meyer–Kirstahler experiment: gas injection in gas with internals. 0.6 MPa pressure source.

FIGURE 12. Pressure as a function of time. Comparison of the IVA3 prediction (26x44 discretization cells) of the total pressure in the center of the computational cell (I=25, K=45) with the measured total pressure on the vessel cover at (r=0.149, z=0.693). Meyer–Kirstahler experiment: gas injection in gas with internals. 0.6 MPa pressure source.

FIGURE 13. Pressure as a function of time. Comparison of the IVA3 prediction (26x44

discretization cells) of the total pressure in the center of the computational cell (I=5, K=45) with the measured total pressure on the vessel cover at (r=0.022, z=0.693). Meyer–Kirstahler experiment: gas injection in liquid with internals. 0.6 MPa pressure source.

FIGURE 14. Pressure as a function of time. Comparison of the IVA3 prediction (26x44 discretization cells) of the total pressure in the center of the computational cell (I=11, K=45) with the measured total pressure on the vessel cover at (r=0.07, z=0.693 m. Meyer–Kirstahler experiment: gas injection in liquid with internals. 0.6 MPa pressure source.

FIGURE 15. Pressure as a function of time. Comparison of the IVA3 prediction (26x44 discretization cells) of the total pressure in the center of the computational cell (I=25, K=45) and (I=19, K=2) with the measured total pressure on the vessel cover corner at (r=0.149, z=0.693) and at (r=0.1143, z=0.2), respectively. Meyer–Kirstahler experiment: gas injection in liquid with internals. 0.6 MPa pressure source.

FIGURE 16. Pressure as a function of time. Comparison of the IVA3 prediction (26x44 discretization cells) of the static pressure in the center of the computational cell (I=7, K=5) with the measured pressure on the wall of the gas entrance nozzle. Meyer–Kirstahler experiment: gas injection in liquid with internals. 0.6 MPa pressure source.

FIGURE 17 a,b,c. Gas volume fraction as a function of radius and height. Parameter – time. Gas jet expansion in a liquid with internals. Pressure source 0.6 MPa. $\tau$ =0.0029, 0.0039 and 0.0049 s.

FIGURE 18 a,b,c. Gas volume fraction as a function of radius and height. Parameter – time. Gas jet expansion in a liquid with internals. Pressure source 1.1 MPa. $\tau$ = 0.0029, 0.0039 and 0.0049 s.

FIGURE 19. Geometry of the test section of the Meyer – Kirstahler gas injection experiments. Gas injection in liquid with internals – strong liquid acceleration. Pressure source 1.1 MPa.

FIGURE 20 a,b,c,d,e. Gas volume fraction as a function of radius and height. Parameter – time. Gas injection in liquid with internals – strong liquid acceleration. Pressure source 1.1 MPa.

FIGURE 21. Pressure as a function of time. Comparison of the IVA3 prediction (26x44 discretization cells) of the total pressure in the center of the computational cell (I=5, K=45) with the measured total pressure on the vessel cover at (r=0.022, z=0.693). Meyer–Kirstahler experiment: gas injection in liquid without internals. 0.6 MPa pressure source. AL0=0.001

FIGURE 22. Pressure as a function of time. Comparison of the IVA3 prediction (26x44 discretization cells) of the total pressure in the center of the computational cell (I=11, K=45) with the measured total pressure on the vessel cover at (r=0.07, z=0.693 m. Meyer–Kirstahler experiment: gas injection in liquid without internals. 0.6 MPa pressure source. AL0=0.001

FIGURE 23. Pressure as a function of time. Comparison of the IVA3 prediction (26x44 discretization cells) of the total pressure in the center of the computational cell (I=25, K=45) and (I=19, K=2) with the measured total pressure on the vessel cover corner at (r=0.149, z=0.693) and at (r=0.1143, z=0.2), respectively. Meyer–Kirstahler experiment:

gas injection in liquid without internals. 0.6 MPa pressure source. AL0=0.001

FIGURE 24 a. Pressure as a function of time. Comparison of the IVA3 prediction (26x44 discretization cells) of the static pressure in the center of the computational cell (I=7, K=5) with the measured pressure on the wall of the gas entrance nozzle. Meyer–Kirstahler experiment: gas injection in liquid without internals. 0.6 MPa pressure source. AL0=0.001

FIGURE 24 b. Pressure as a function of time. Comparison of the IVA3 prediction (26x44 discretization cells) of the static pressure in the center of the computational cell (I=7, K=5) with the measured pressure on the wall of the gas entrance nozzle. Meyer–Kirstahler experiment: gas injection in liquid without internals. 0.6 MPa pressure source. AL0=0.001

FIGURE 25. Pressure as a function of time. Comparison of the IVA3 prediction (26x44 discretization cells) of the total pressure in the center of the computational cell (I=5, K=45) with the measured total pressure on the vessel cover center at (r=0.022, z=0.693). Parameter in IVA3 simulation: volume fraction of the initially dissolved gasses (0.001 and 0.004). Meyer–Kirstahler experiment: gas injection in liquid without internals. 0.6 MPa pressure source.

FIGURE 26. Pressure as a function of time. Comparison of the IVA3 prediction (26x44 discretization cells) of the total pressure in the center of the computational cell (I=5, K=45) with the measured total pressure on the vessel cover center at (r=0.022, z=0.693). Parameter by the IVA3 simulation: opening time of the sliding doors (0 and 0.4 ms). Meyer–Kirstahler experiment: gas injection in liquid without internals. 6 bar pressure source.

FIGURE 27. Volumetric concentration of water as a function of the radial and axial coordinates at different times from the beginning of the process. $\tau$ = 0.00, 0.08, 0.16, 0.20, 0.40, 0.56, 0.64, 0.72, 0.91 s.

FIGURE 28. Fuel, water, and steam volumetric fraction as functions of space. Parameter: time.

FIGURE 29. Predictions of particle and water volumetric fraction distributions at 0.5 and 1 s. Comparison of IVA3 prediction with that obtained by Amarasooriya and Theofanous with the PM–ALPHA code.

FIGURE 30. Fuel Mass Transients: Comparison of the IVA3 prediction with the prediction by Amarasooriya and Theofanous.

FIGURE 31. Mixing criteria. a) Abolfadl et al. criterion fulfilled for cells predominantly occupied by fuel. b) Abolfadl et al. criterion not fulfilled for cells occupied approximately uniformly by fuel, steam, an liquid. c–f) Explanation to the estimation of the fuel mass surrounded by liquid.

FIGURE 32. Bottom pressure transients: Comparison of the IVA3 prediction with the Amarasooriya and Theofanous prediction.

FIGURE 33. Wall pressure transients: Comparison of the IVA3 prediction with the Amarasooriya and Theofanous prediction.

FIGURE 34. Top pressure transients: Comparison of the IVA3 prediction with the Amarasooriya and Theofanous prediction.

FIGURE 35. Geometry of typical PWR–1300 type reactor. Cell noding diagram for IVA3.

FIGURE 36. Fuel, water, and steam volumetric fractions as functions of space. Parameter: time. IVA3 prediction for a PWR–1300 type reactor.

FIGURE 37. Pressure transients in lower plenum due to premixing. IVA3 Prediction for typical PWR 1300 reactor.

FIGURE 38. IVA3 prediction of fuel mass transients in typical PWR 1300 reactor.

FIGURE 39. Melt mass surrounded by liquid as a function of time. Particle diameter 0.01 m, discharge circle with diameter of 1.8 m and axial permeability of 0.5, $\rho_3=\rho_{UO_2}$, no flow distribution plate.

FIGURE 40. Melt mass surrounded by liquid as a function of time. Case C: particle diameter 0.02 m, discharge circle with diameter of 1.8 m and axial permeability of 0.5, $\rho_3=\rho_{UO_2}$, no flow distribution plate.

FIGURE 41. Comparison of the melt masses surrounded by liquid for two different cases: case B with particle size of 0.01 m and case C with particle size of 0.02 m.

FIGURE 42. Melt mass surrounded by liquid as a function of time. Case D: particle diameter 0.01 m, discharge circle with diameter 1.2 m and axial permeability of 0.5, $\rho_3=\rho_{UO_2}$, no flow distribution plate.

FIGURE 43. Comparison of the melt masses surrounded by liquid for two different cases: case B with discharge circle with diameter of 1.8 m and axial permeability of 0.5 and case D with discharge circle with diameter of 1.2 m.

FIGURE 44. Basic elements of the experimental apparatus.

FIGURE 45. Injected corium mass flow in the ANL CWTI9 experiment.

FIGURE 46. Total corium mass conservation predicted by IVA3 for the CWTI9 experiment.

FIGURE 47. Corium mass distribution as a function of time for the CWTI9 experiment as predicted by IVA3 3D simulation.

FIGURE 48. Limits of the corium–water intermixing as a function of time. IVA3 3D prediction of the ANL CWTI9 experiment.

FIGURE 49. Water mass distribution versus time. IVA3 3D prediction of the ANL CWTI9 experiment.

FIGURE 50. Volumetric fractions of the three components in the IV for different times in the first angular sector containing the escape pipeway.

FIGURE 51. Pressures versus time at different levels (bottom, middle and top) in the immediate neighborhood to the vertical wall of the interaction vessel.

FIGURE 52. Pressure in the expansion vessel versus time.

FIGURE 53. Geometry of typical 1300 MWe PWR type reactor, cell noding diagram for IVA3 simulation, initial conditions.

FIGURE 54. Corium, water, and steam volume fractions as functions of space. Parameter: time.

FIGURE 55. Pressure acting at different positions of the reactor vessel wall due to melt – water interaction versus time.

(a) lower plenum (I= 2, K= 2)
(b) lower plenum (I= 7, K= 3)
(c) lower plenum (I=10, K= 5)
(d) lower plenum (I=12, K= 7)
(e) down comer (I=12, K=24)
(f) upper plenum (I=12, K=27)
(g) upper plenum (I= 9, K=27)
(h) upper plenum (I= 2, K=27)

FIGURE 56. Melt and water masses as functions of time. 1300 MWe PWR melt–water interaction. 54 t initial melt mass in the core, 15.6 t initial water mass in the lower plenum.

FIGURE 57. Geometry of typical 1300 MWe PWR type reactor, cell noding diagram for IVA3 simulation, initial conditions. Molten lower end of the fuel elements and flow distribution plate.

FIGURE 58. Corium, water, and steam volume fractions as functions of space. Parameter: time. Molten lower end of the fuel elements and flow distribution plate.

FIGURE 59. Pressure acting at different positions of the reactor vessel wall due to melt – water interaction versus time. Molten lower end of the fuel elements and flow distribution plate.

(a) lower plenum (I= 2, K= 2)
(b) lower plenum (I= 7, K= 3)
(c) lower plenum (I=10, K= 5)
(d) lower plenum (I=12, K= 7)
(e) down comer (I=12, K=24)
(f) upper plenum (I=12, K=27)
(g) upper plenum (I= 9, K=27)
(h) upper plenum (I= 2, K=27)

FIGURE 60. Melt and water masses as functions of time. 1300 MWe PWR melt–water interaction. 54 t initial melt mass in the core, 15.6 t initial water mass in the lower plenum. Molten lower end of the fuel elements and flow distribution plate.

FIGURE 61. IVA3 predictions of pressure transients during melt water interaction for three different hypotheses regarding the fuel state and the structure below the core.

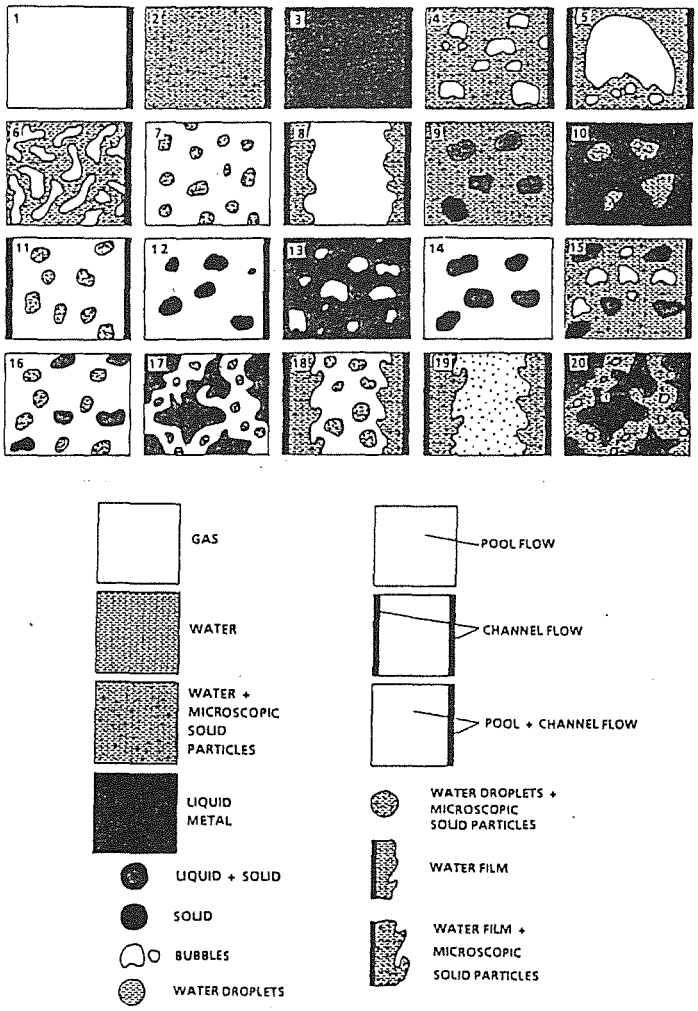


FIGURE 1. Postulated flow regimes in IVA3

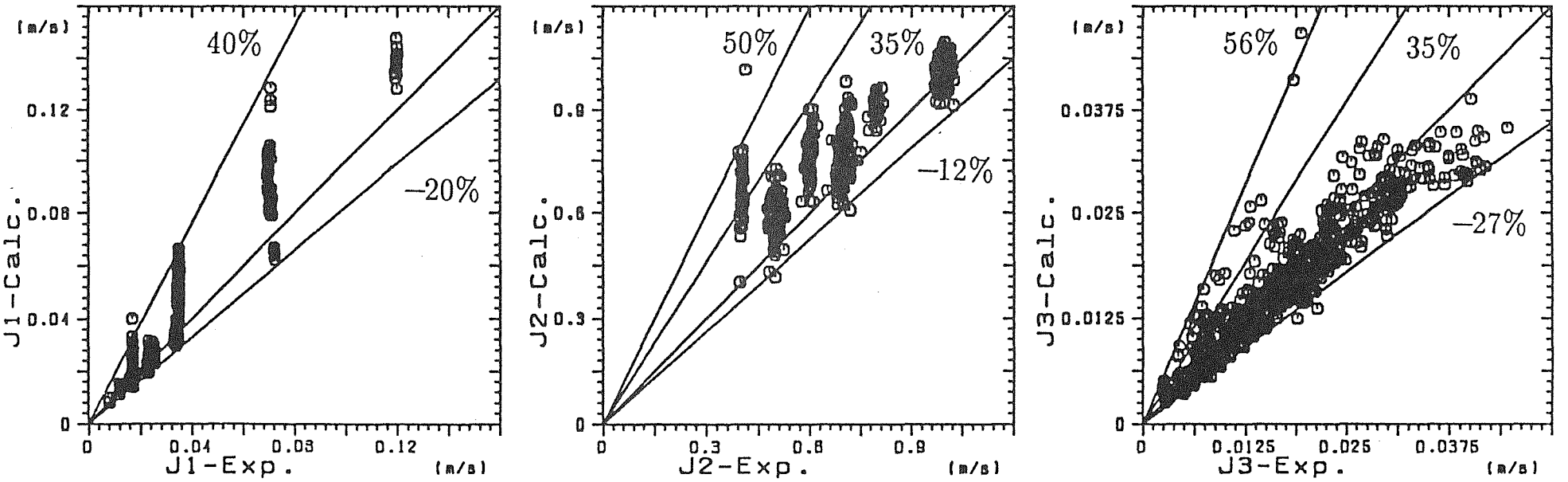


FIGURE 2. The calculated mean superficial gas ($j_1$), liquid ($j_2$), and solid particle ($j_3$) velocity with the IVA3 constitutive models versus the measured ones for: $D_3$=1.13÷4.16mm, $D_h$=2.09÷5.05cm, $\rho_3$=2270, 2380, 2400kg/m$^3$, $\alpha_1$ = 0.0108÷0.1341, $\alpha_3$ = 0.00482÷0.0726, $j_1$=0.0079÷0.1201m/s, $j_2$=0.3918÷1.0257m/s, $j_3$=0.0023÷0.0446m/s.

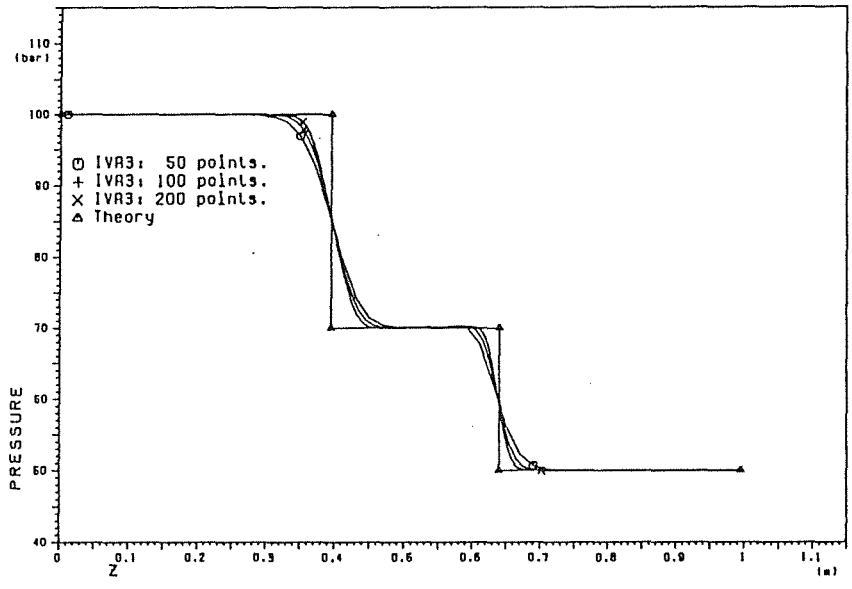


FIGURE 3. Pressure as a function of space 250 $\mu$s after the beginning of the process.

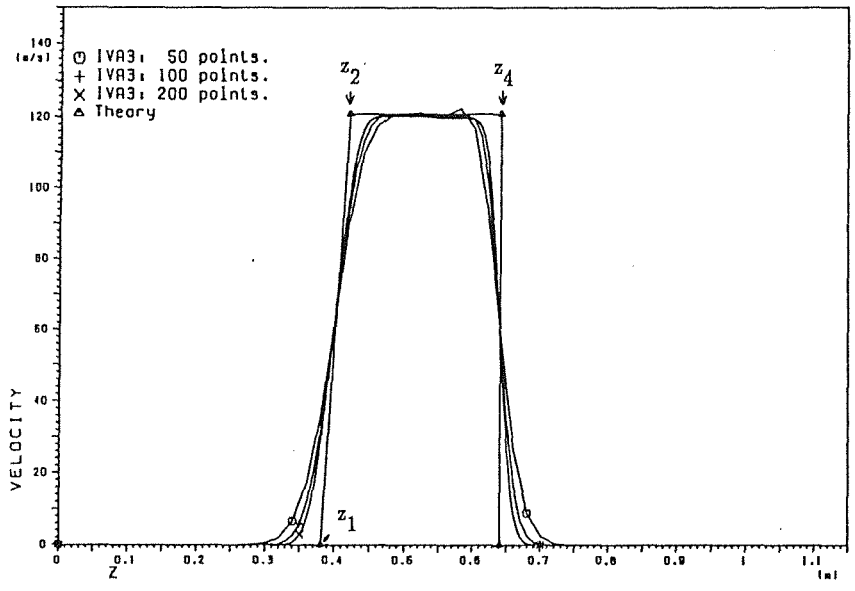


FIGURE 4. Velocity as a function of space 250 $\mu$s after the beginning of the process.

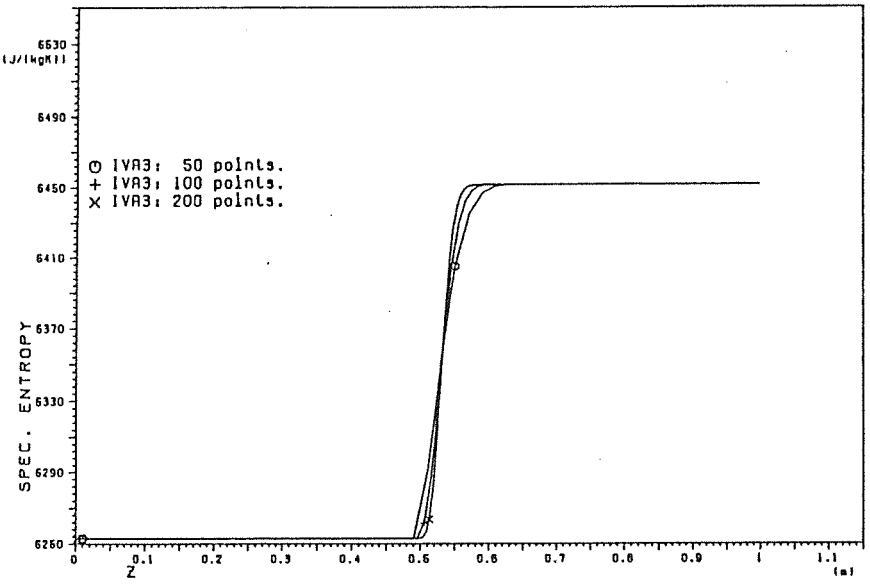


FIGURE 5. Specific entropy as a function of space 250 $\mu$s after the beginning of the process.

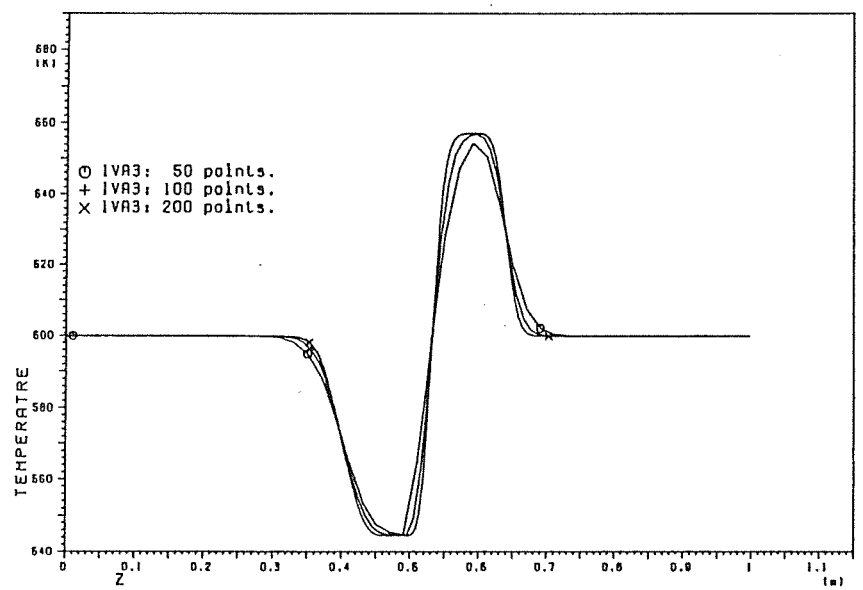


FIGURE 6. Temperature a function of space 250 $\mu$s after the beginning of the process.

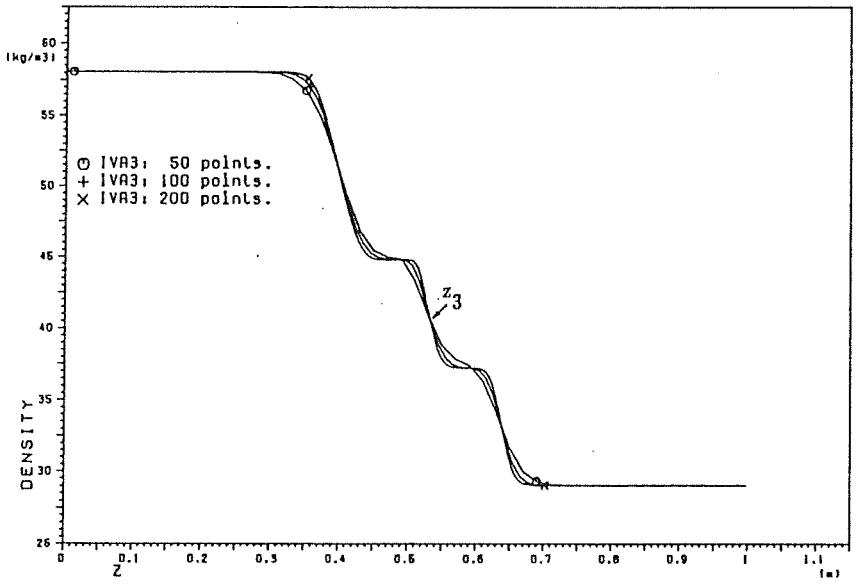


FIGURE 7. Density as a function of space 250 $\mu s$ after the beginning of the process.

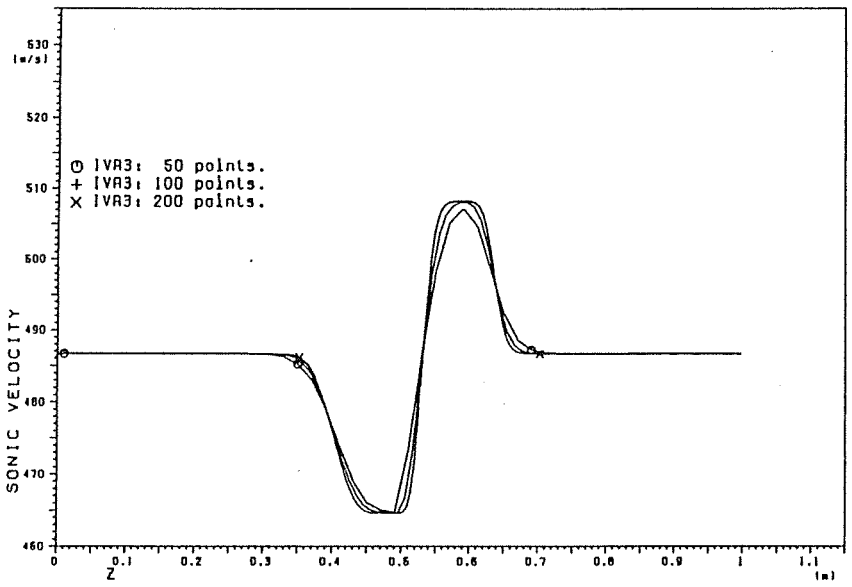


FIGURE 8. Sonic velocity as a function of space 250 $\mu s$ after the beginning of the process.

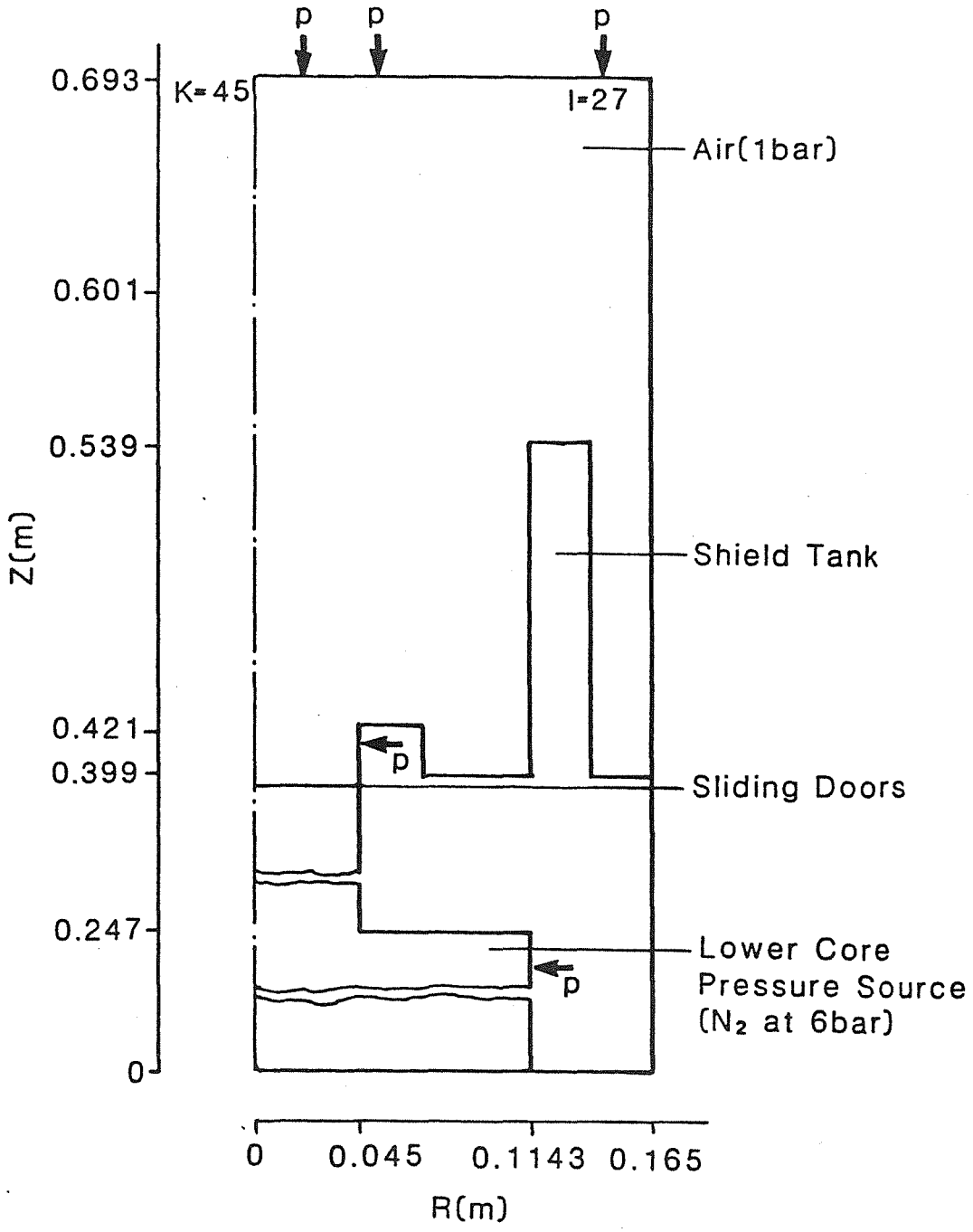


FIGURE 9 a. Geometry of the test section of the Meyer – Kirstahler gas injection experiments: gas jet in gas with internals.

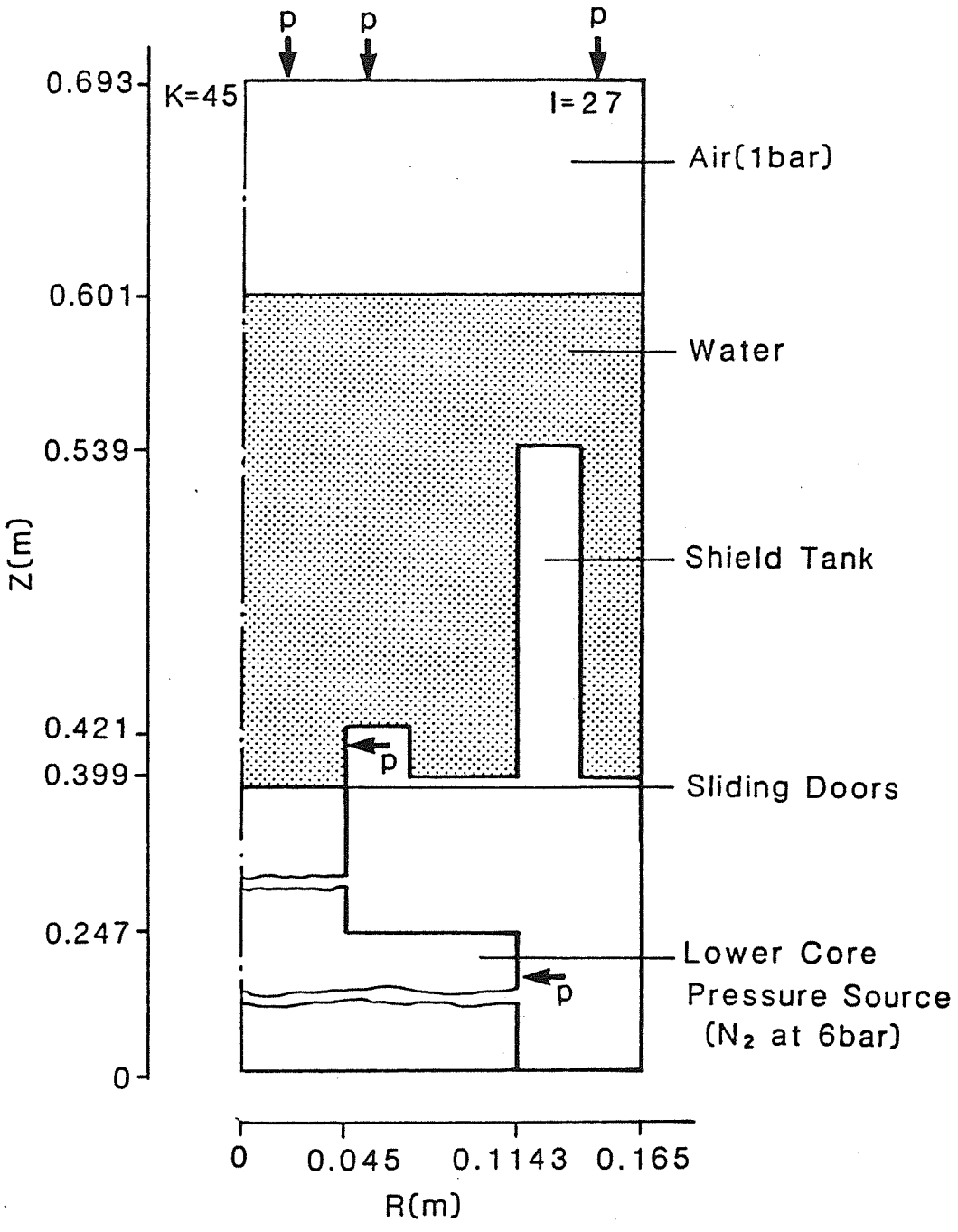


FIGURE 9 b. Geometry of the test section of the Meyer – Kirstahler gas injection experiments: gas jet in liquid with internals.

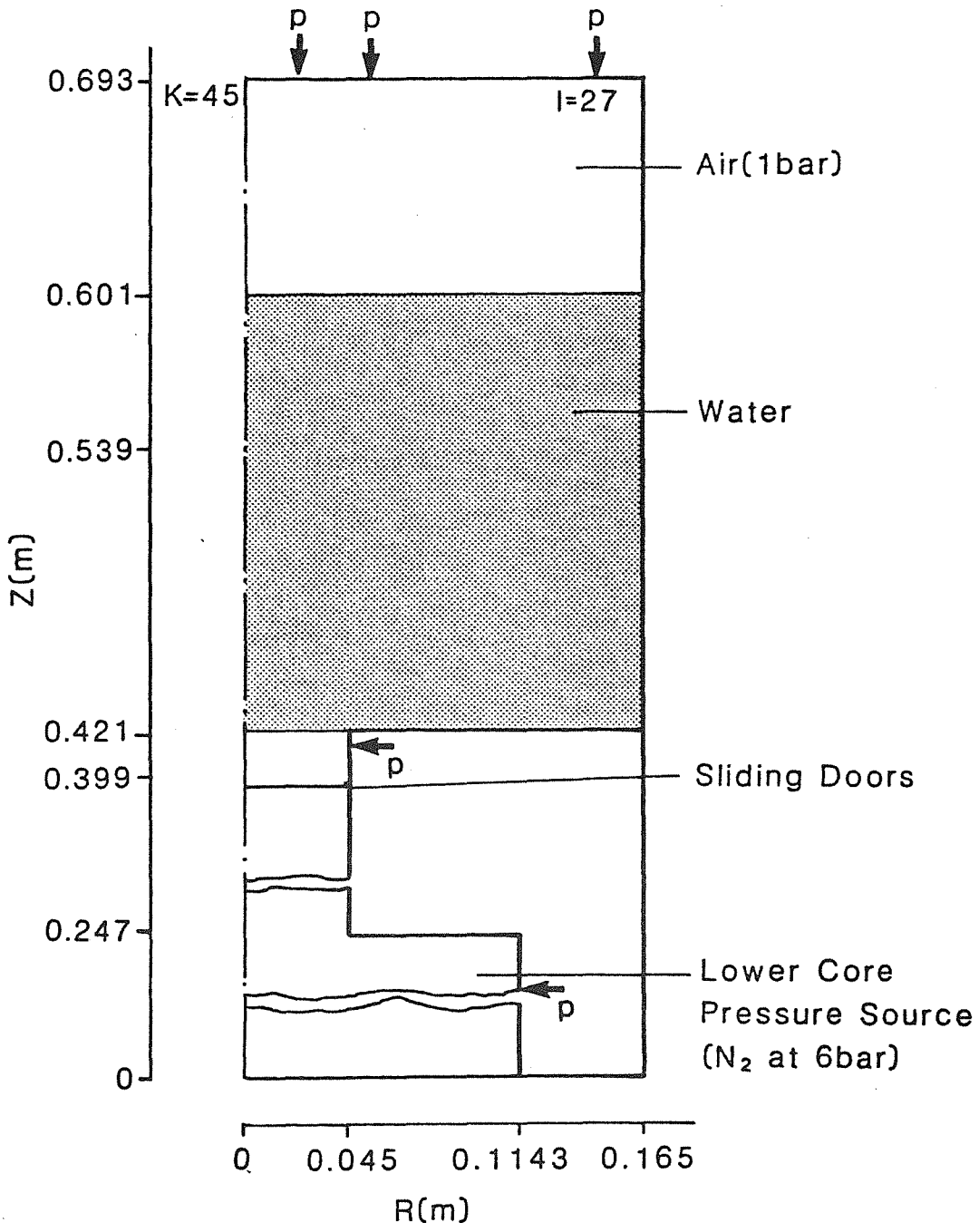


FIGURE 9 c. Geometry of the test section of the Meyer – Kirstahler gas injection experiments: gas jet in liquid without internals.

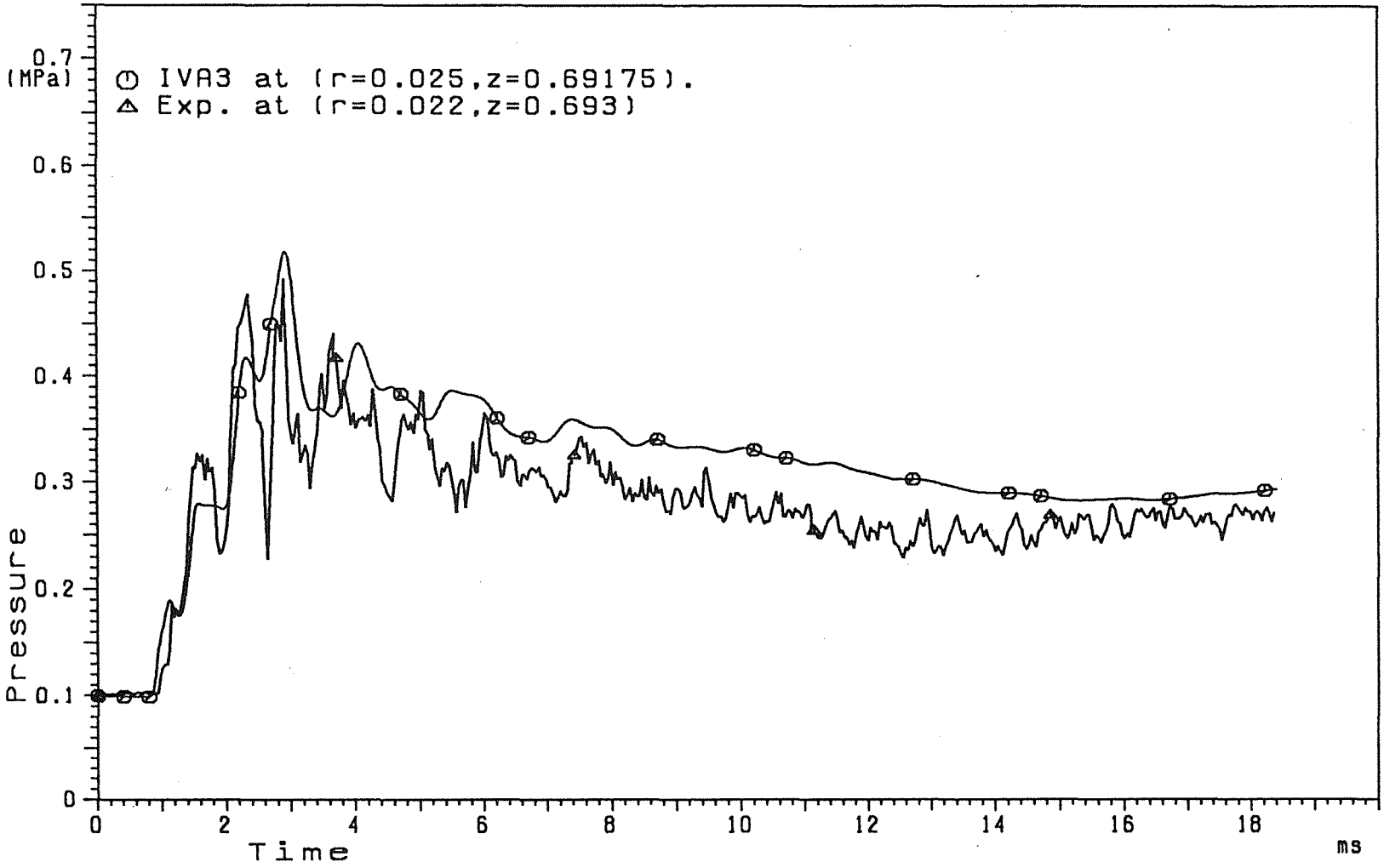


FIGURE 10. Pressure as a function of time. Comparison of the IVA3 prediction (26x44 discretization cells) of the total pressure in the center of the computational cell (I=5, K=45) with the measured total pressure on the vessel cover at (r=0.022, z=0.693). Meyer–Kirstahler experiment: gas injection in gas with internals. 0.6 MPa pressure source.

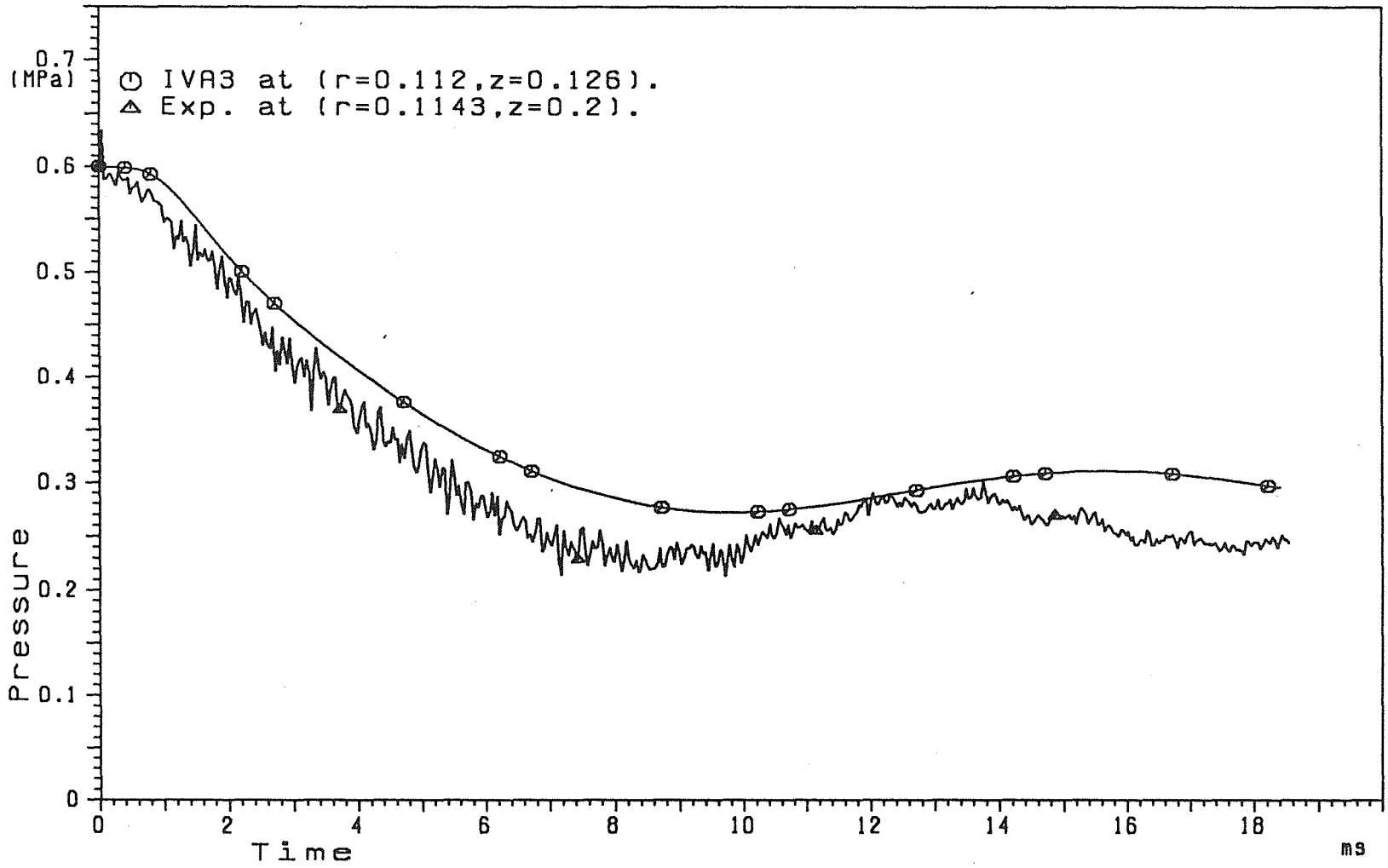


FIGURE 11. Pressure as a function of time. Comparison of the IVA3 prediction (26x44 discretization cells) of the static pressure in the center of the computational cell (I=19, K=2) with the measured total pressure at (r=0.1143, z=0.2). Meyer–Kirstahler experiment: gas injection in gas with internals. 0.6 MPa pressure source.

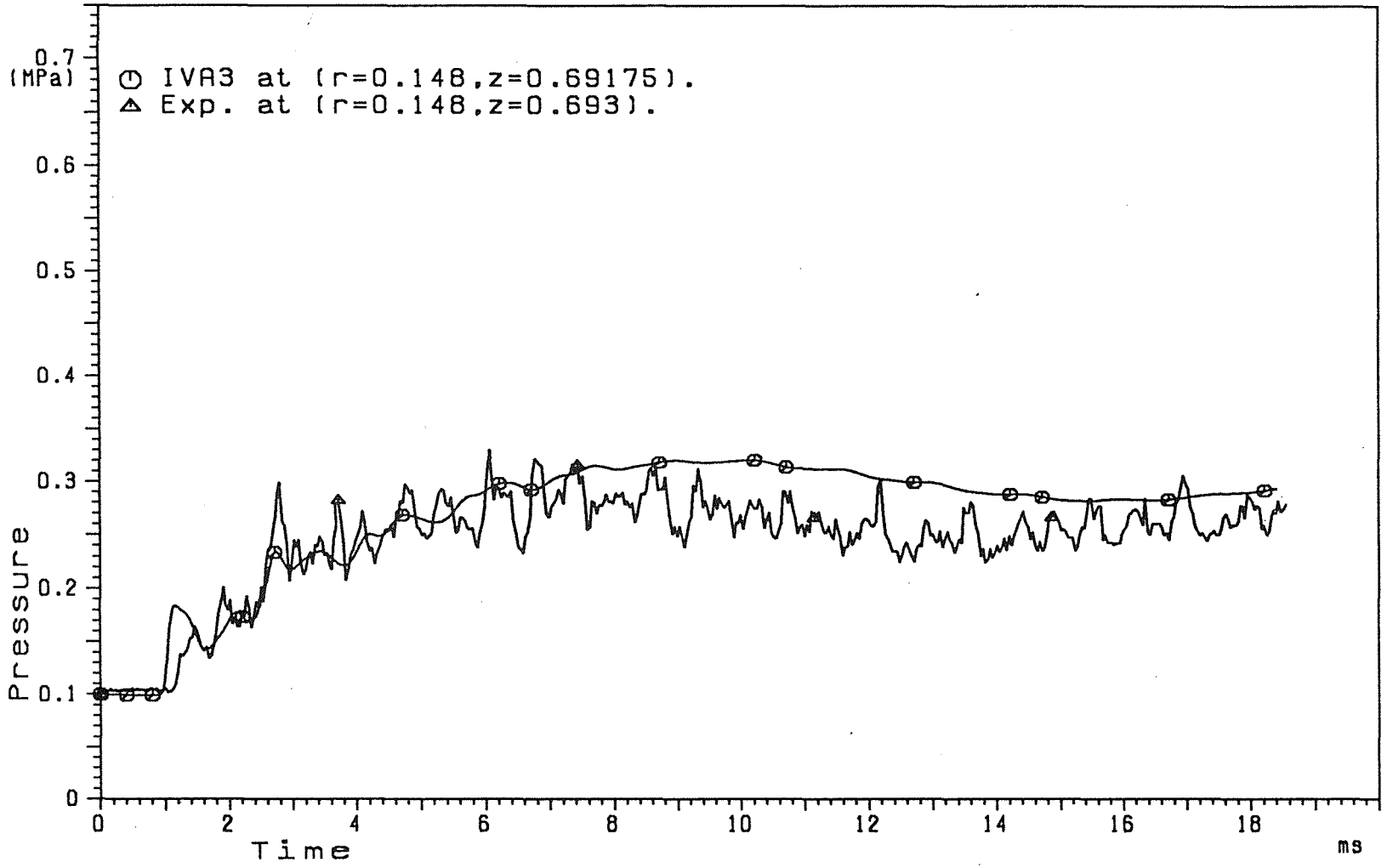


FIGURE 12. Pressure as a function of time. Comparison of the IVA3 prediction (26x44 discretization cells) of the total pressure in the center of the computational cell (I=25, K=45) with the measured total pressure on the vessel cover at (r=0.149, z=0.693). Meyer–Kirstahler experiment: gas injection in gas with internals. 0.6 MPa pressure source.

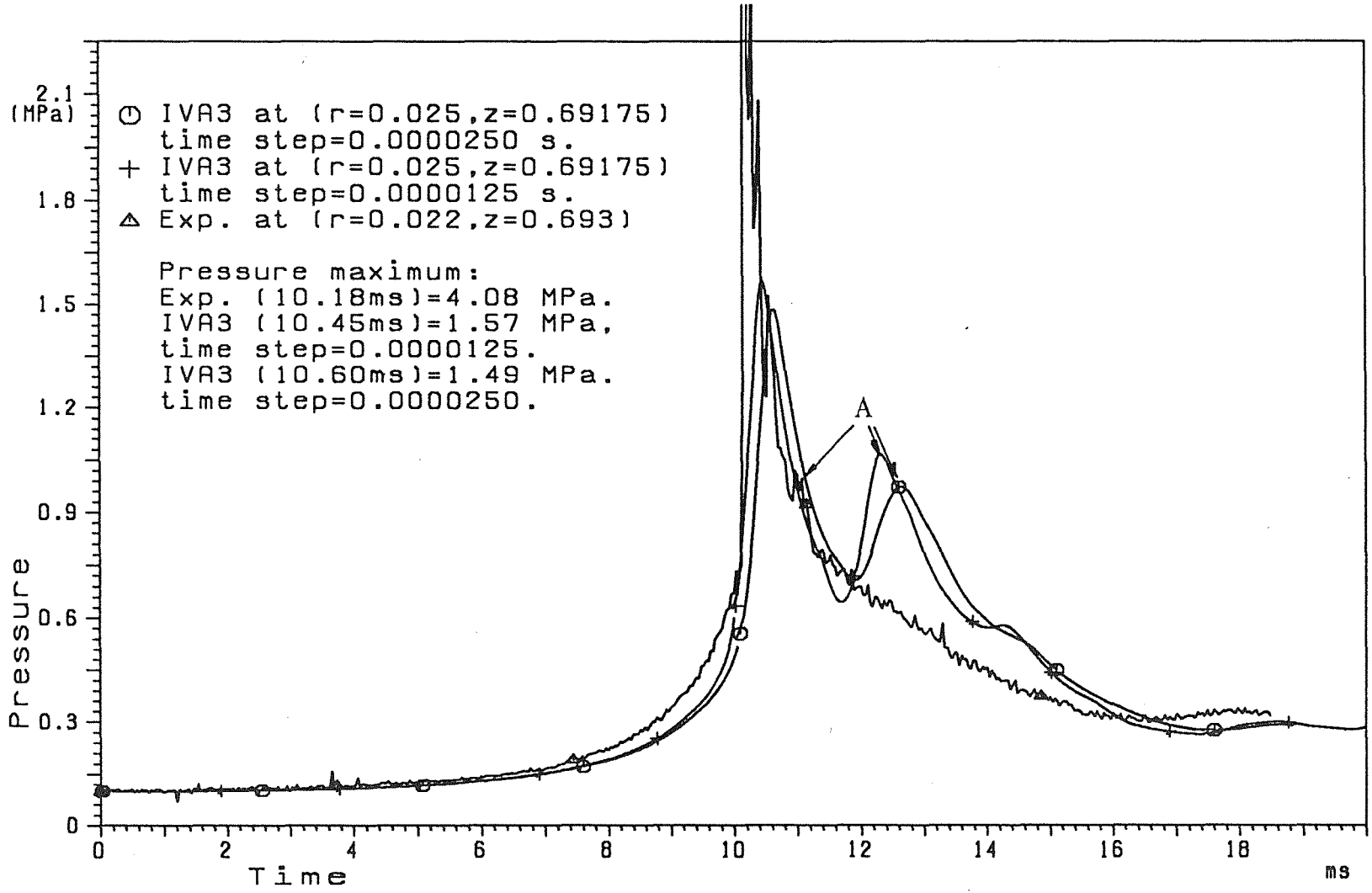


Fig. 13. Pressure as a function of time. Comparison of the IVA3 prediction (26x44 discretization cells) of the total pressure in the center of the computational cell (I=5,K=45) with the measured pressure on the vessel cover at (r=0.022, z=0.693). Meyer-Kirstahler experiment: gas injection in liquid with internals. 6 bar pressure source.

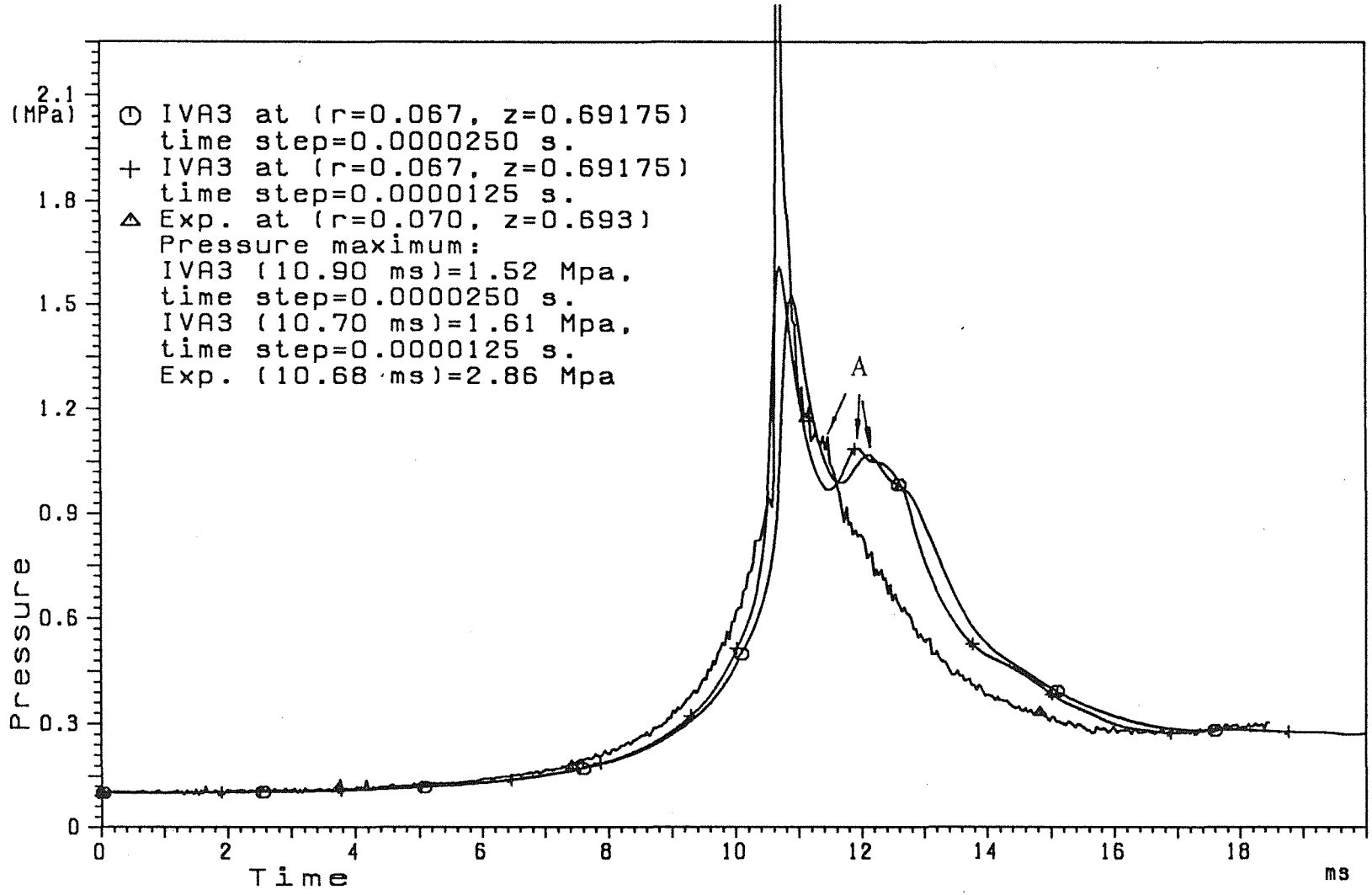


Fig. 14. Pressure as a function of time. Comparison of the IVA3 prediction (26x44 discretization cells) of the total pressure in the center of the computational cell (I=11,K=45) with the measured pressure on the vessel cover at (r=0.07, z=0.693). Meyer-Kirstahler experiment: gas injection in liquid with internals. 6 bar pressure source.

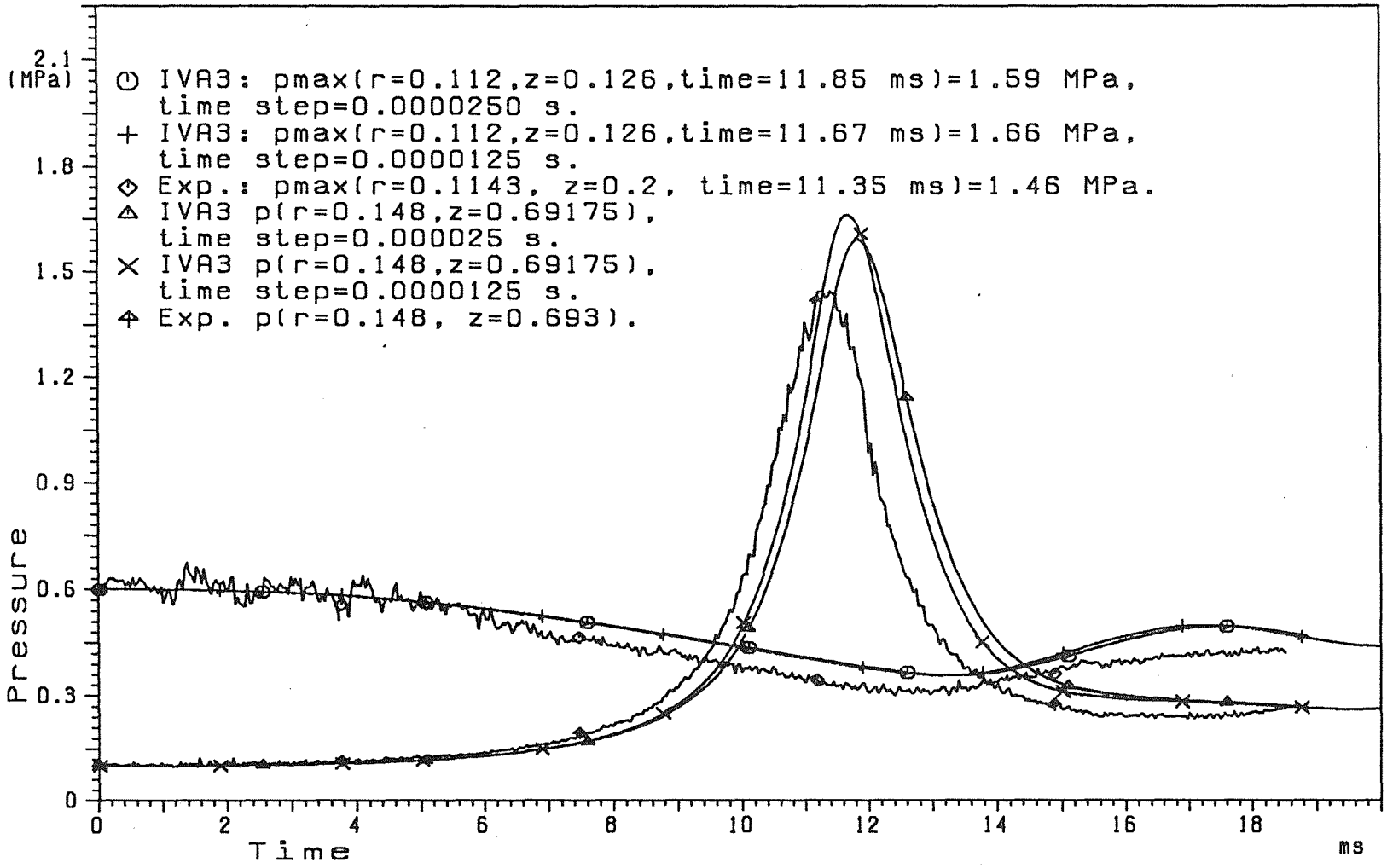


Fig. 15. Pressure as a function of time. Comparison of the IVA3 prediction (26x44 discretization cells) of the total pressure in the center of the computational cell (I=25,K=45) and (I=19,K=2) with the measured total pressure on the vessel cover at (r=0.149, z=0.693) and at (r=0.1143, z=0.2), respectively. Meyer-Kirstahler experiment: gas injection in liquid with internals. 6 bar pressure source.

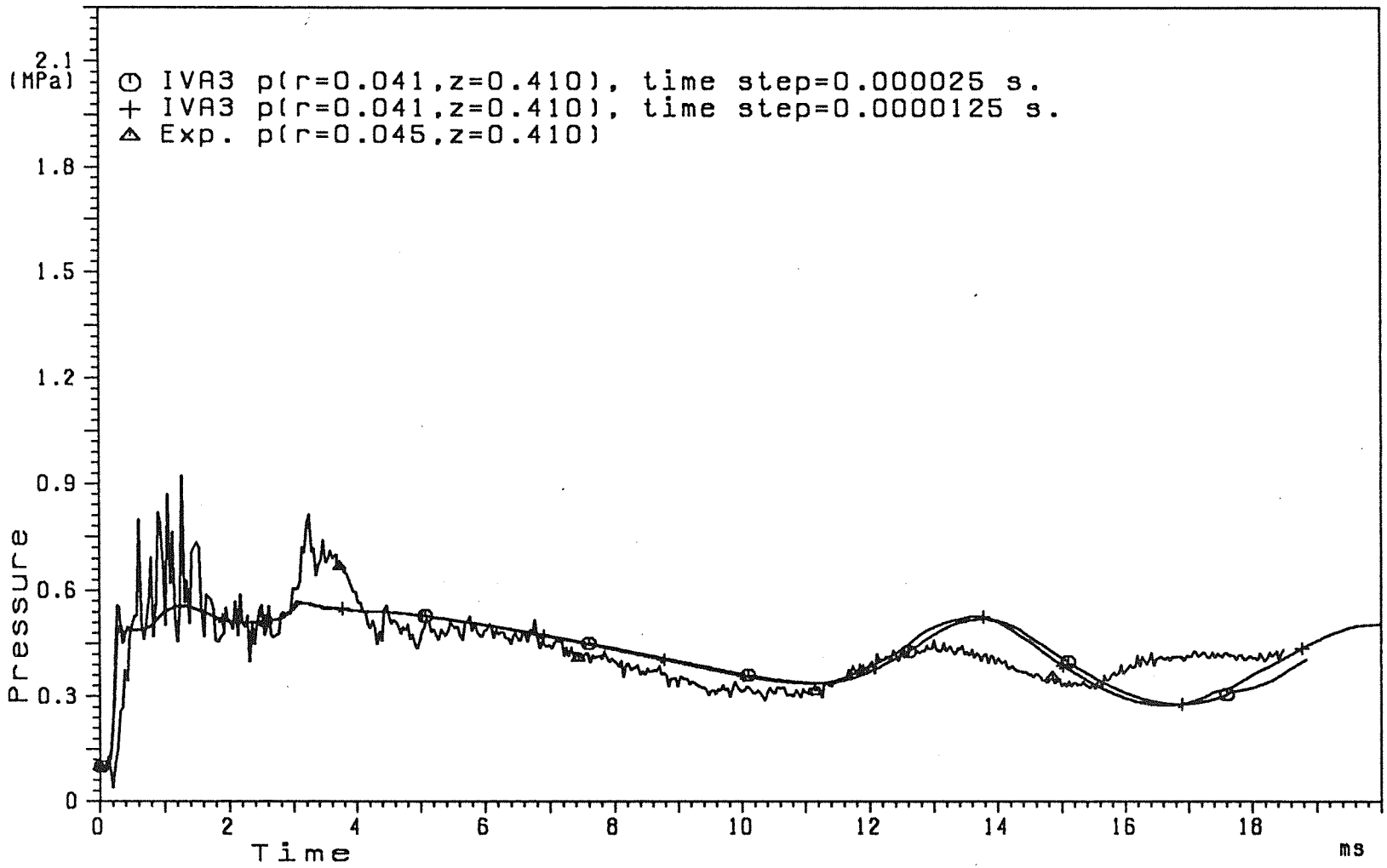


Fig. 16. Pressure as a function of time. Comparison of the IVA3 prediction (26x44 discretization cells) of the static pressure in the center of the computational cell (I=7,K=5) with the measured pressure on the wall of the gas entrance nozzle. Meyer-Kirstahler experiment: gas injection in liquid with internals. 6 bar pressure source.

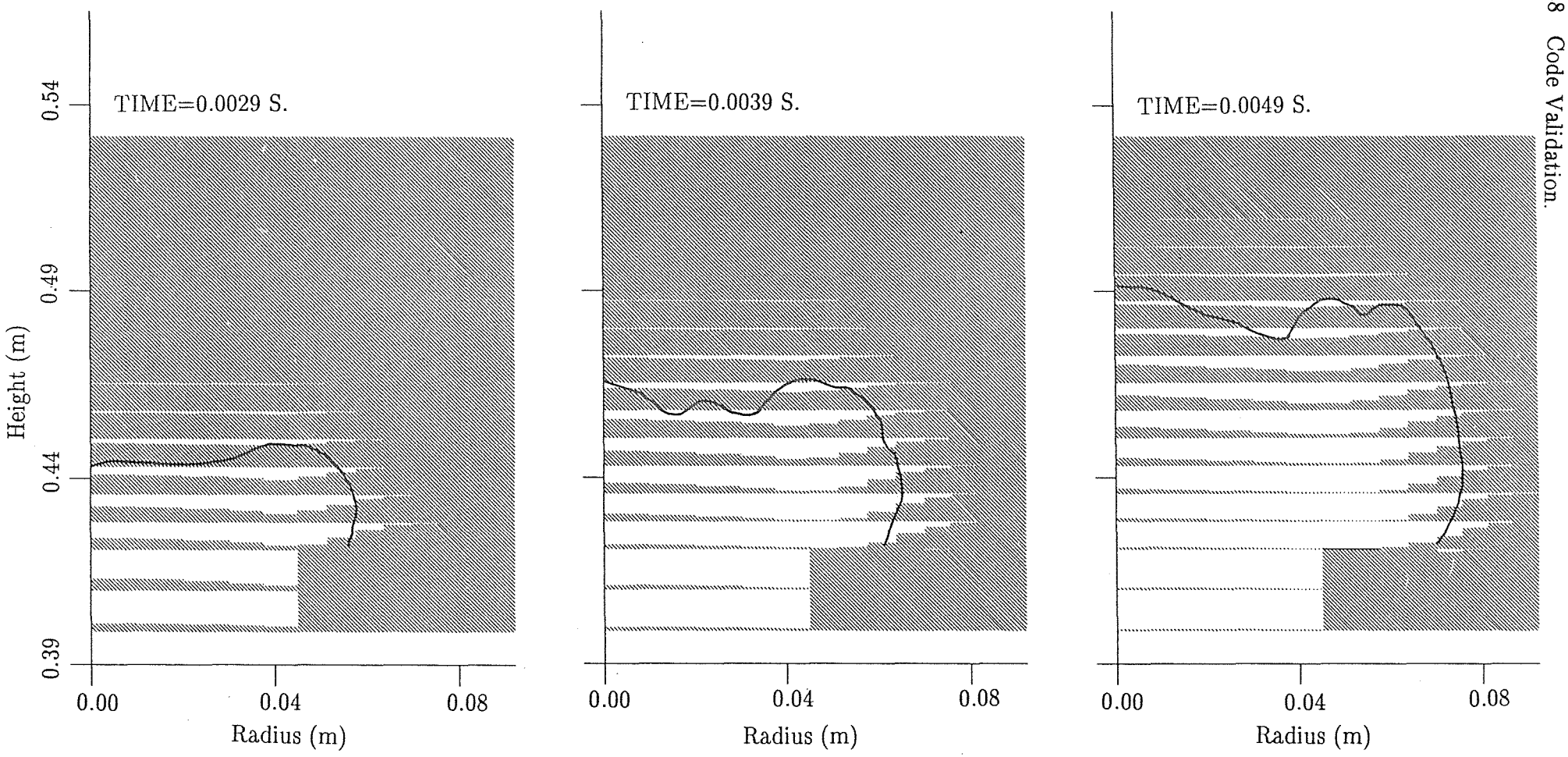


FIGURE 17 a,b,c. Gas volume fraction as a function of radius and height. Parameter — time. Gas jet expansion in a liquid with internals. Pressure source 0.6 MPa.

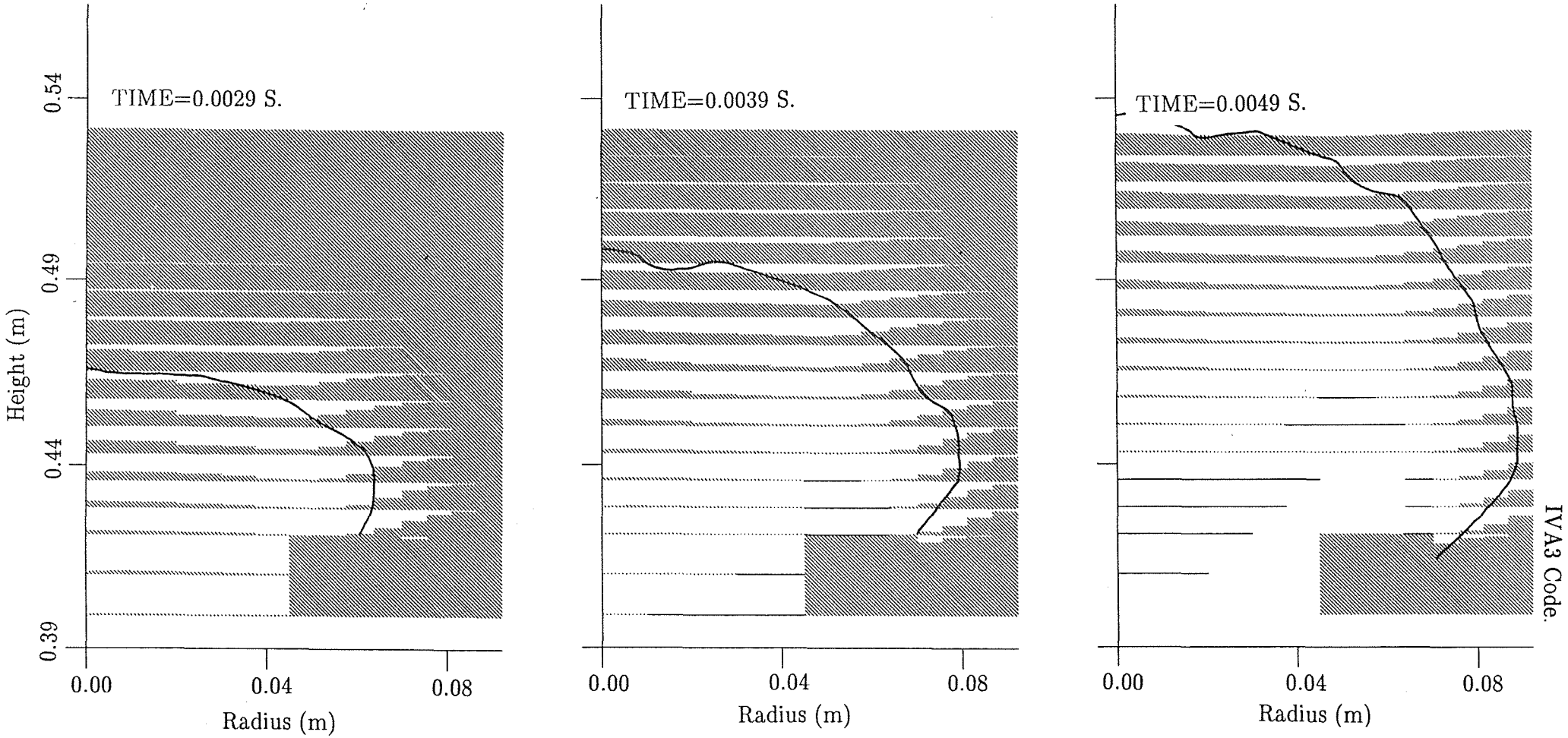


FIGURE 18 a,b,c. Gas volume fraction as a function of radius and height. Parameter – time. Gas jet expansion in a liquid with internals. Pressure source 1.1 MPa.

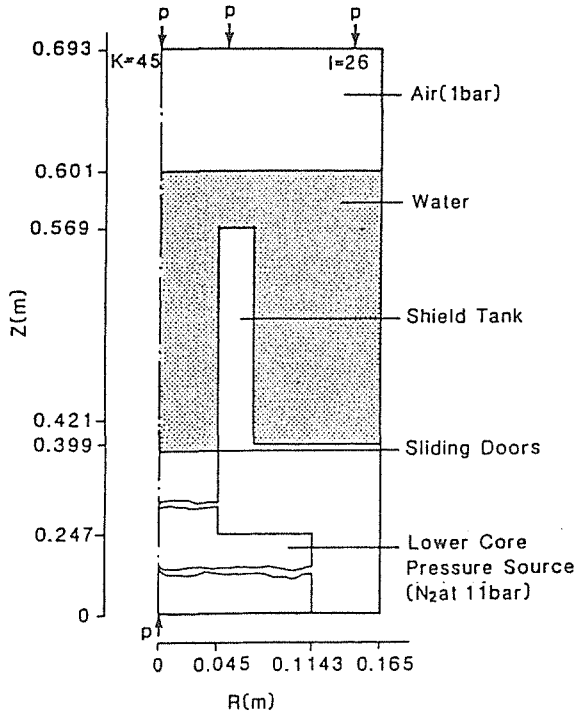


FIGURE 19. Geometry of the test section of the Meyer – Kirstahler gas injection experiments. Gas injection in liquid with internals – strong liquid acceleration. Pressure source 1.1 MPa.

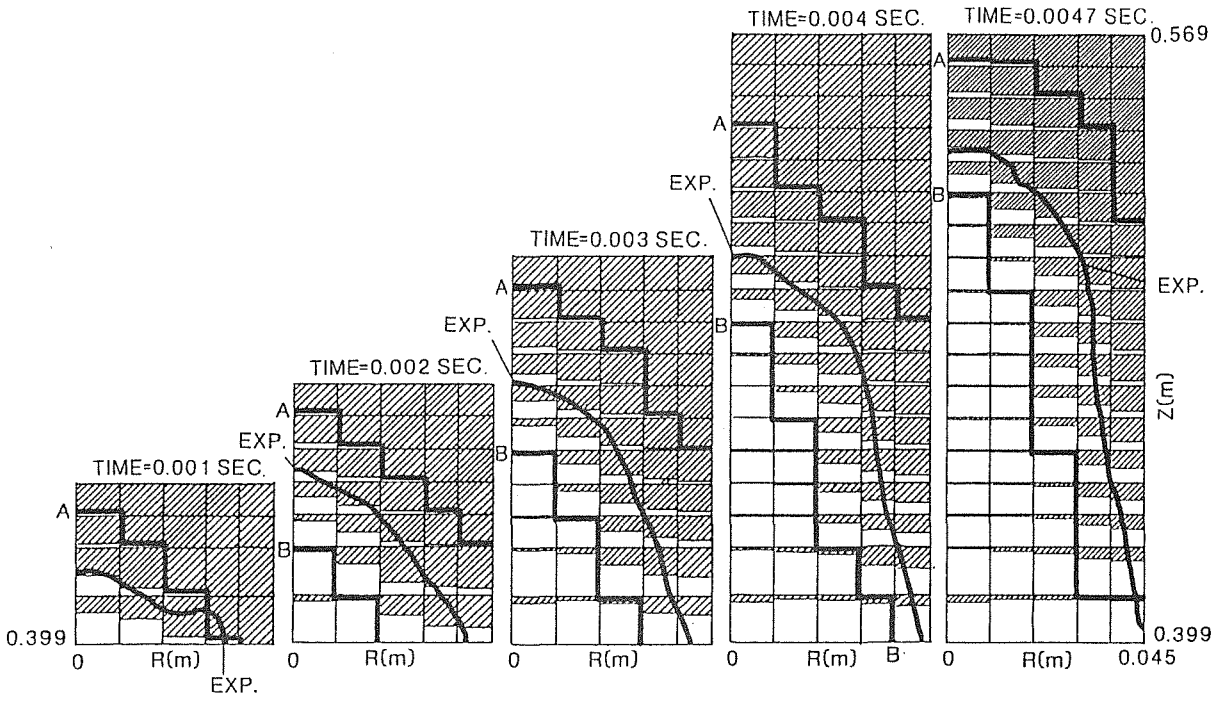


FIGURE 20 a,b,c,d,e. Gas volume fraction as a function of radius and height. Parameter – time. Gas injection in liquid with internals – strong liquid acceleration. Pressure source 1.1 MPa.

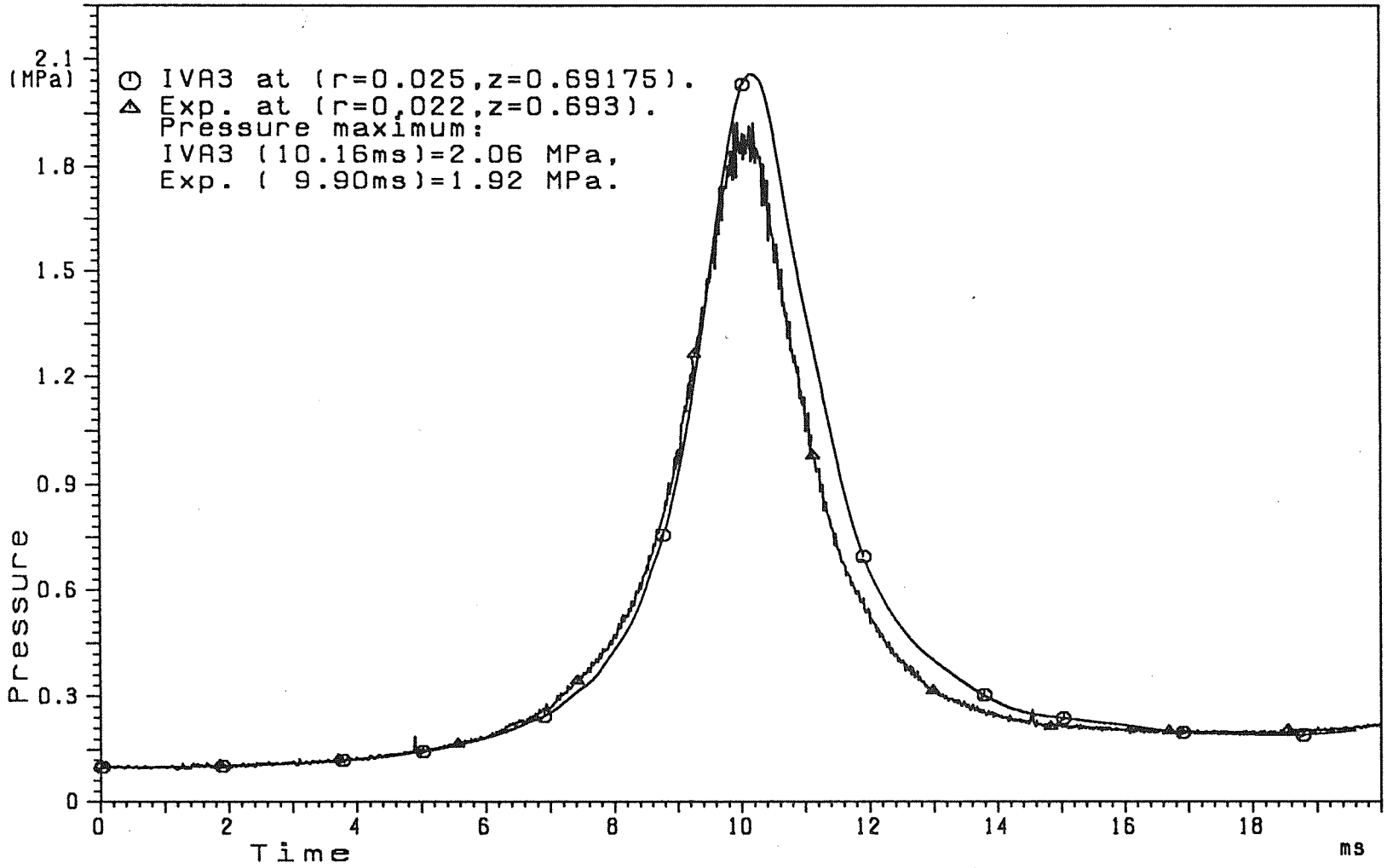


Fig. 21. Pressure as a function of time. Comparison of the IVA3 prediction (26x44 discretization cells) of the total pressure in the center of the computational cell (I=5,K=45) with the measured pressure on the vessel cover at (r=0.022, z=0.693). Meyer-Kirstahler experiment: gas injection in liquid without internals. 6 bar pressure source. ALO=0.001.

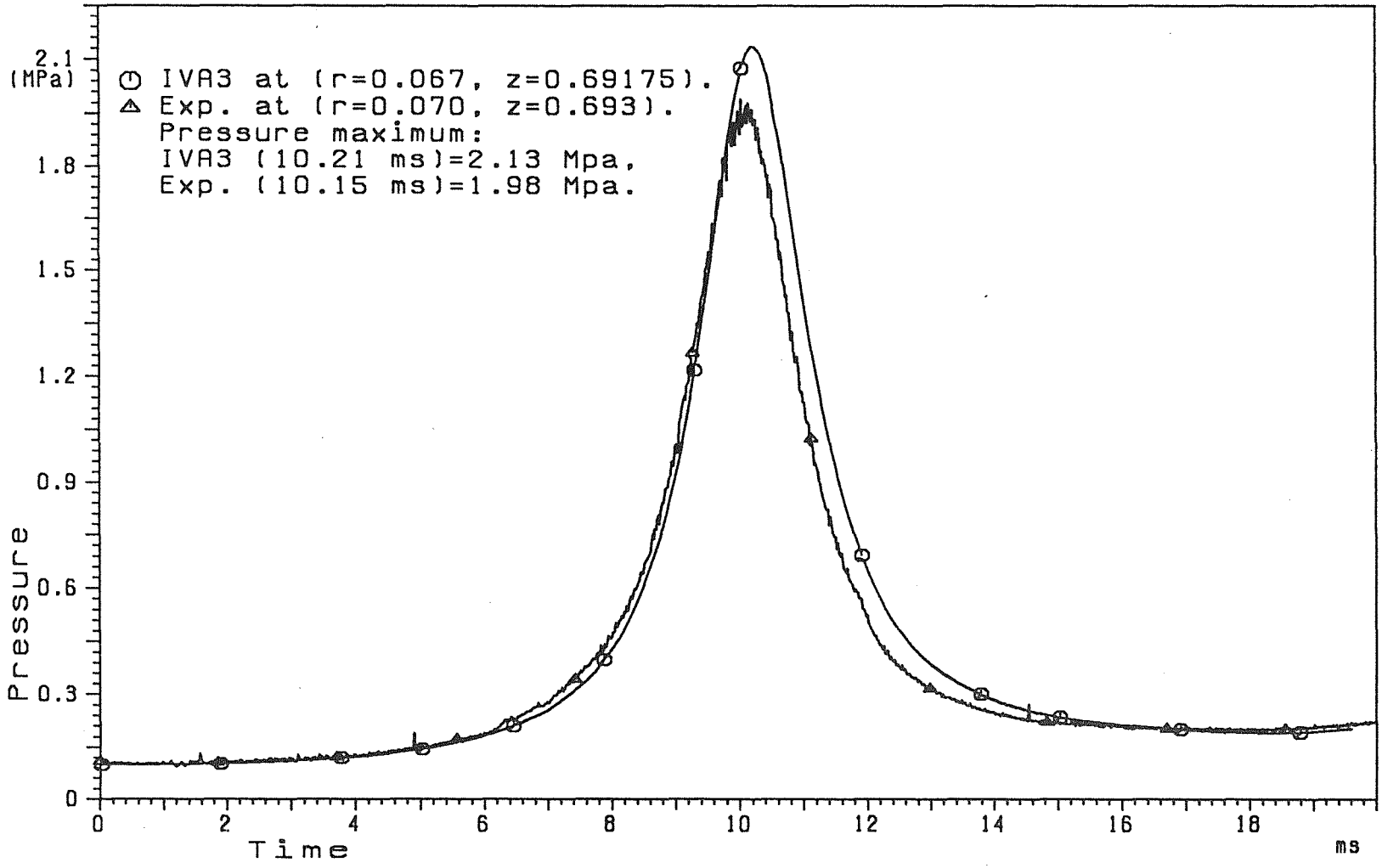


Fig. 22. Pressure as a function of time. Comparison of the IVA3 prediction (26x44 discretization cells) of the total pressure in the center of the computational cell (I=11,K=45) with the measured pressure on the vessel cover at (r=0.07, z=0.693). Meyer-Kirstahler experiment: gas injection in liquid with internals. 6 bar pressure source. ALO=0.001.

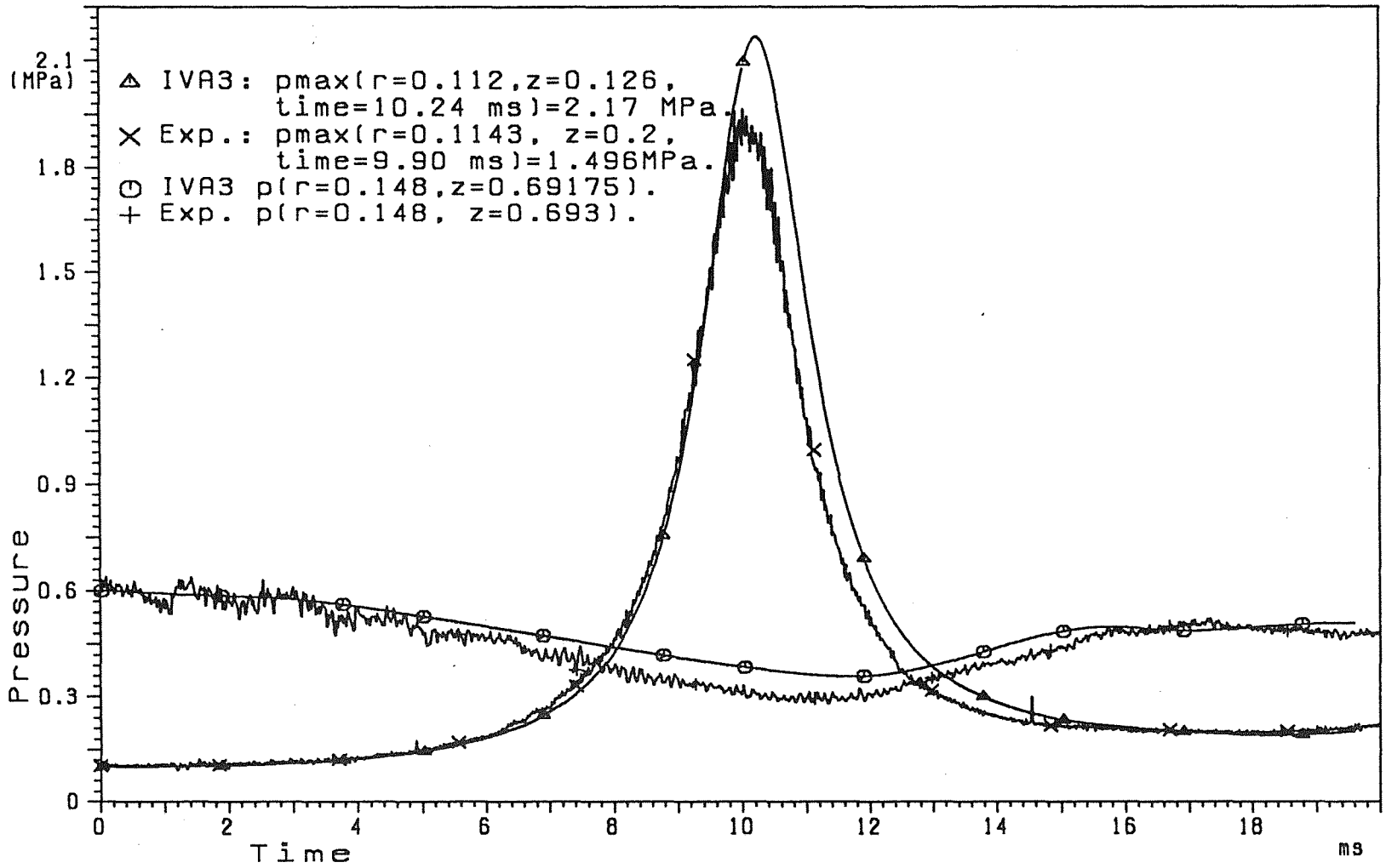


Fig.23. Pressure as a function of time. Comparison of the IVA3 prediction (26x44 discretization cells) of the total pressure in the center of the computational cell (I=25,K=45) and (I=19,K=2) with the measured total pressure on the vessel cover at (r=0.149, z=0.693) and at (r=0.1143, z=0.2), respectively. Meyer-Kirstahler experiment: gas injection in liquid without internals. 6 bar pressure source. ALO=0.001.

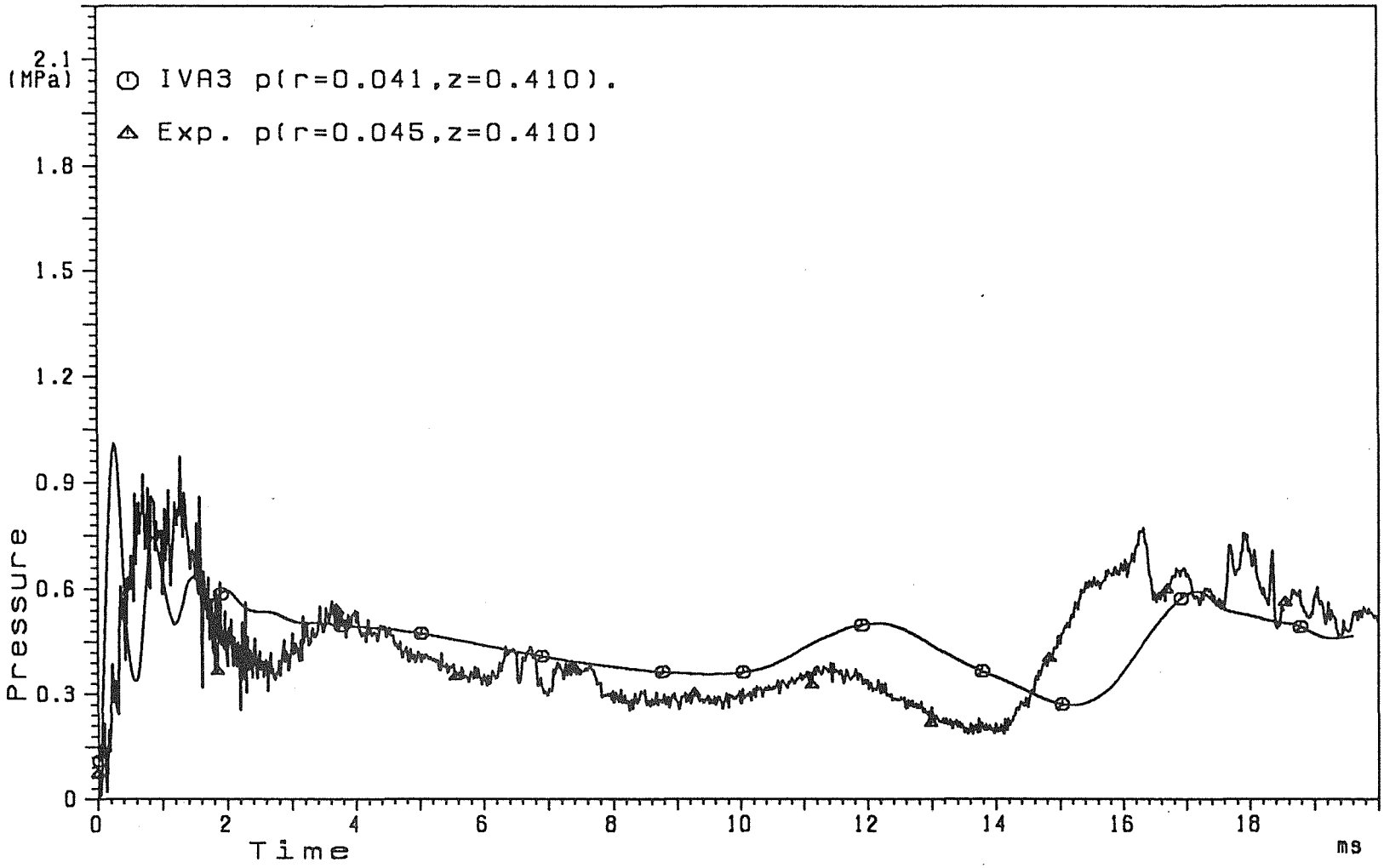


Fig.24 a. Pressure as a function of time. Comparison of the IVA3 prediction (26x44 discretization cells) of the static pressure in the center of the computational cell (I=7,K=5) with the measured pressure on the wall of the gas entrance nozzle. Meyer-Kirstahler experiment: gas injection in liquid without internals. 6 bar pressure source. ALO=0.001.

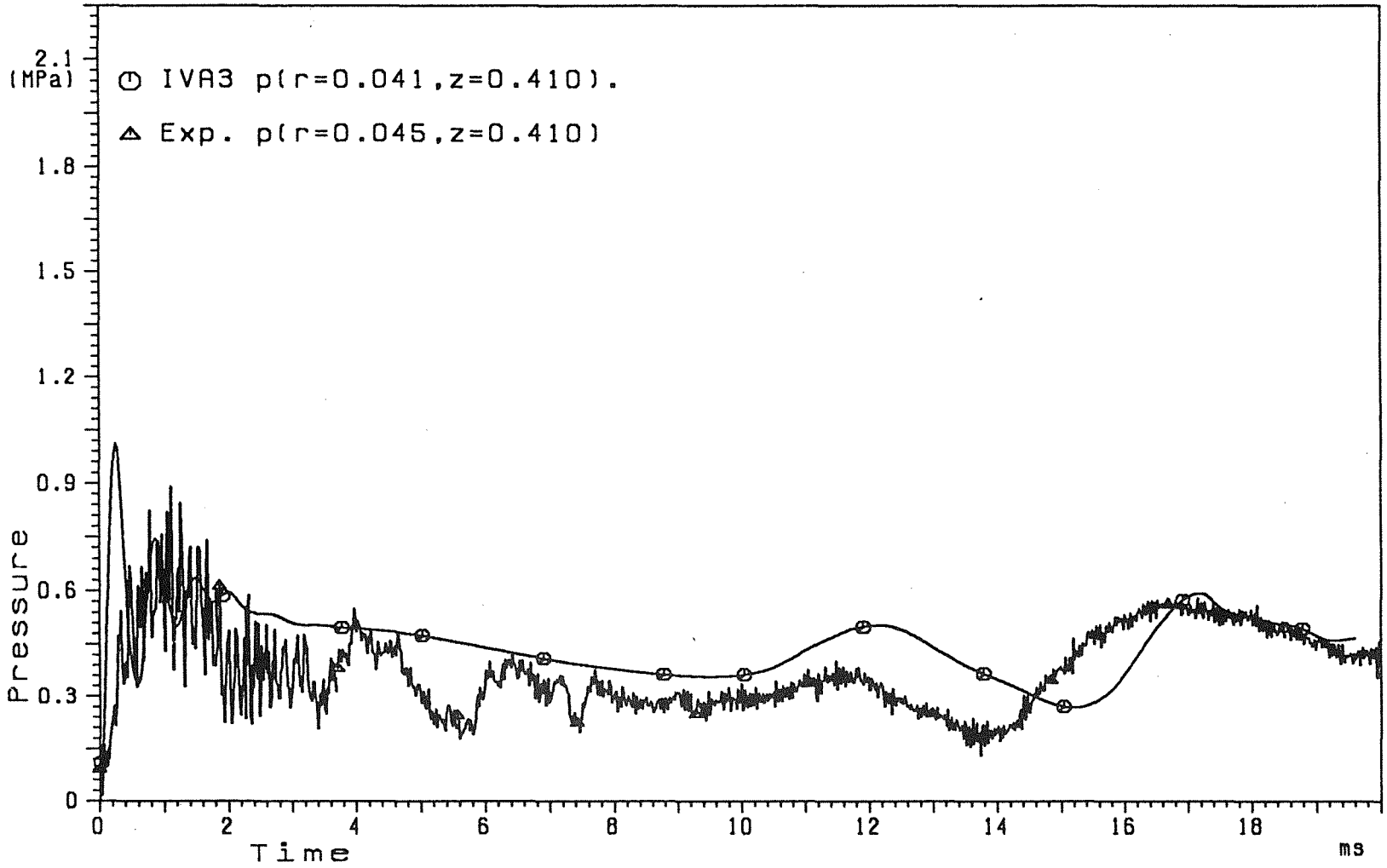


Fig. 24 b. Pressure as a function of time. Comparison of the IVA3 prediction (26x44 discretization cells) of the static pressure in the center of the computational cell (I=7,K=5) with the measured pressure on the wall of the gas entrance nozzle. Meyer-Kirstahler experiment: gas injection in liquid without internals. 6 bar pressure source. ALO=0.001.

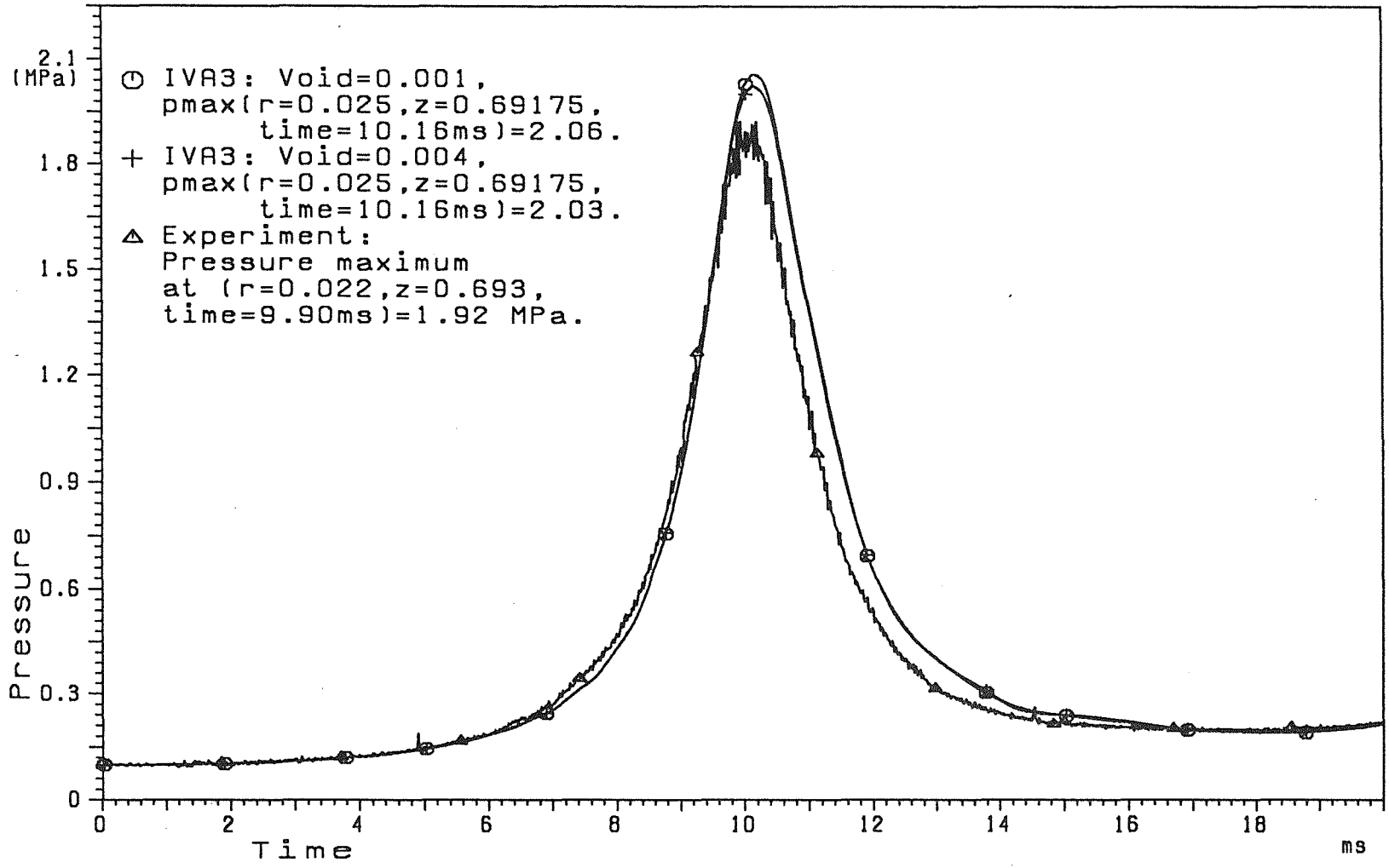


Fig.25. Pressure as a function of time. Comparison of the IVA3 prediction (26x44 discretization cells) of the total pressure in the center of the computational cell (I=5,K=45) with the measured pressure on the vessel cover at (r=0.022, z=0.693). Meyer-Kirstahler experiment: gas injection in liquid without internals. 6 bar pressure source. Sliding doors delay time=0ms.

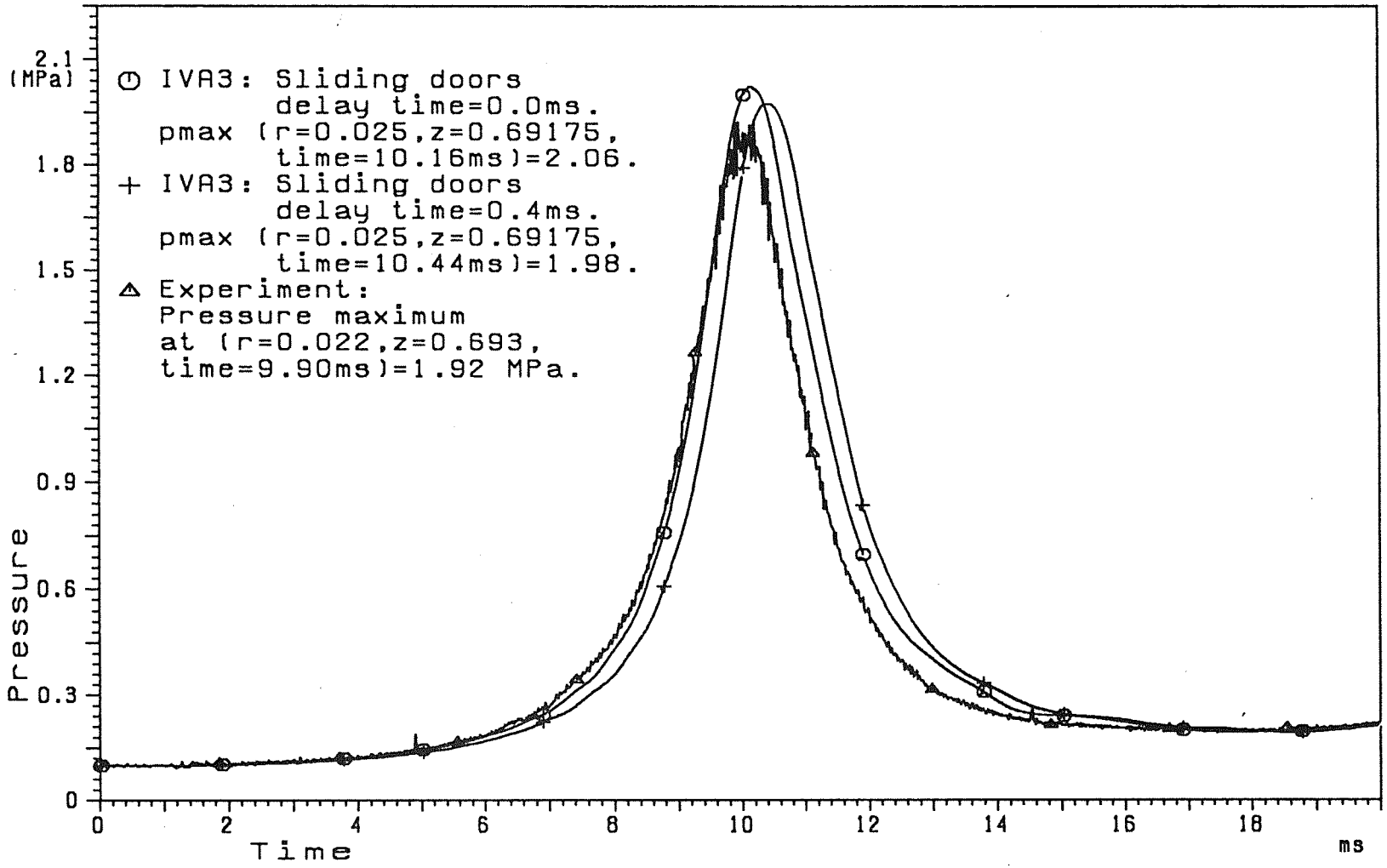


Fig.26. Pressure as a function of time. Comparison of the IVA3 prediction (26x44 discretization cells) of the total pressure in the center of the computational cell (I=5,K=45) with the measured pressure on the vessel cover at (r=0.022, z=0.693). Meyer-Kirstahler experiment: gas injection in liquid without internals. 6 bar pressure source. IVA3: Void=0.004.

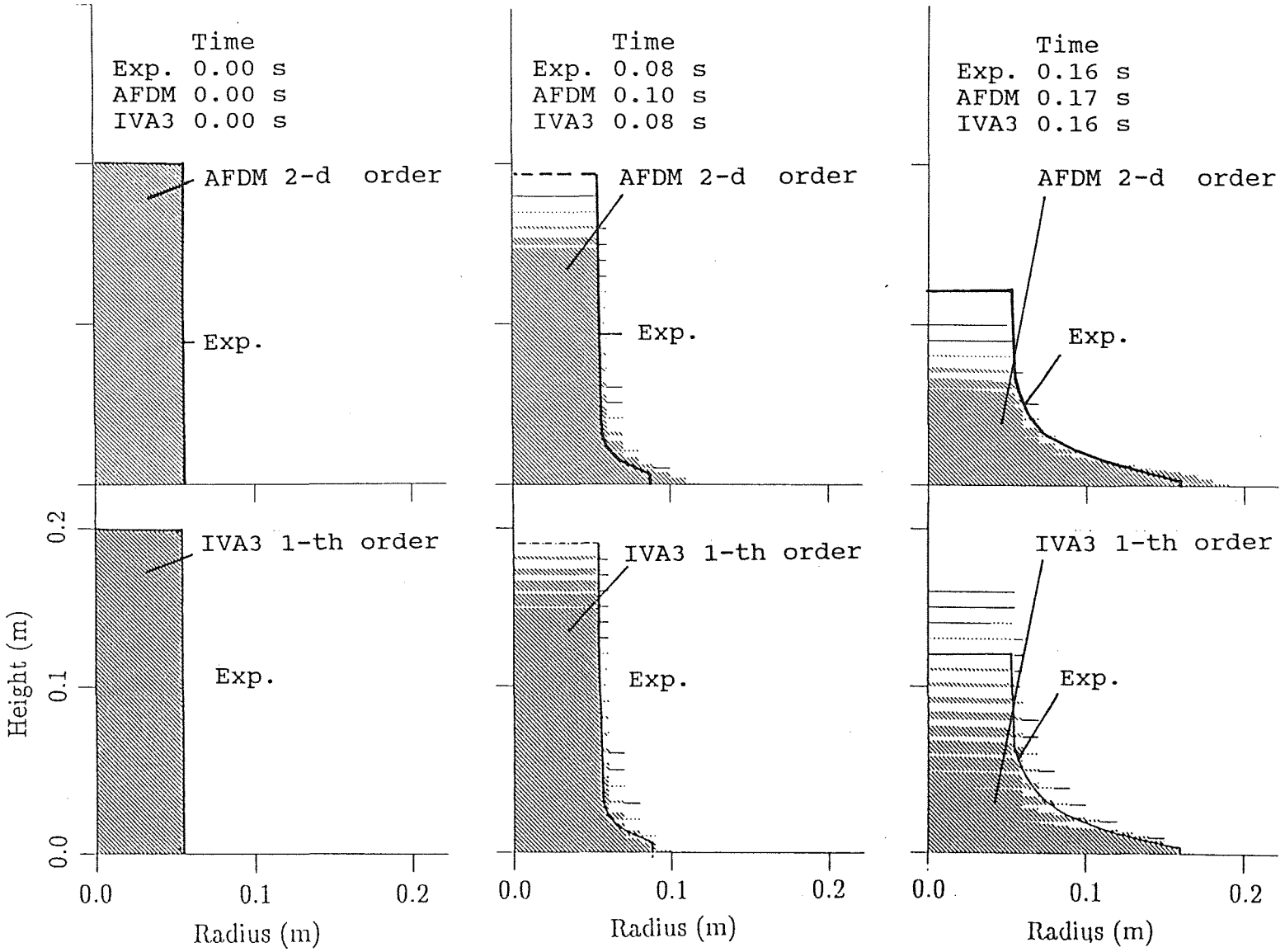


FIGURE 27. Volumetric concentration of water as a function of the radial and axial coordinates at different times from the beginning of the process.

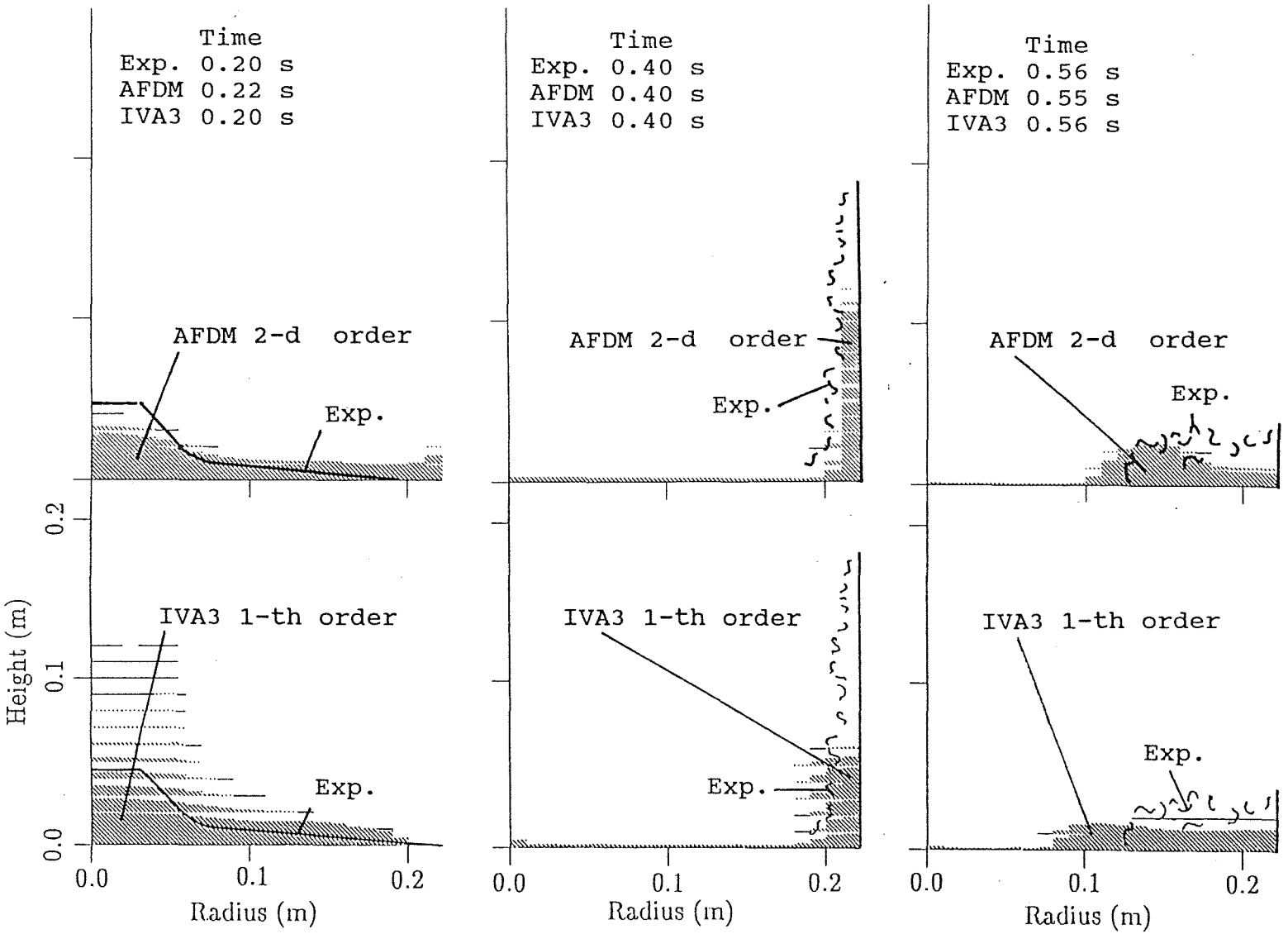


FIGURE 27. Volumetric concentration of water as a function of the radial and axial coordinates at different times from the beginning of the process.

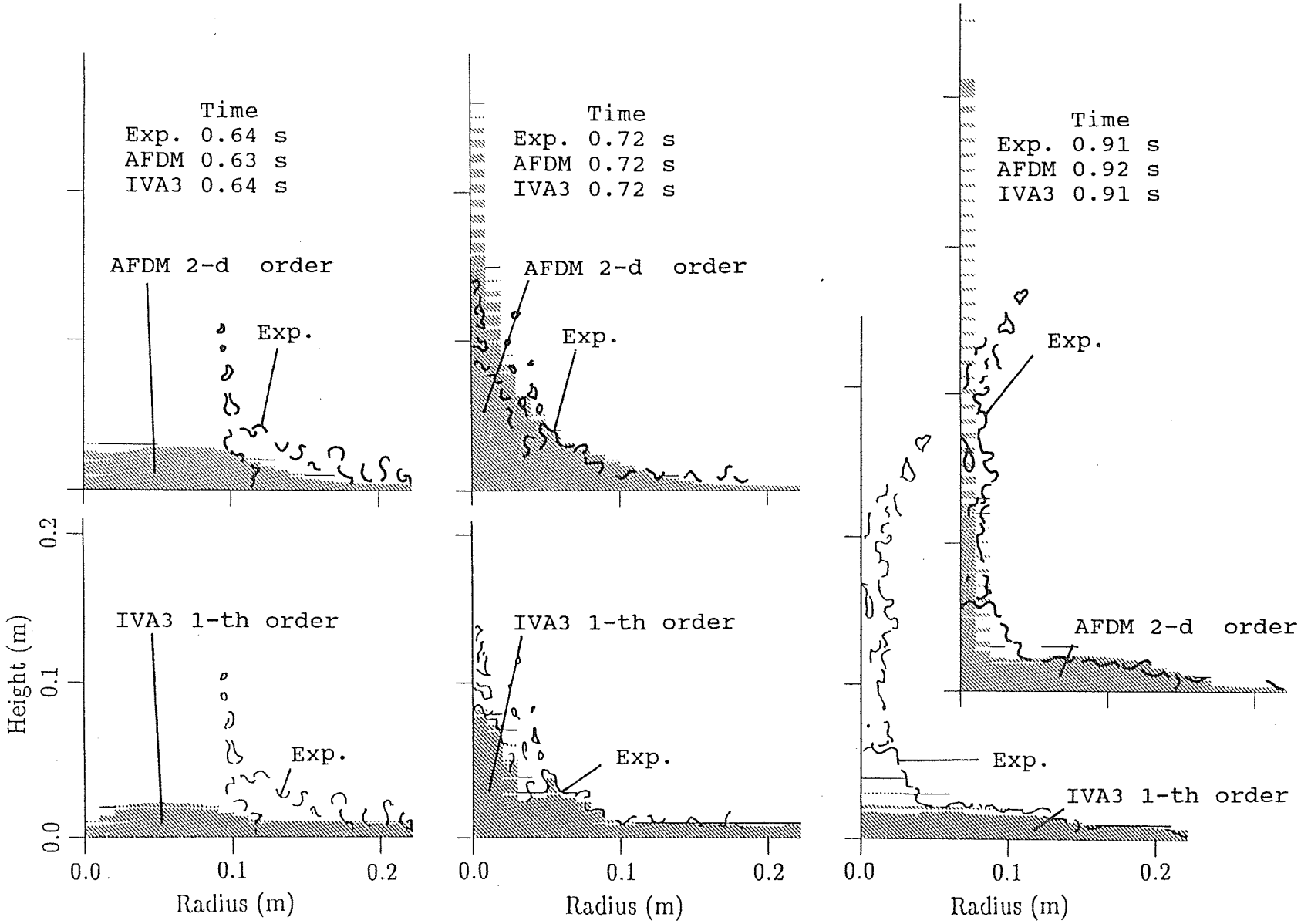


FIGURE 27. Volumetric concentration of water as a function of the radial and axial coordinates at different times from the beginning of the process.

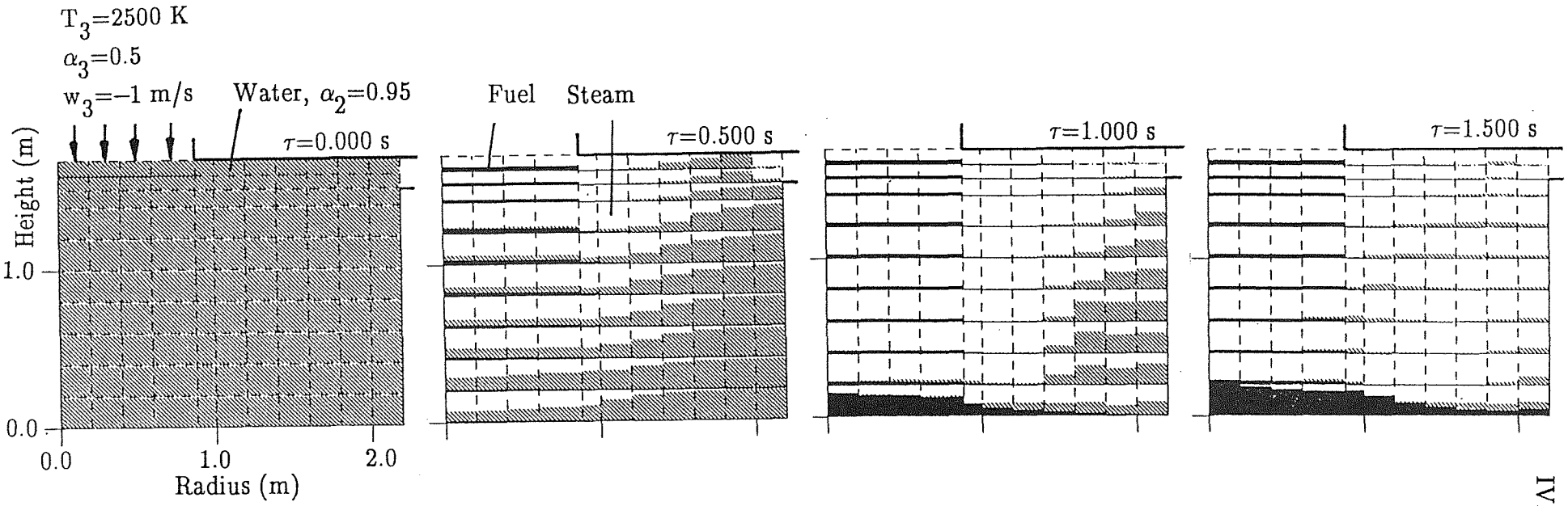


Fig. 28. Fuel, Water and Steam Volumetric Fraction as a Function of Space. Parameter – time.

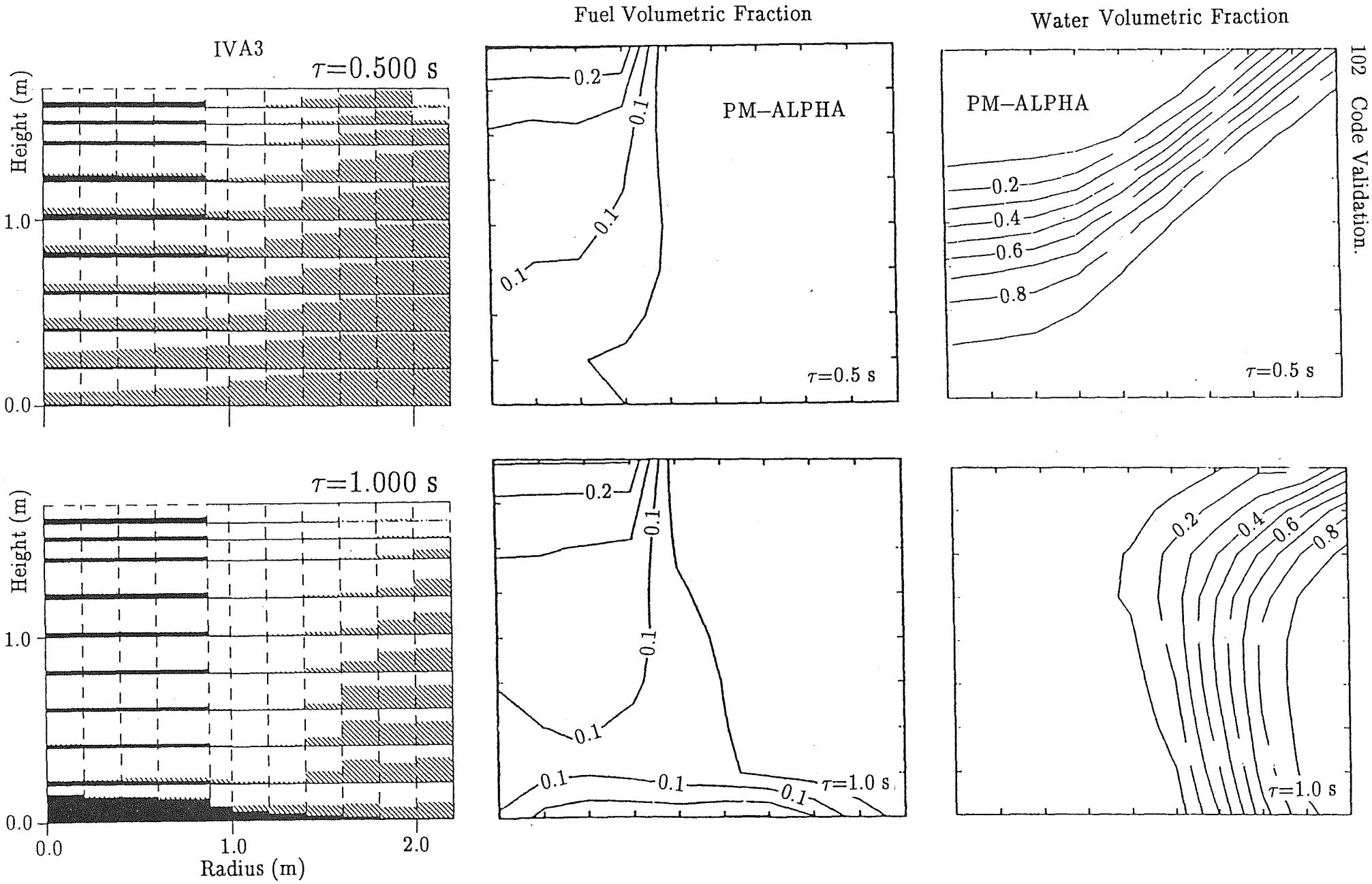


FIGURE 29. Predictions of particle and water volumetric fraction distributions at 0.5 and 1 s. Comparison of IVA3 prediction with that obtained by Amarasooriya and Theofanous with PM–ALPHA code.

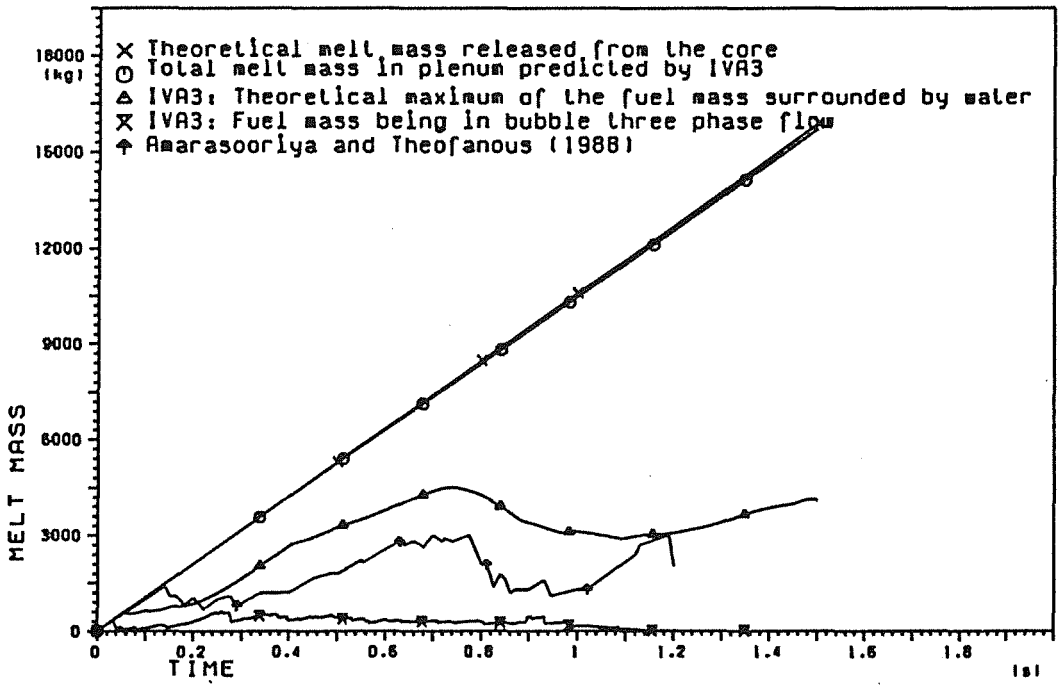


FIGURE 30. Fuel Mass Transients: Comparison of the IVA3 – prediction with the Amarasooriya and Theofanous predictions.

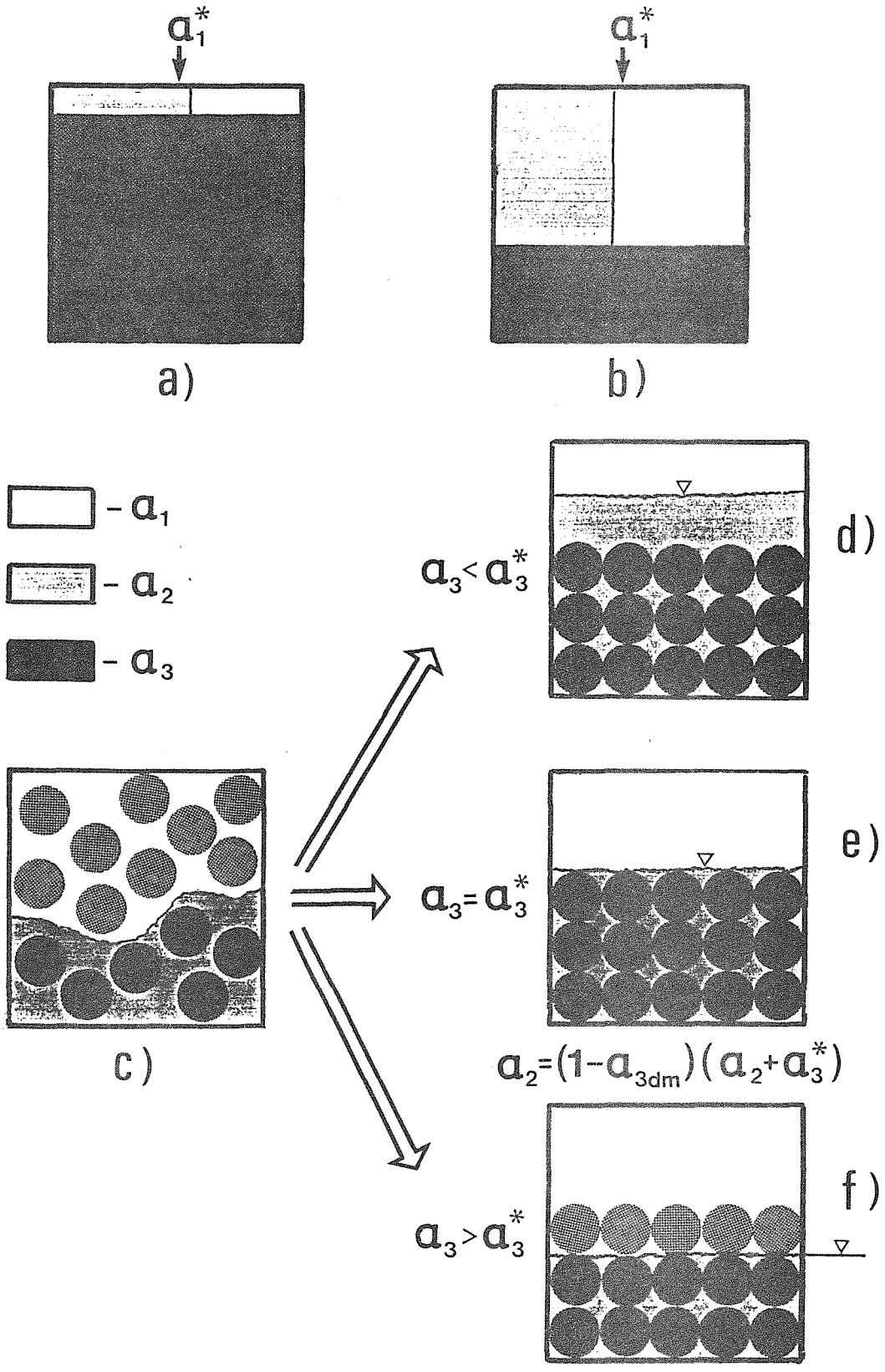


FIGURE 31. Mixing criteria. a) Abolfadl et al. criterion fulfilled for cell predominantly occupied by fuel. b) Abolfadl et al. criterion not fulfilled for cell occupied approximately uniformly by fuel, steam, an liquid. c–f) Explanation to the estimation of the fuel mass surrounded by liquid.

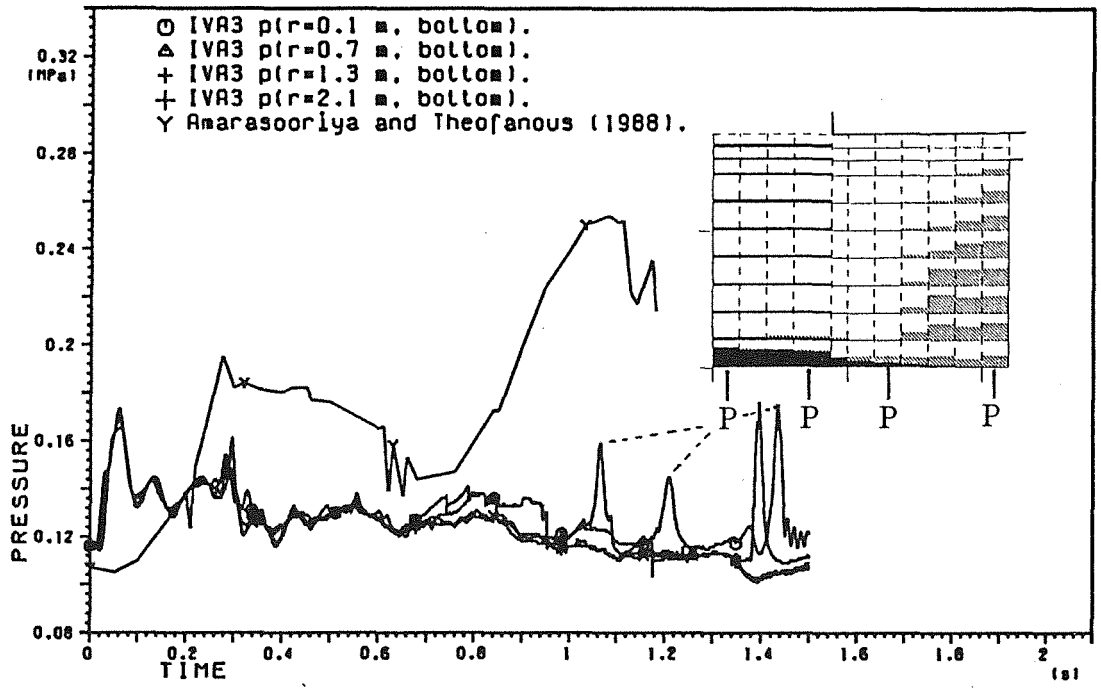


FIGURE 32. Bottom pressure transients: Comparison of the IVA3 prediction with the Amarasooriya and Theofanous prediction.

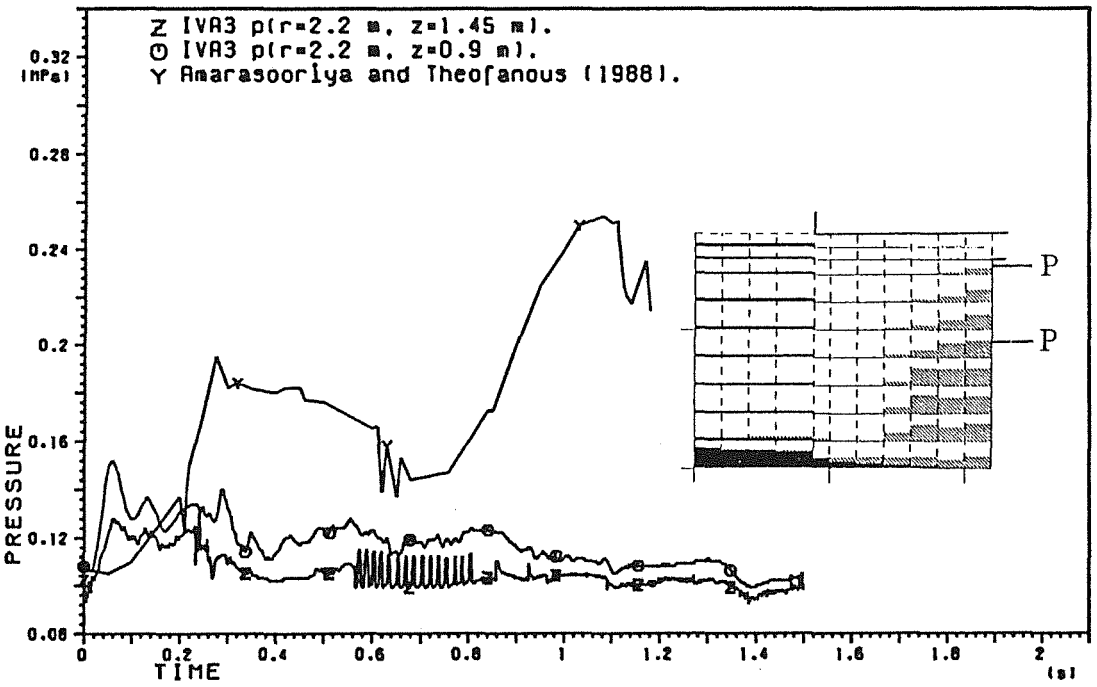


FIGURE 33. Wall pressure transients: Comparison of the IVA3 prediction with the Amarasooriya and Theofanous prediction.

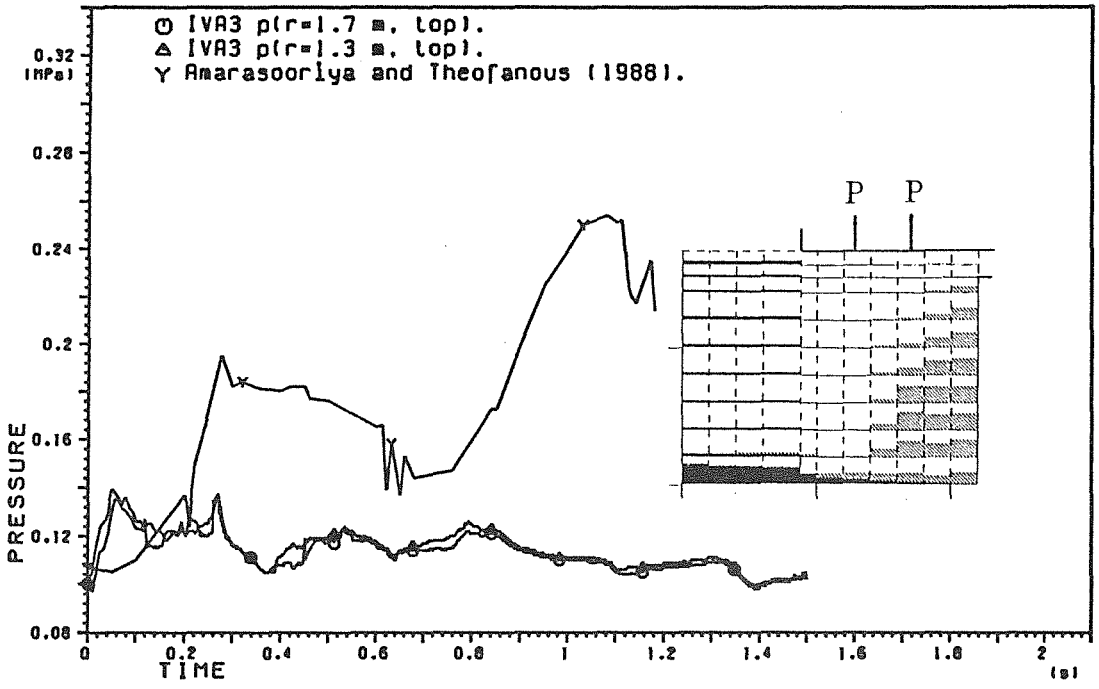


FIGURE 34. Top pressure transients: Comparison of the IVA3 prediction with the Amarasooriya and Theofanous prediction.

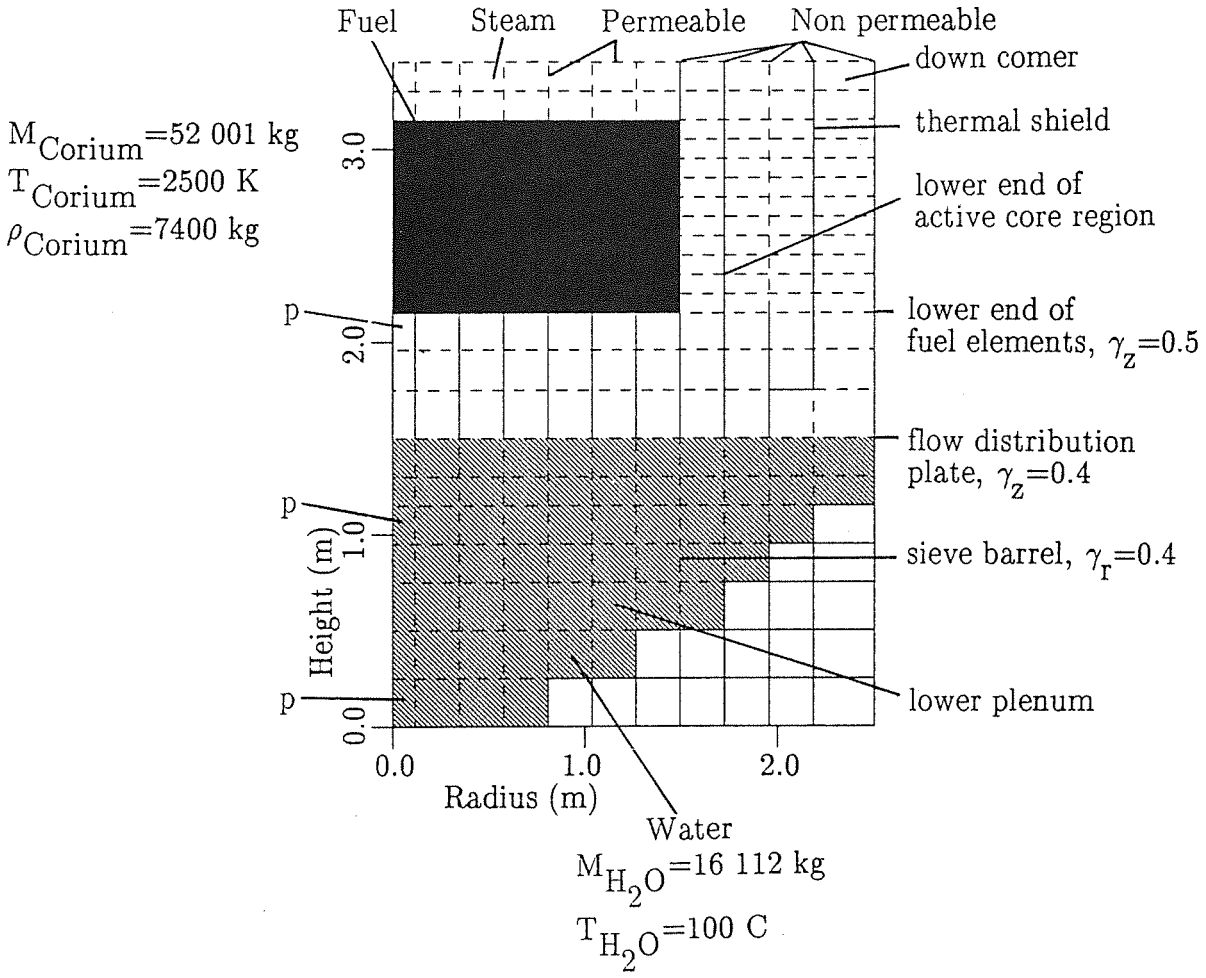


FIGURE 35. Geometry of typical PWR–1300 type reactor. Cell nodding diagram for IVA3.

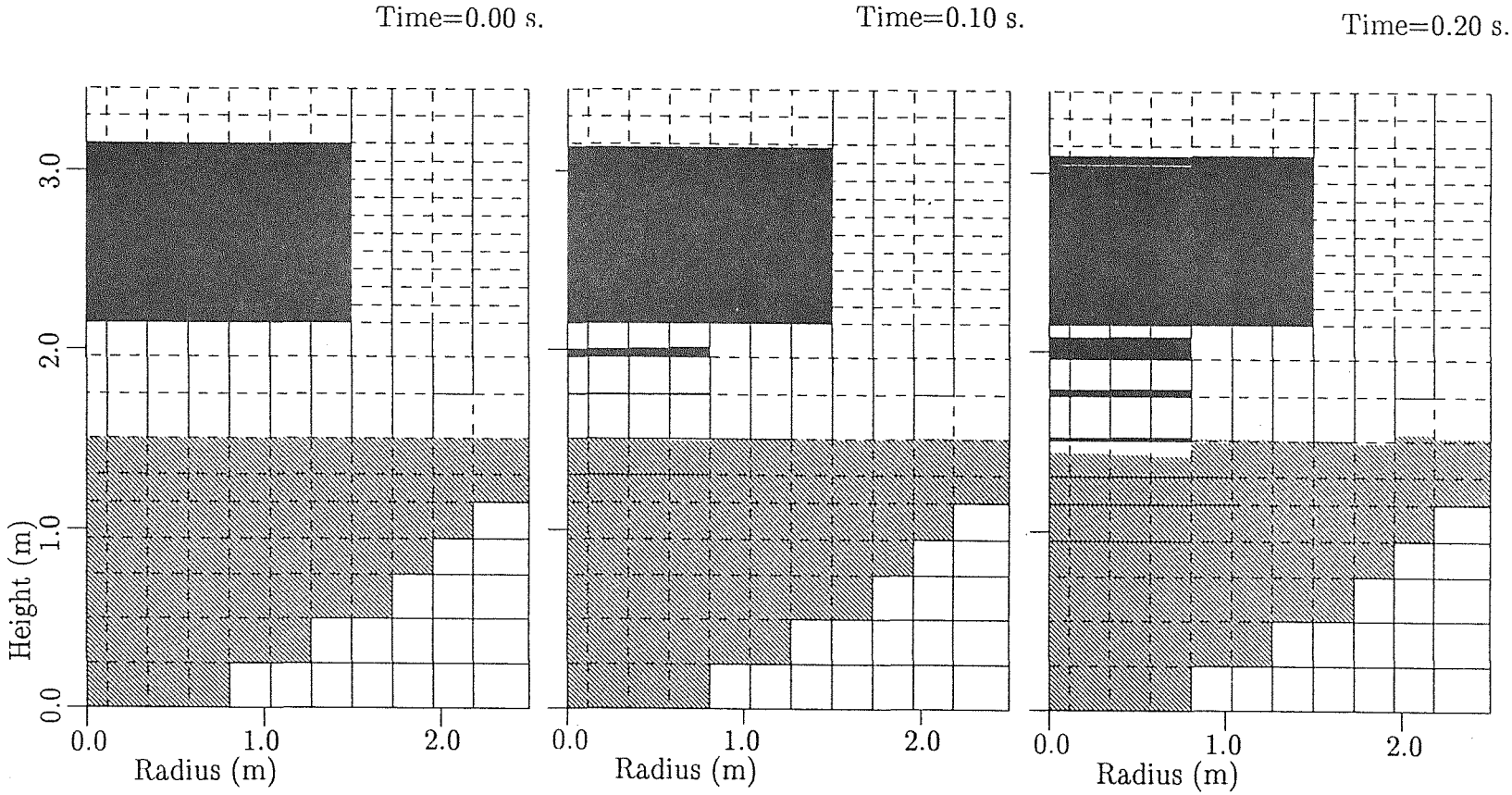


FIGURE 36. Fuel, water and steam volumetric fraction as a function of space. Parameter time. IVA3 prediction for a PWR–1300 type reactor.

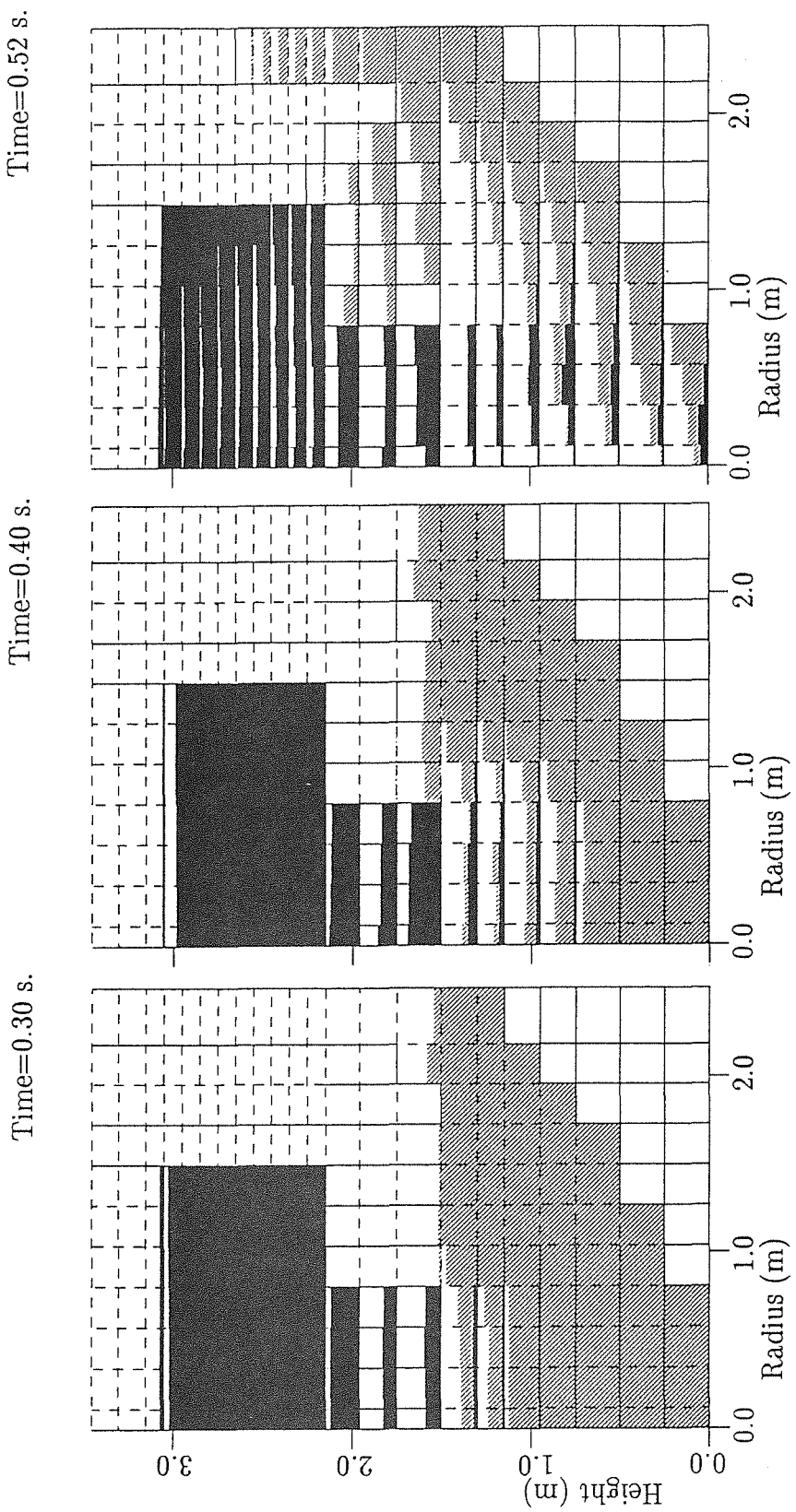
Time=0.52 s.
Time=0.40 s.
Time=0.30 s.
Radius (m)
0.0
1.0
2.0
Height (m)
0.0
1.0
2.0
3.0

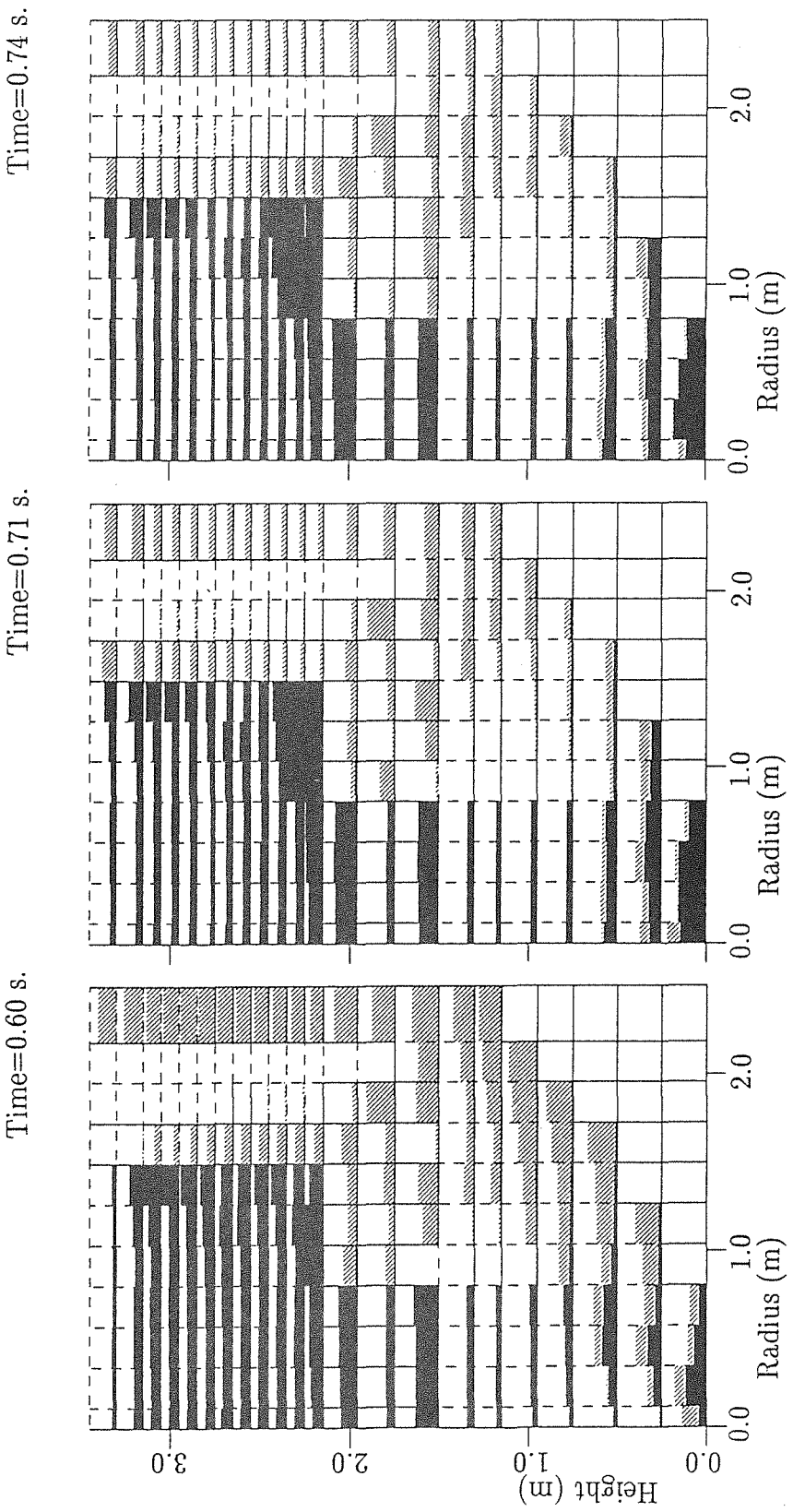
Time=0.74 s.
Time=0.71 s.
Time=0.60 s.
Radius (m)
0.0
1.0
2.0
Height (m)
0.0
1.0
2.0
3.0

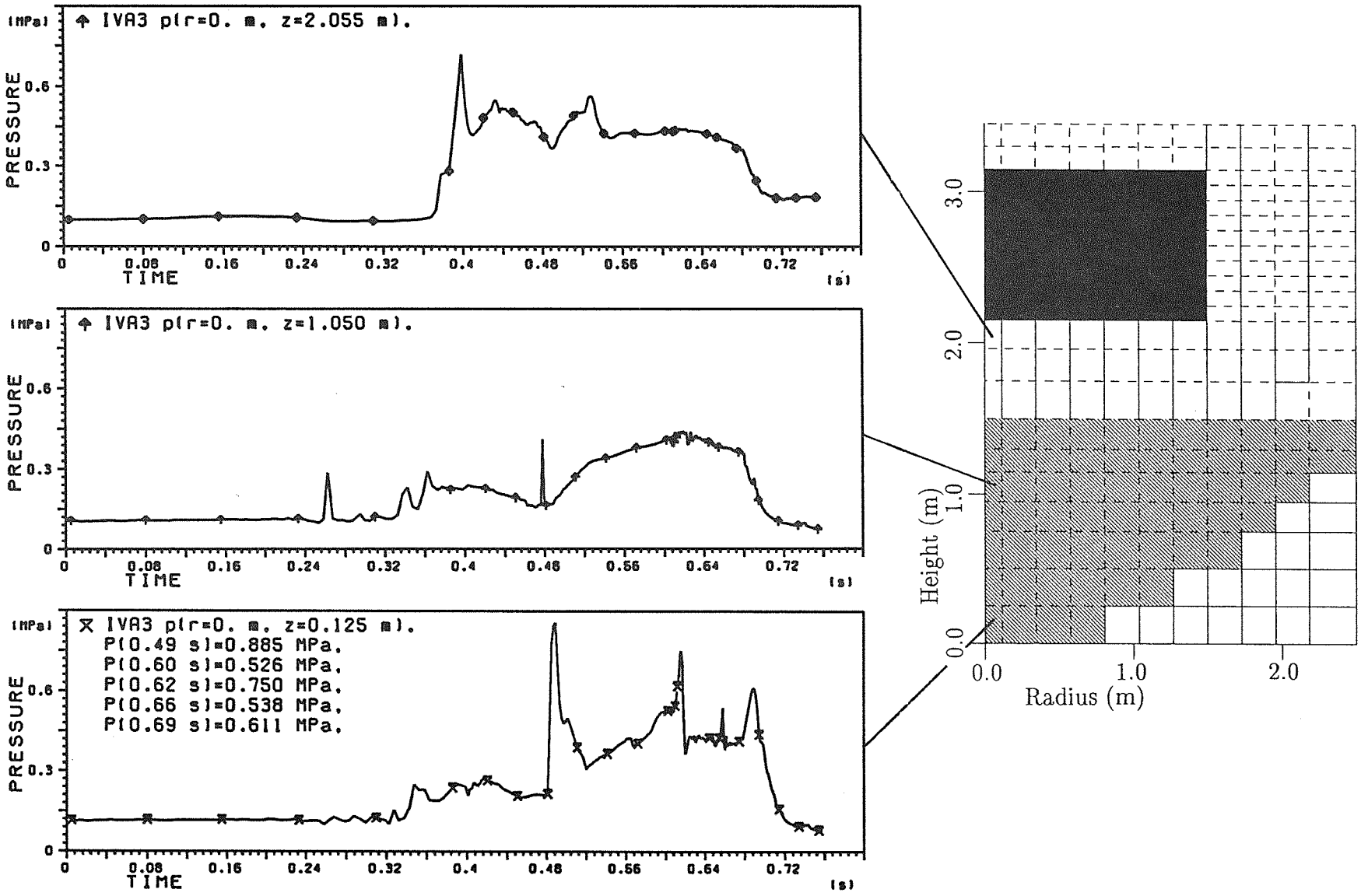


FIGURE 37. Pressure transients in lower plenum due to premixing. IVA3 Prediction for typical PWR 1300 reactor.

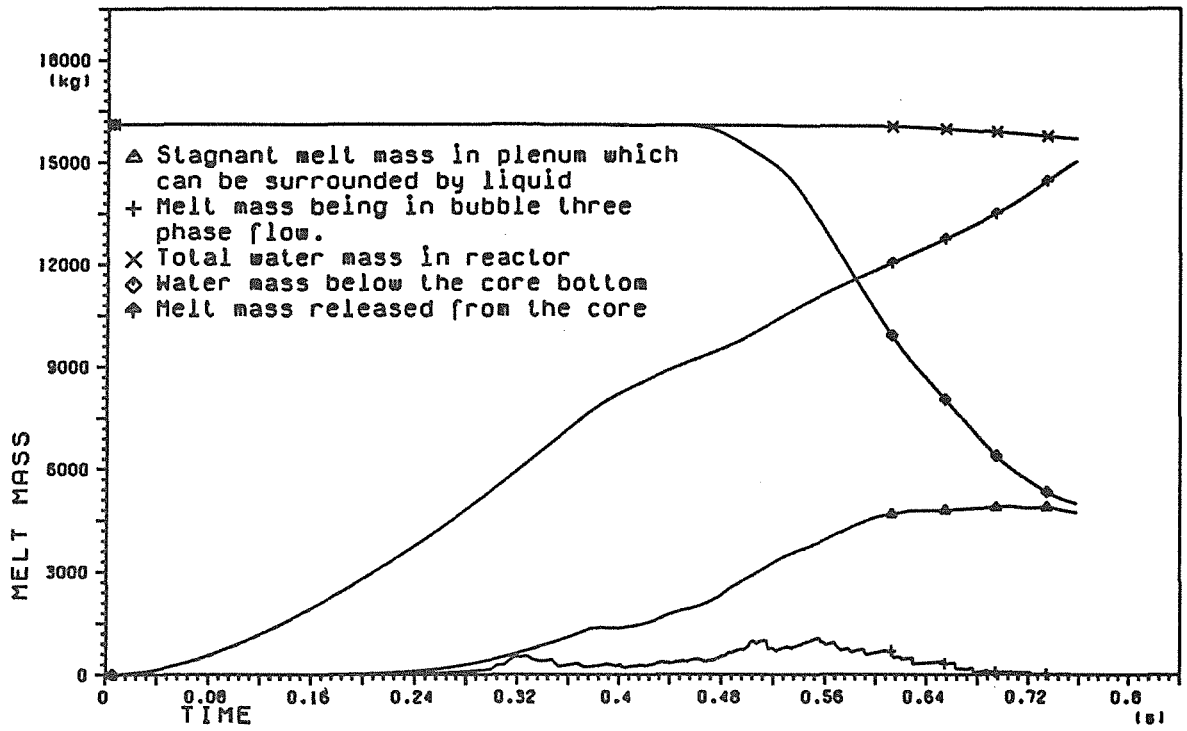


FIGURE 38. IVA3 prediction of fuel mass transients in typical PWR 1300 reactor.

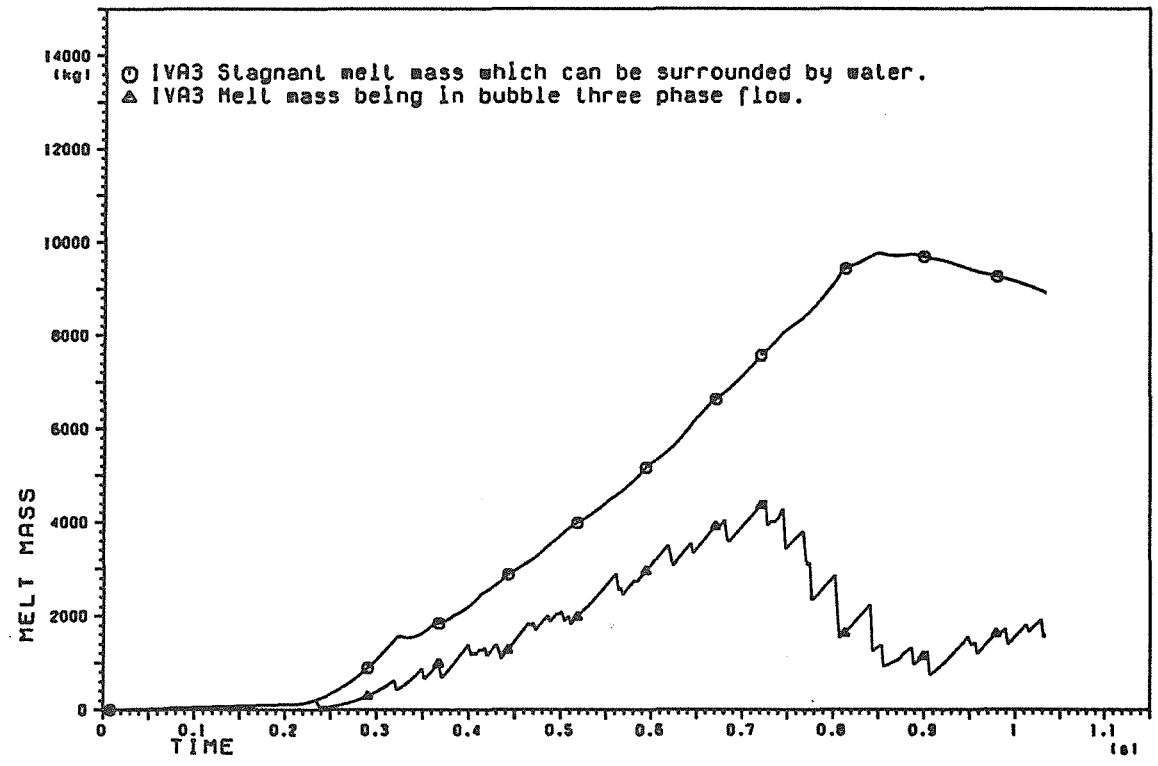


FIGURE 39. Melt mass surrounded by liquid as a function of time. Particle diameter 0.01 m, discharge circle with diameter of 1.8 m and axial permeability of 0.5, $\rho_3=\rho_{UO_2}$, no flow distribution plate.

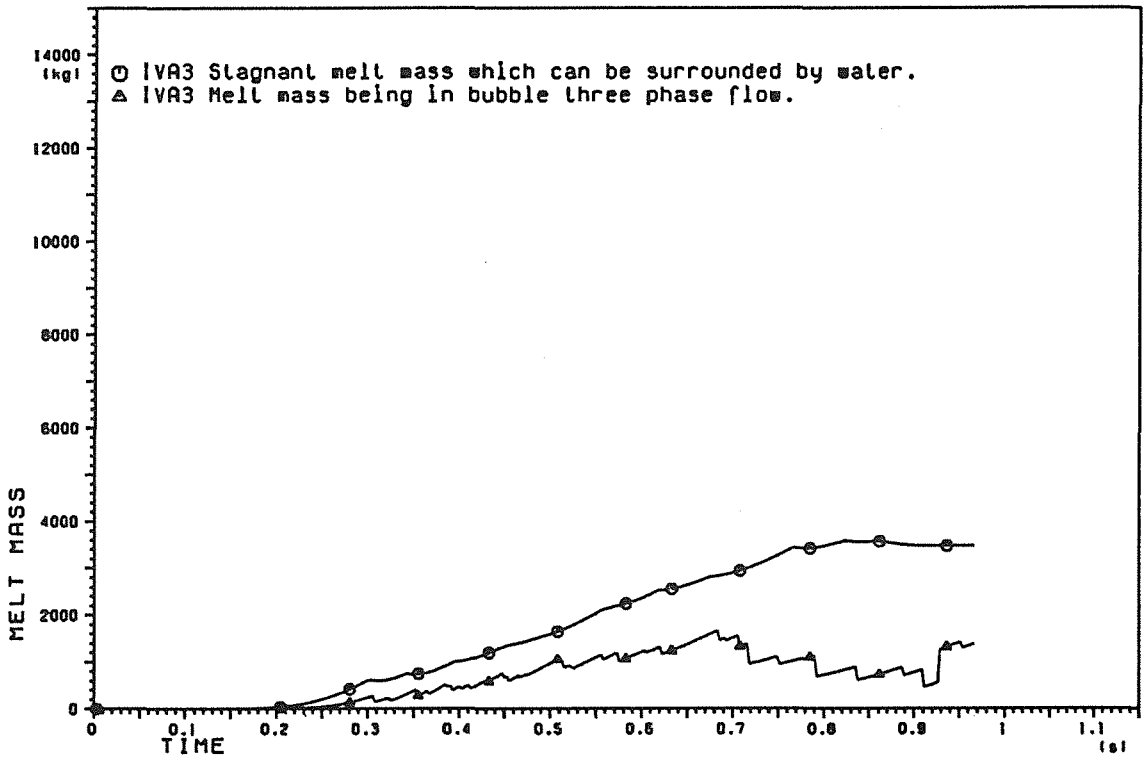


FIGURE 42. Melt mass surrounded by liquid as a function of time. Case D: particle diameter 0.01 m, discharge circle with diameter 1.2 m and axial permeability of 0.5, $\rho_3=\rho_{UO_2}$, no flow distribution plate.

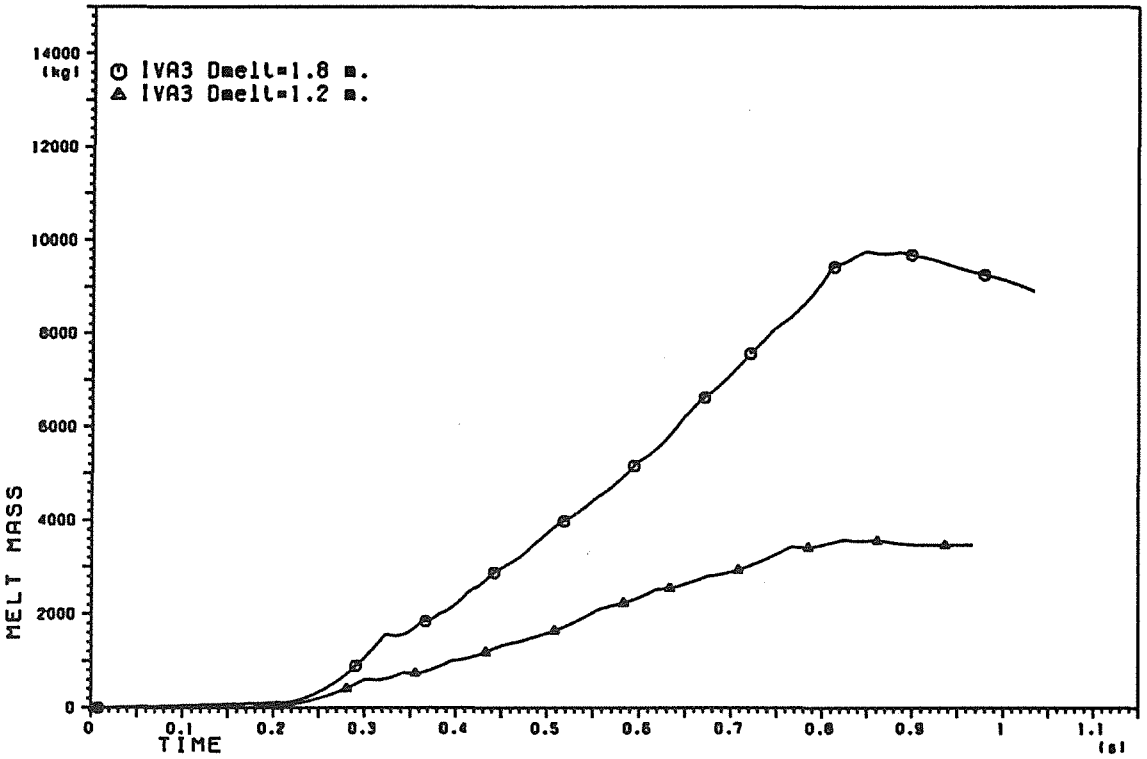


FIGURE 43. Comparison of the melt mass surrounded by liquid for two different cases: case B with discharge circle with diameter of 1.8 m and axial permeability of 0.5 and case D with discharge circle with diameter of 1.2 m.

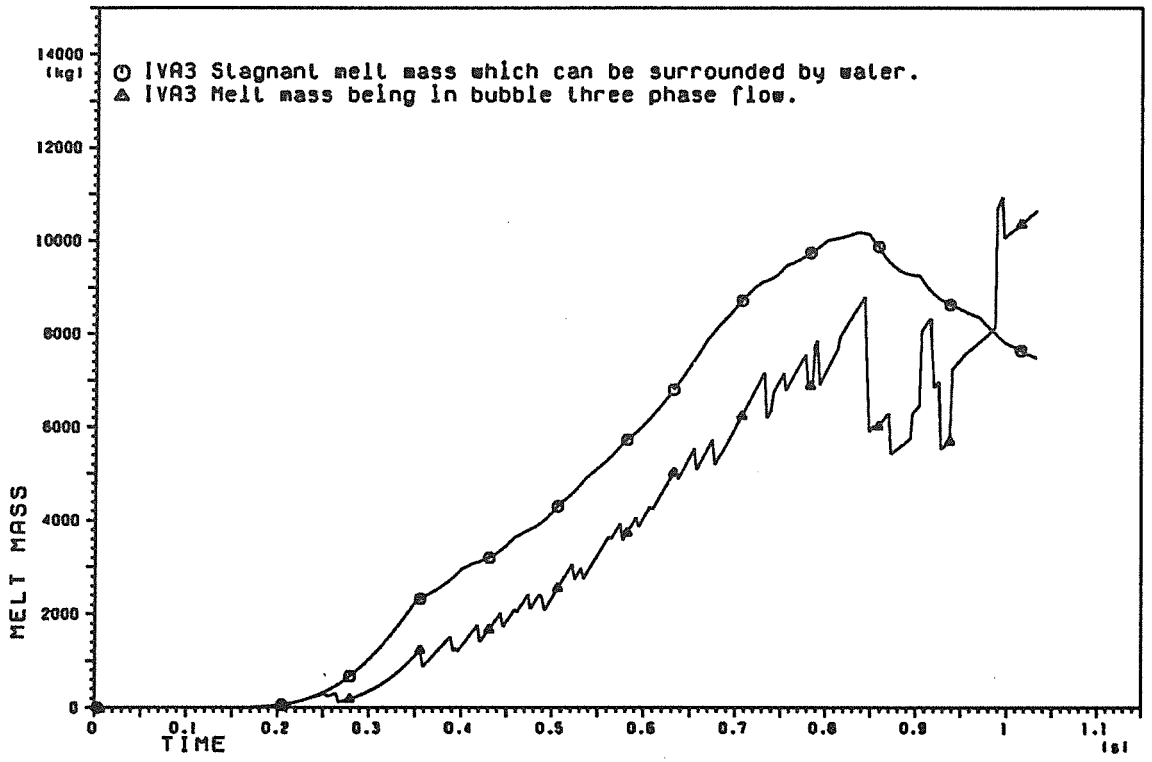


FIGURE 40. Melt mass surrounded by liquid as a function of time. Case C: particle diameter 0.02 m, discharge circle with diameter of 1.8 m and axial permeability of 0.5, $\rho_3=\rho_{UO_2}$, no flow distribution plate.

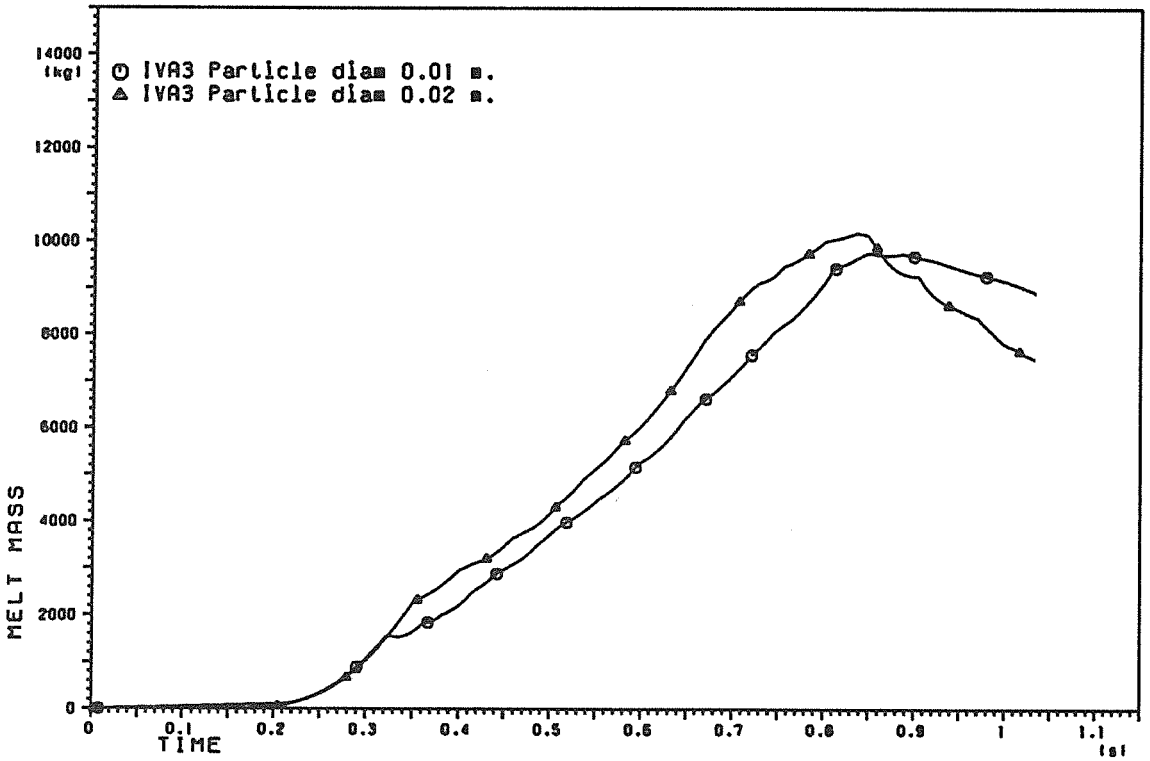


FIGURE 41. Comparison of the melt mass surrounded by liquid for two different cases: case B with particle size of 0.01 m and case C with particle size of 0.02 m.

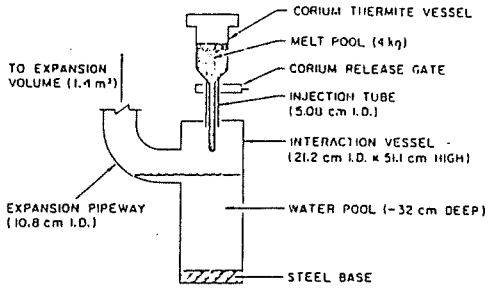


FIGURE 44. Basic elements of the experimental apparatus.

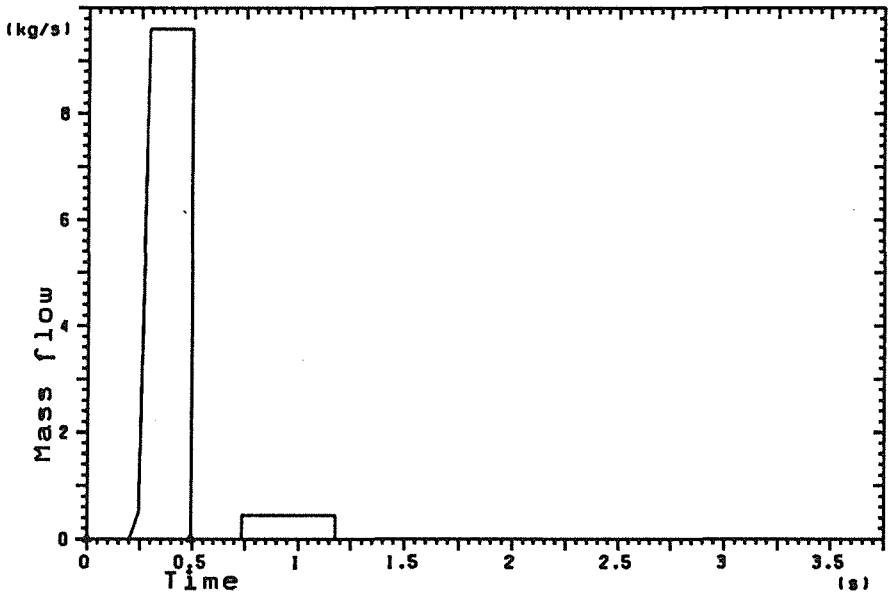


FIGURE 45. Injected corium mass flow in the ANL CWTI9 experiment.

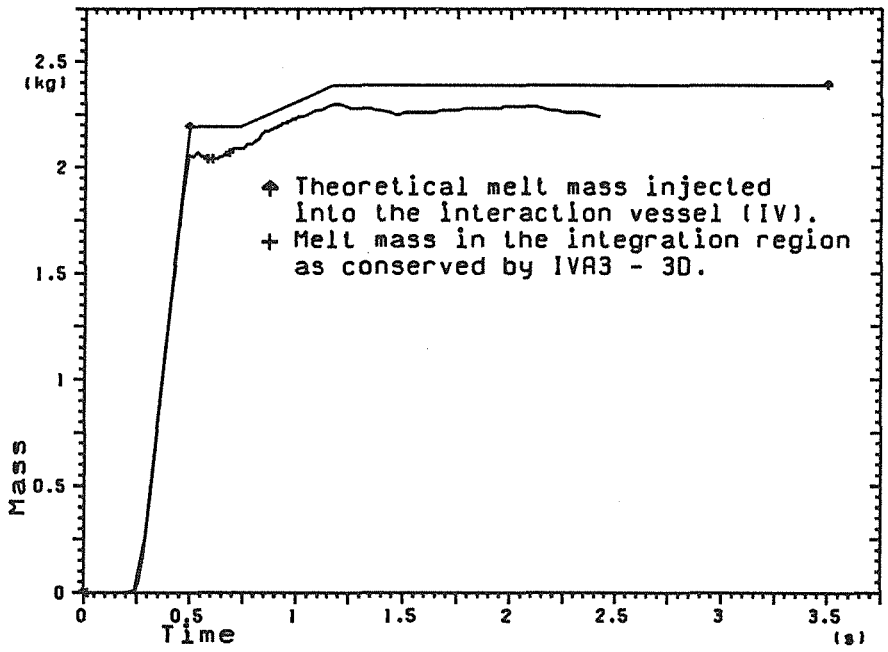


FIGURE 46. Total corium mass conservation predicted by IVA3 for CWTI9 experiment.

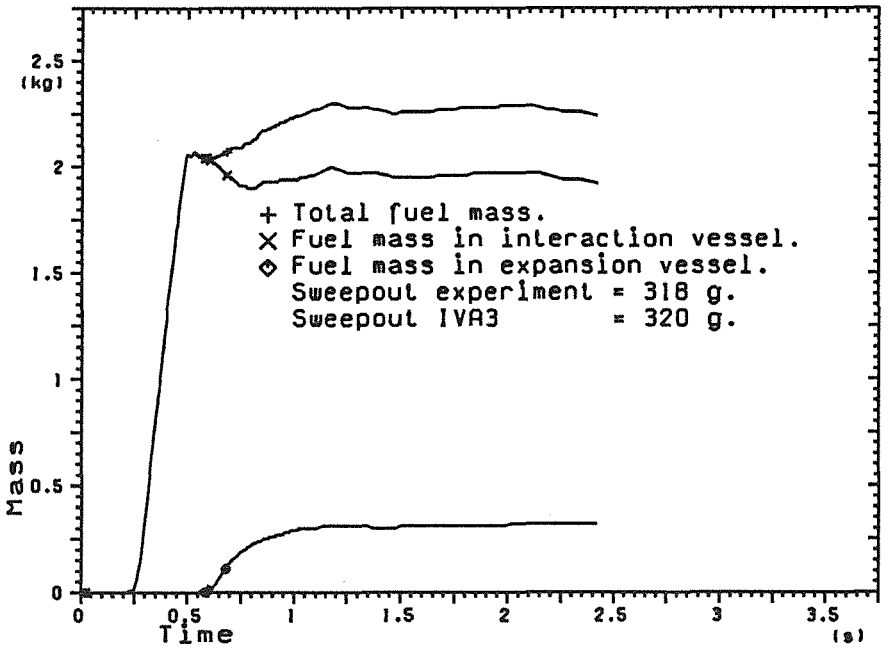


FIGURE 47. Corium mass distribution as a function of time for CWTI9 experiment as predicted by IVA3 3D simulation.

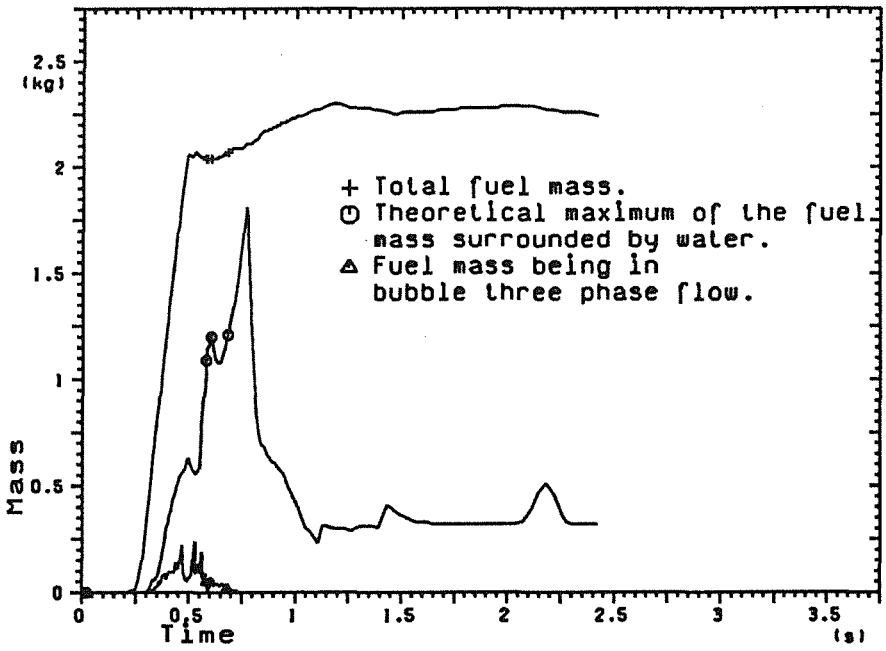


FIGURE 48. Limits of the corium water intermixing as a function of time. IVA3 3D prediction of the ANL CWTI9 experiment.

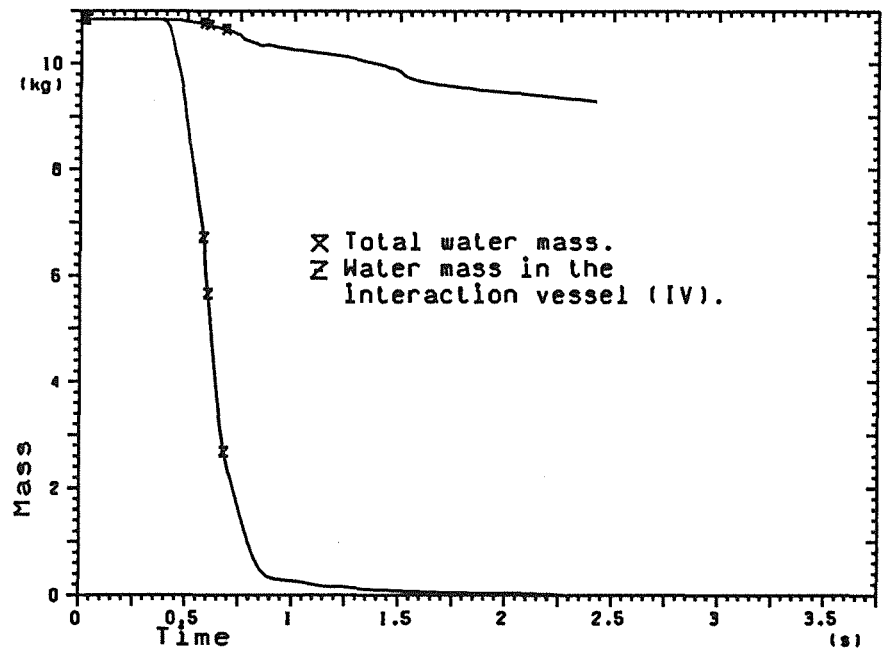


FIGURE 49. Water mass distribution versus time. IVA3 3D prediction of the ANL CWTI9 experiment.

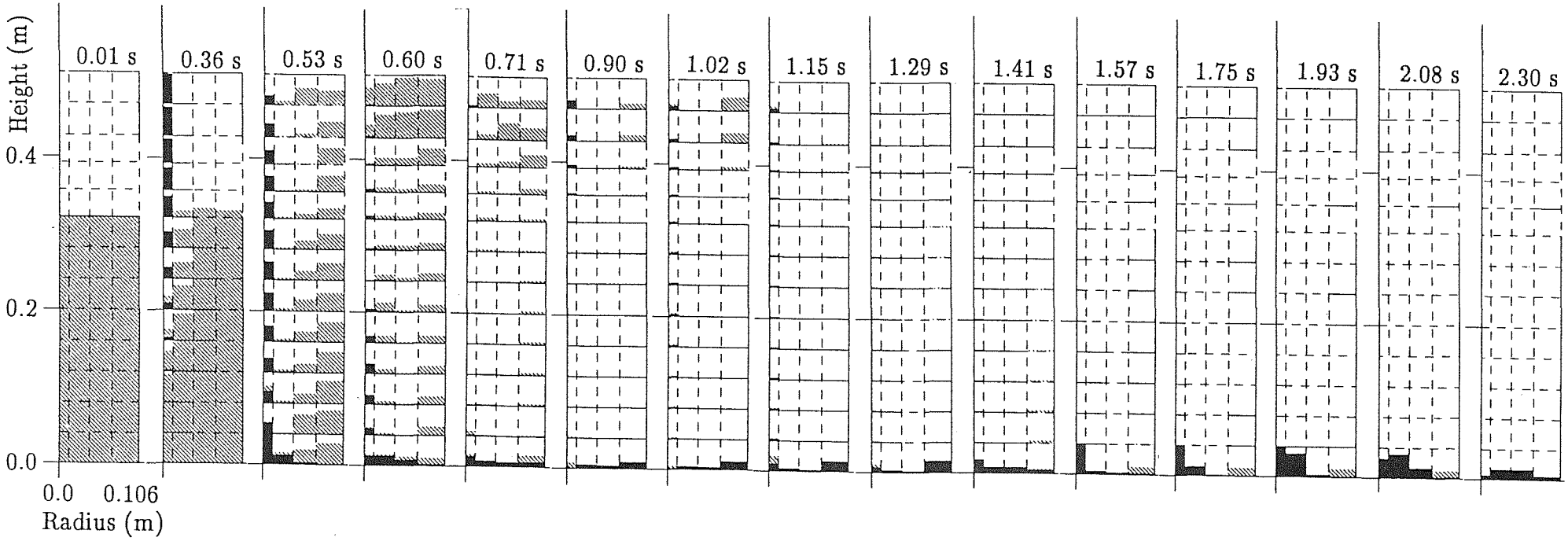


FIGURE 50. Volumetric fractions of the three components in the IV for different times in the first angular sector containing the escape pipeway.

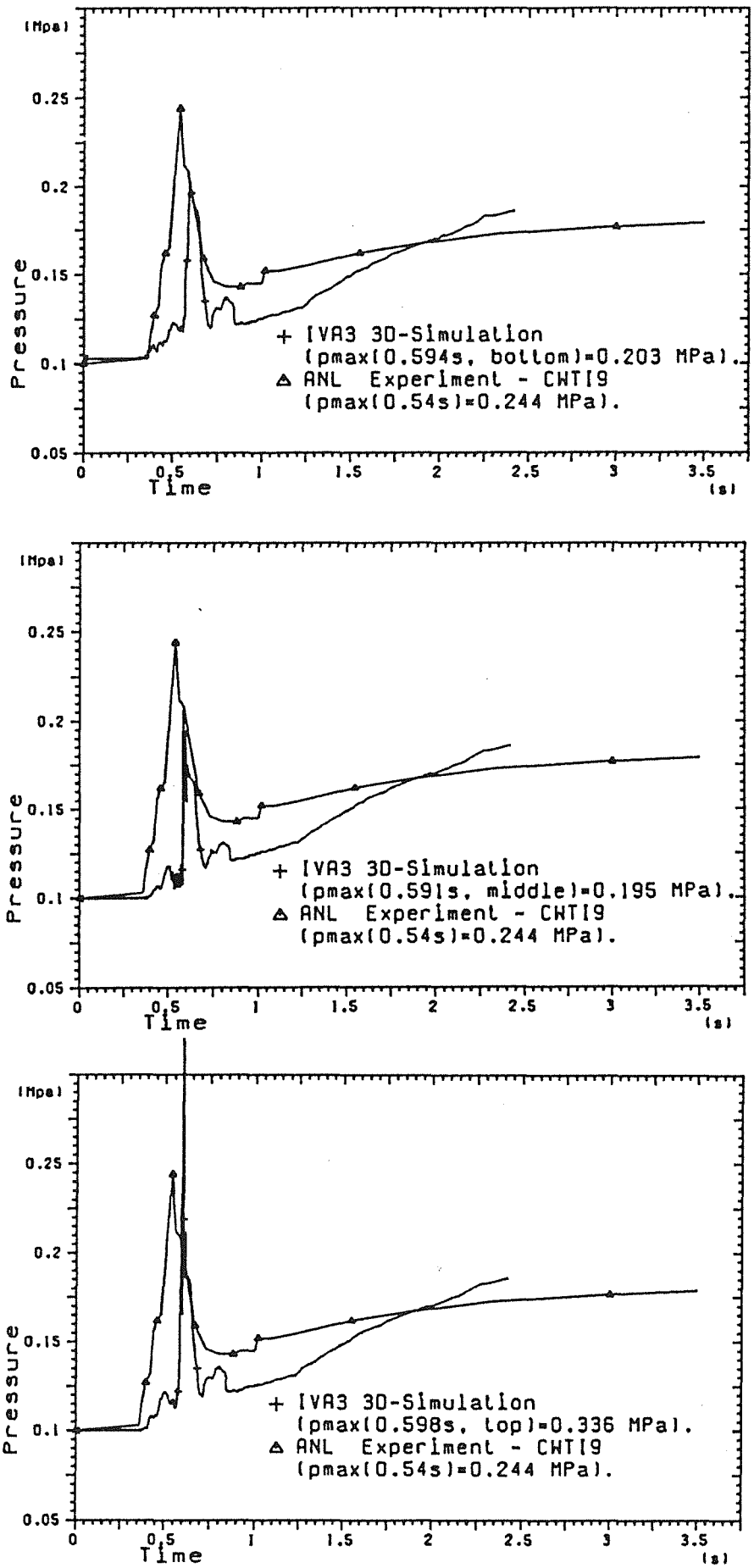


FIGURE 51. Pressures versus time in different level (bottom, middle and top) in the immediate neighborhood to the vertical wall of the interaction vessel.

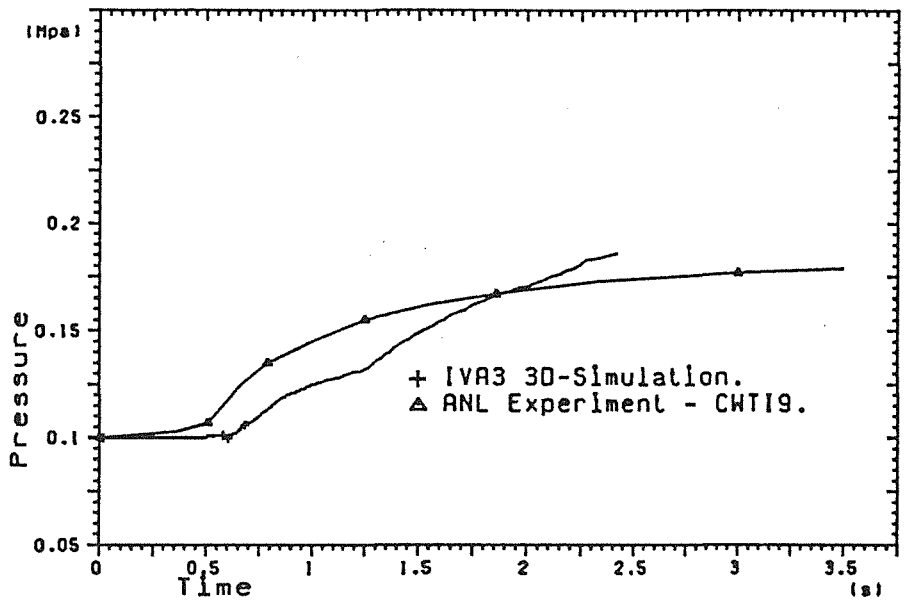


FIGURE 52. Pressure in the expansion vessel versus time.

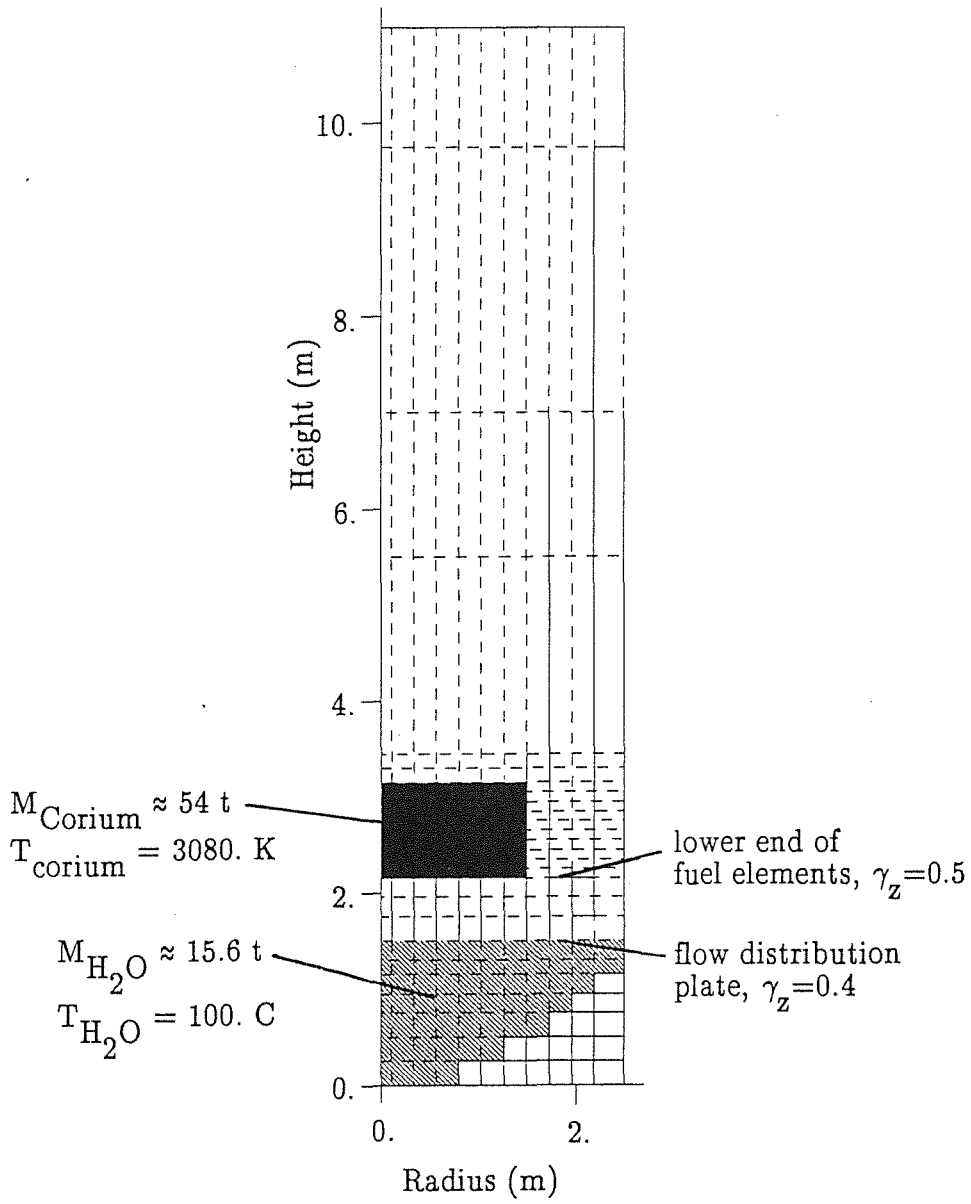


FIGURE 53 Geometry of typical PWR–1300 type reactor, cell nodding diagram for IVA3 simulation, initial conditions.

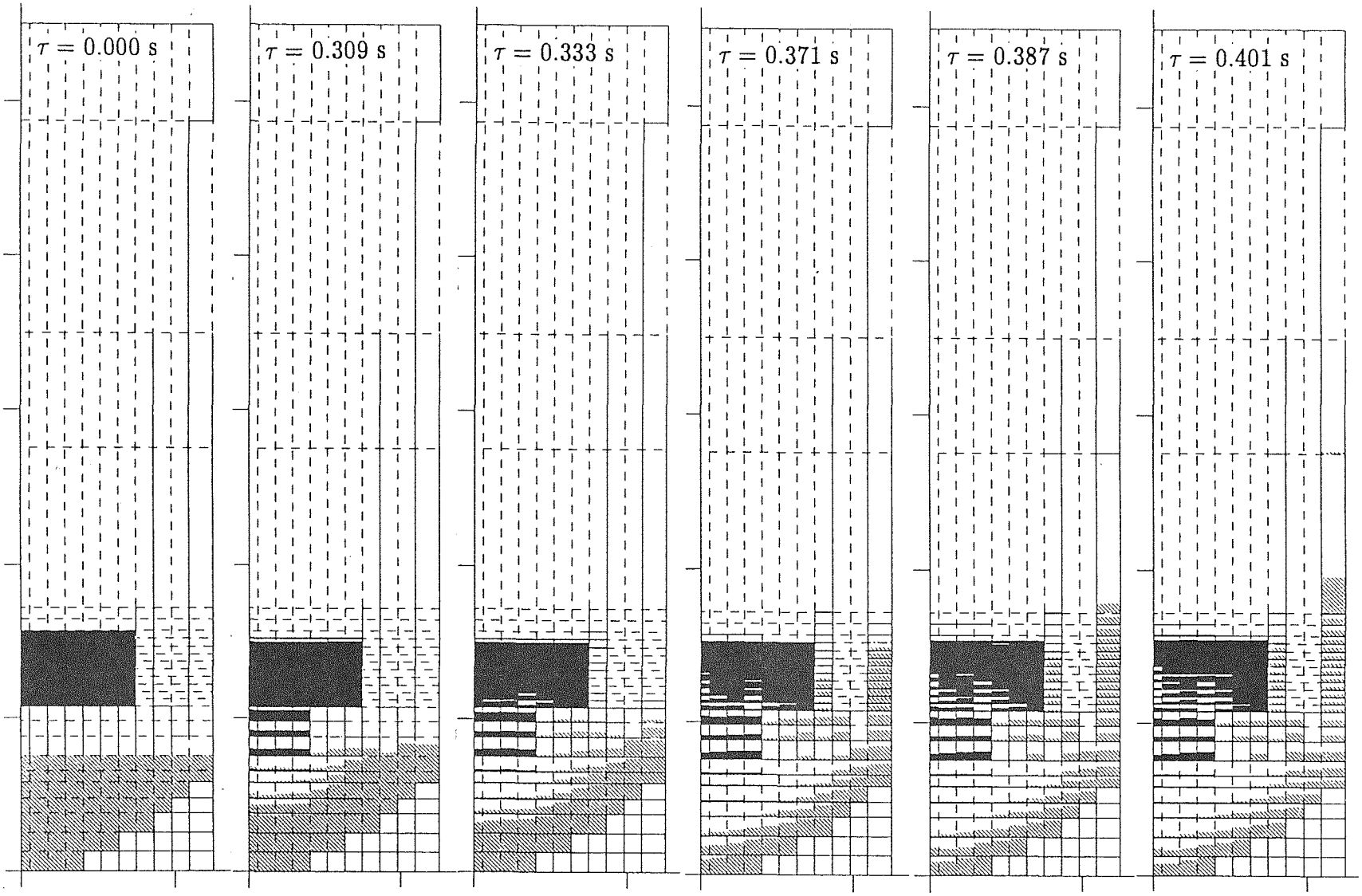


FIGURE 54 Corium, water and steam volume fractions as a function of space. Parameter – time.

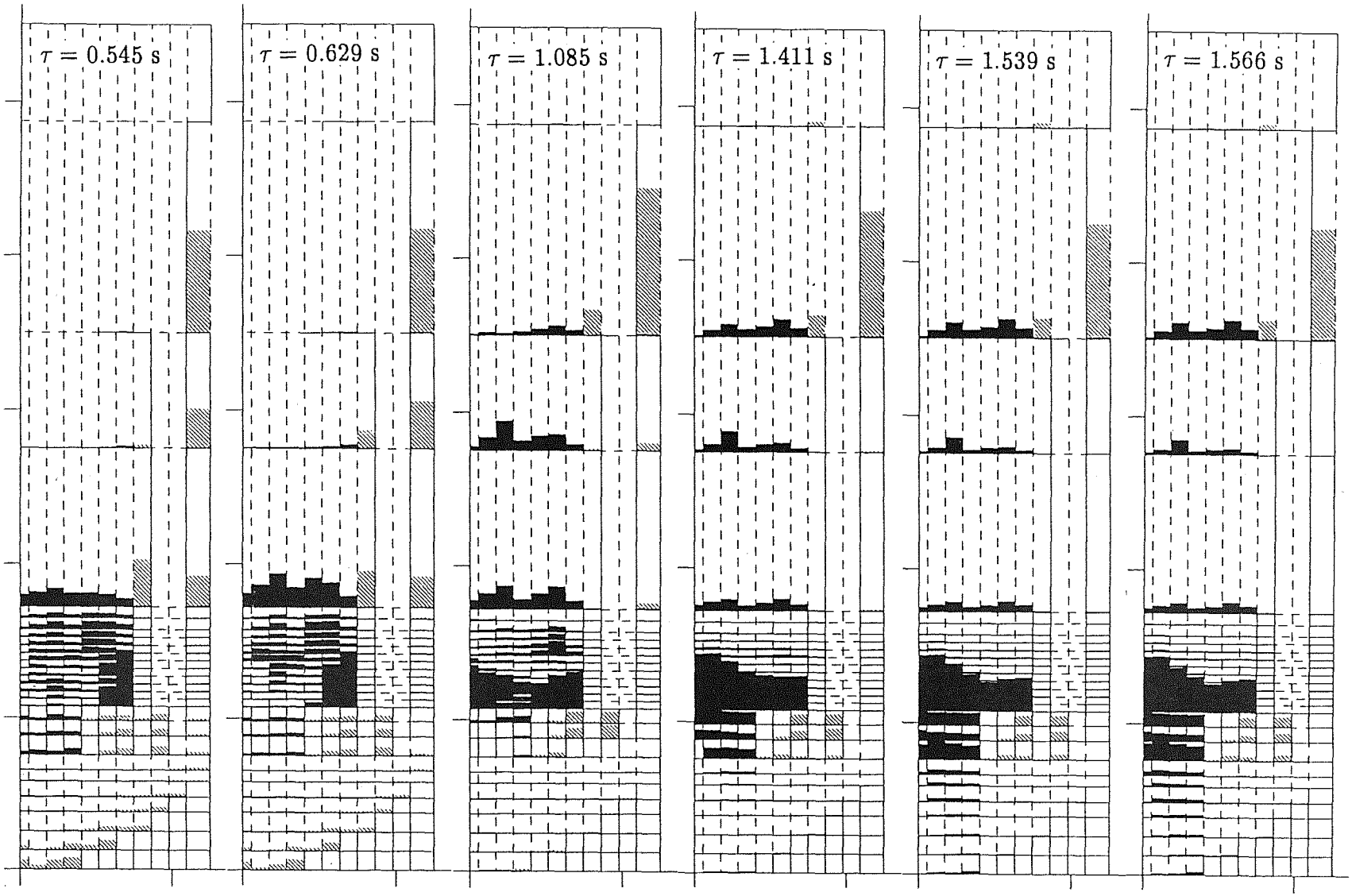


FIGURE 54 Corium, water and steam volume fractions as a function of space. Parameter – time.

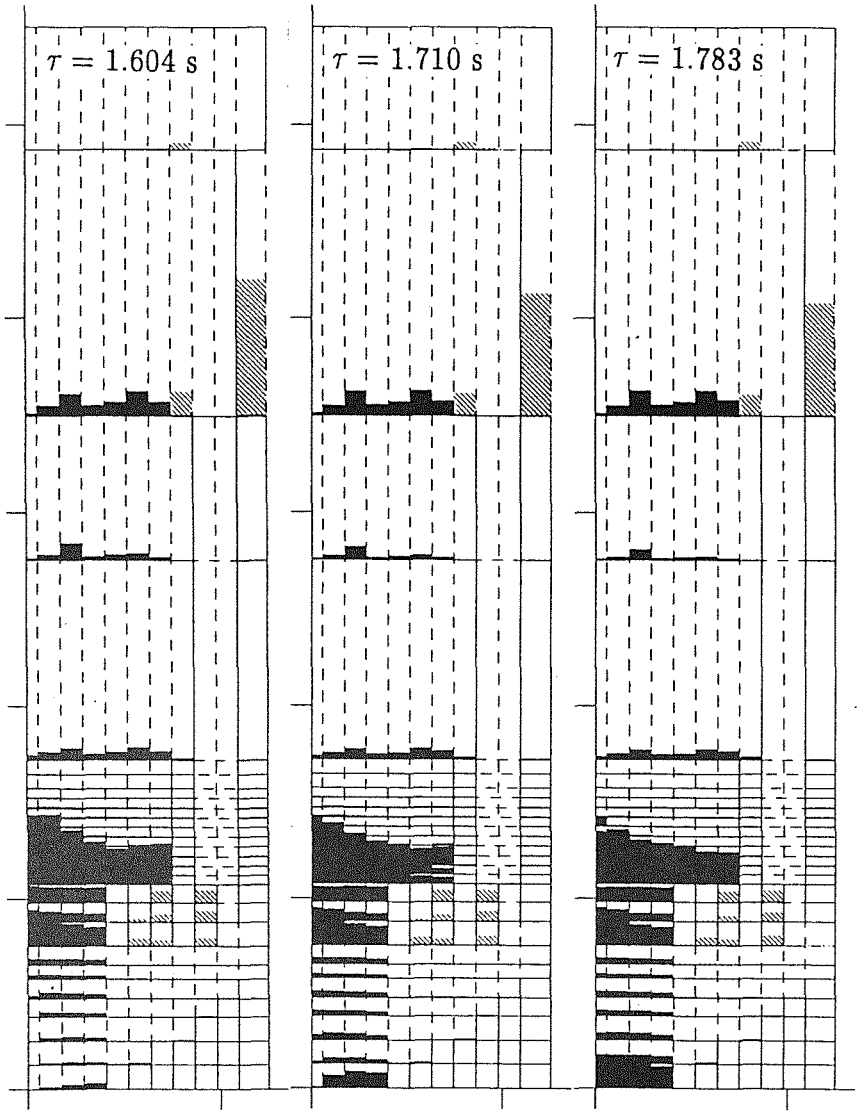


FIGURE 54 Corium, water and steam volume fractions as a function of space. Parameter – time.

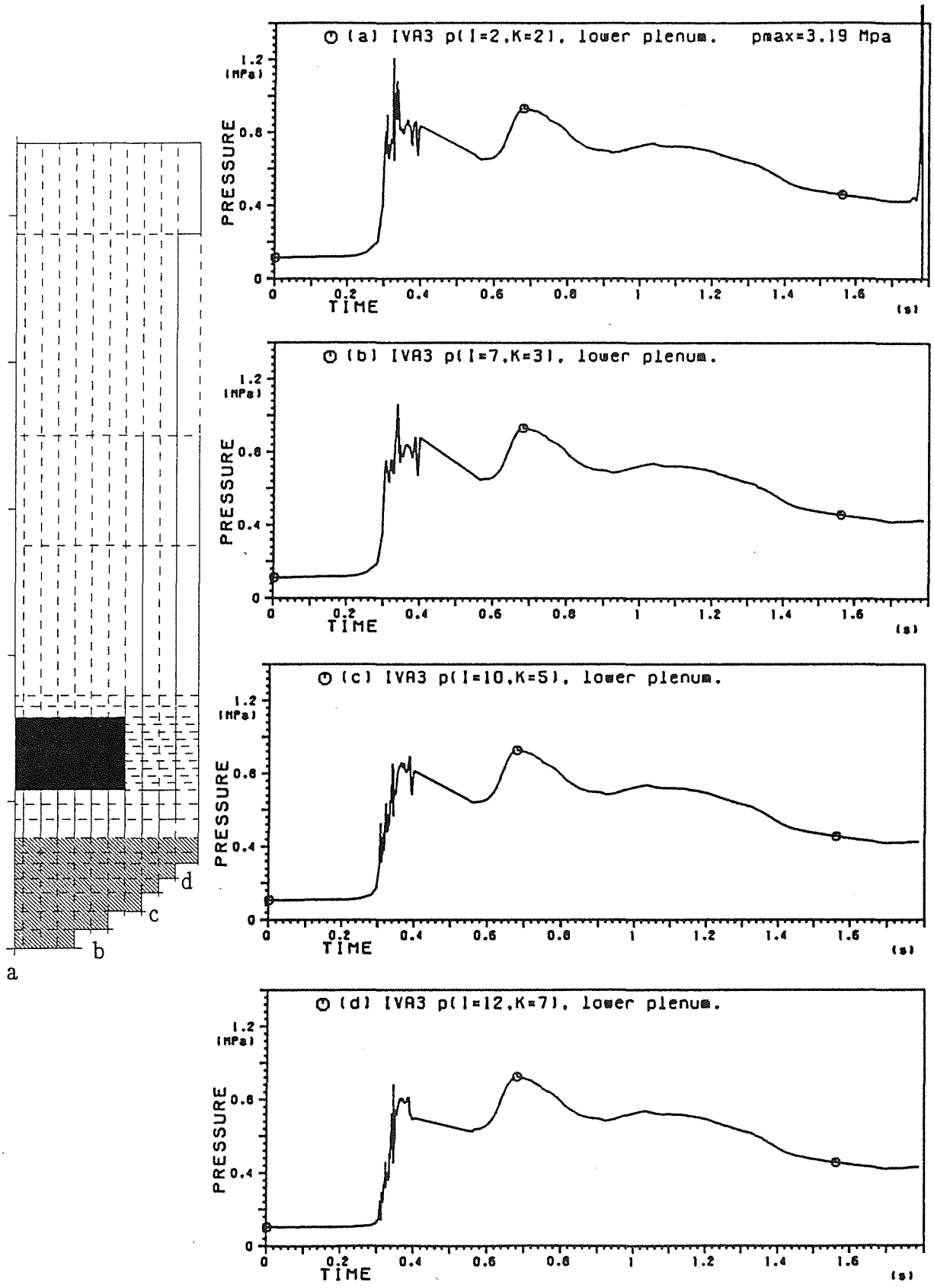


FIGURE 55 Pressure acting at different positions of the reactor vessel wall due to melt – water interaction versus time.

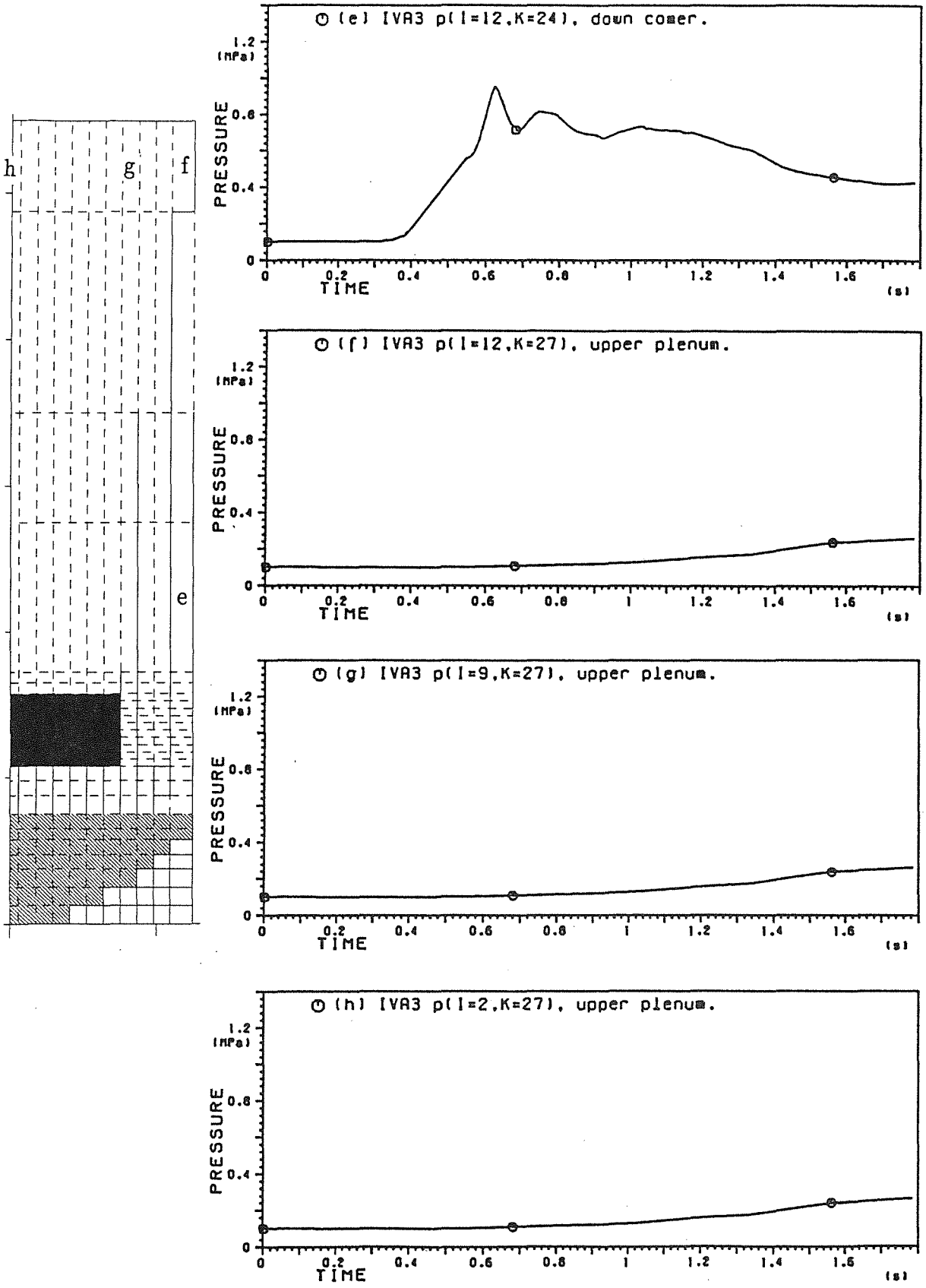


FIGURE 55 Pressure acting at different positions of the reactor vessel wall due to melt – water interaction versus time.

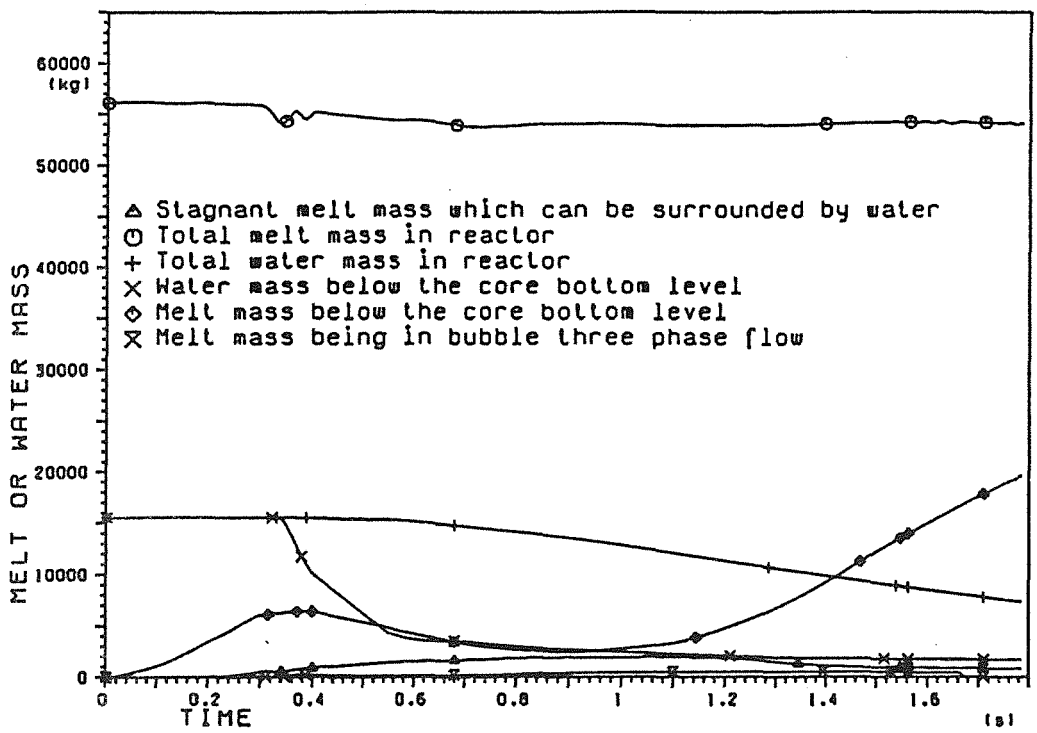


FIGURE 56 Melt and water mass as a function of time. PWR–1300 melt – water interaction. 54 t initial melt mass in the core, 15.6 t initial water mass in the lower plenum.

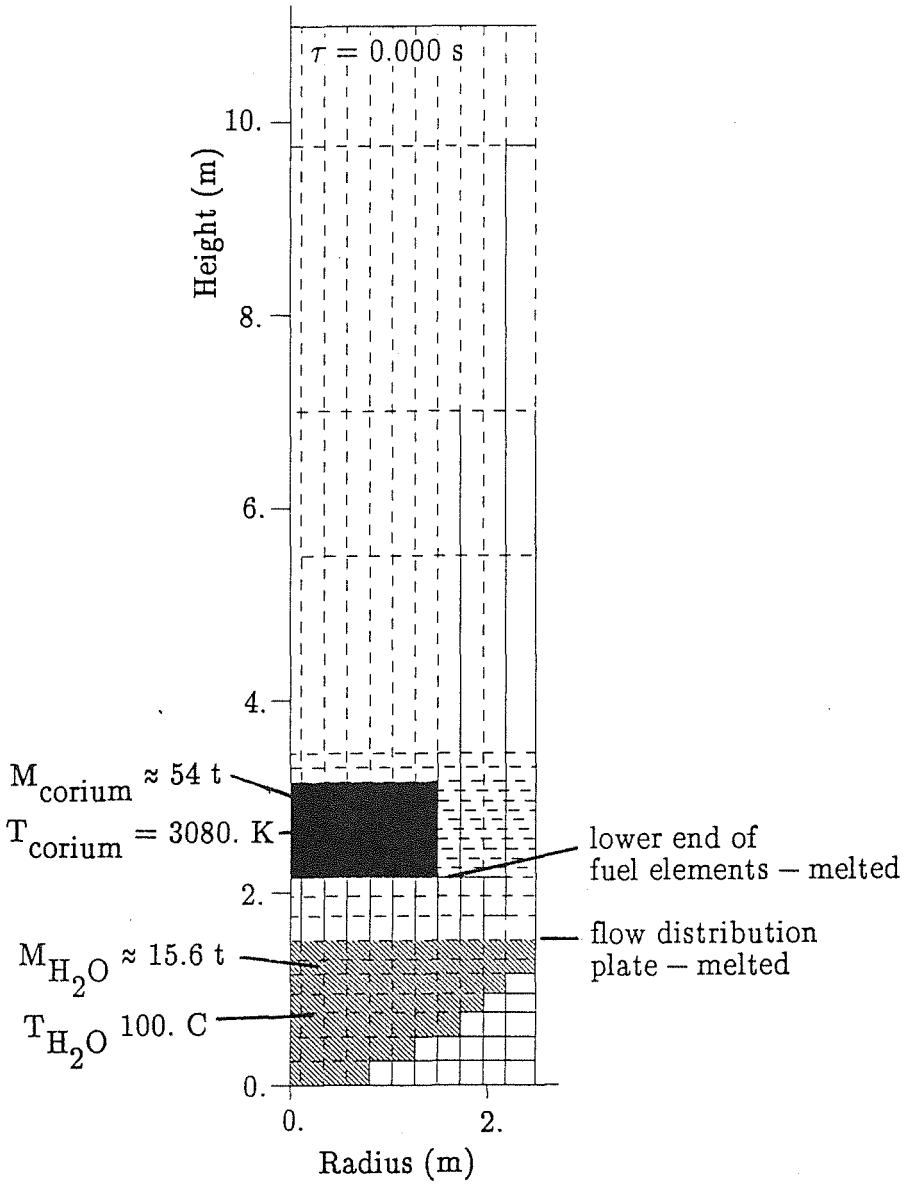


FIGURE 57 Geometry of typical PWR–1300 type reactor, cell nodding diagram for IVA3 simulation, initial conditions. Lower end of fuel elements and flow distribution plate – melted.

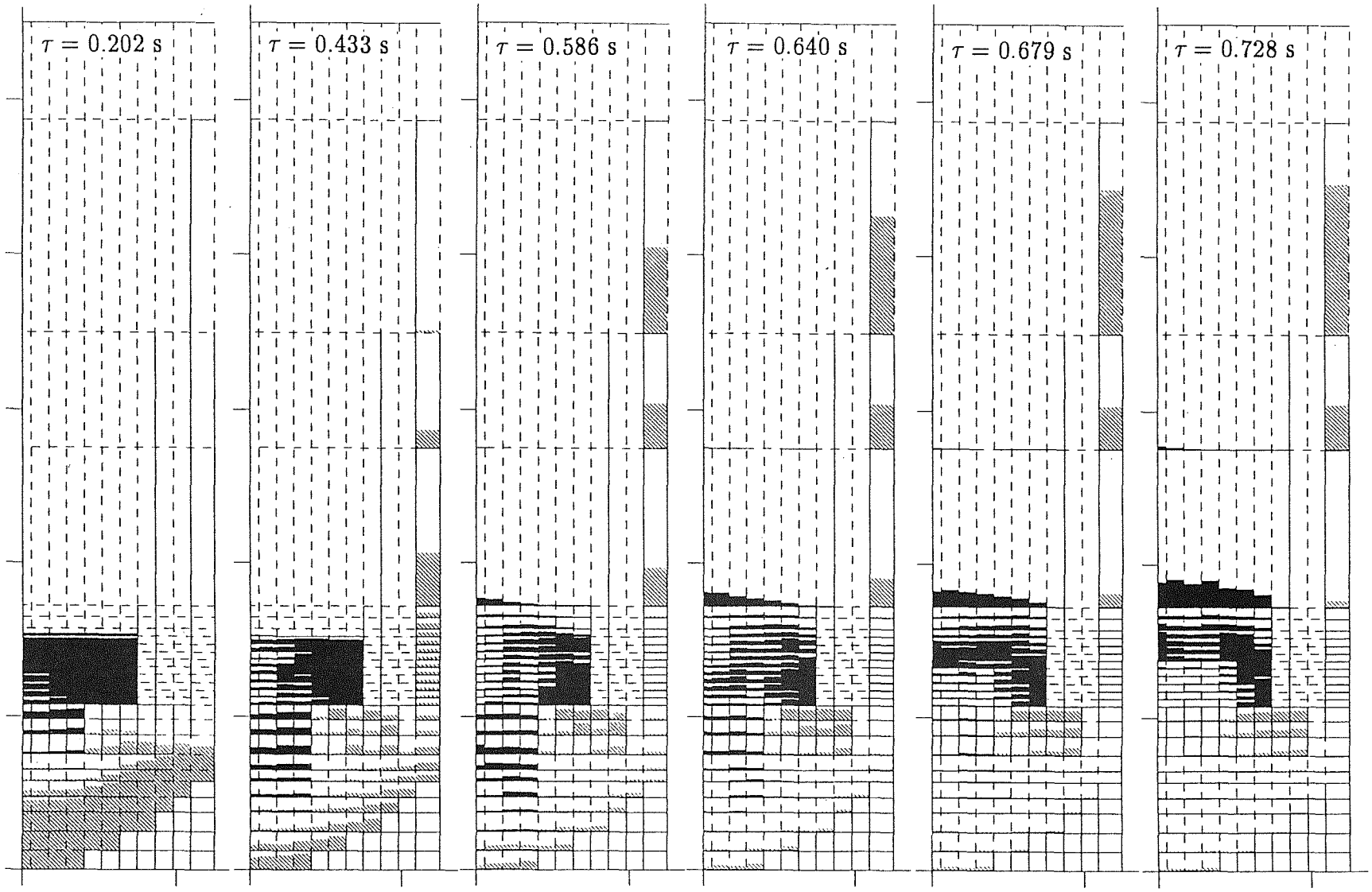


FIGURE 58 Corium, water and steam volume fraction as a function of space. Parameter – time. Lower end of fuel elements and flow distribution plate – melted.

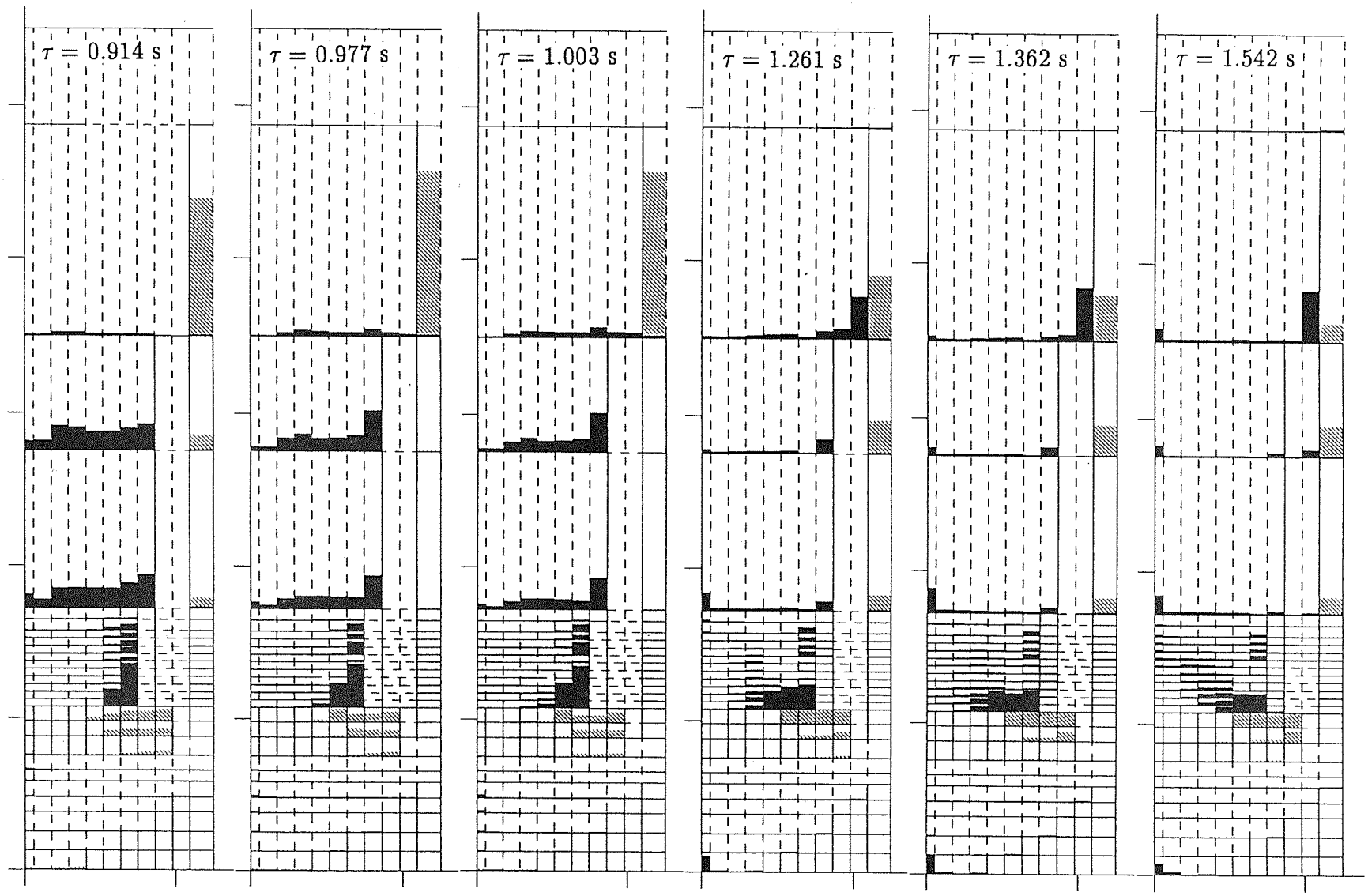


FIGURE 58 Corium, water and steam volume fraction as a function of space. Parameter – time. Lower end of fuel elements and flow distribution plate – melted.

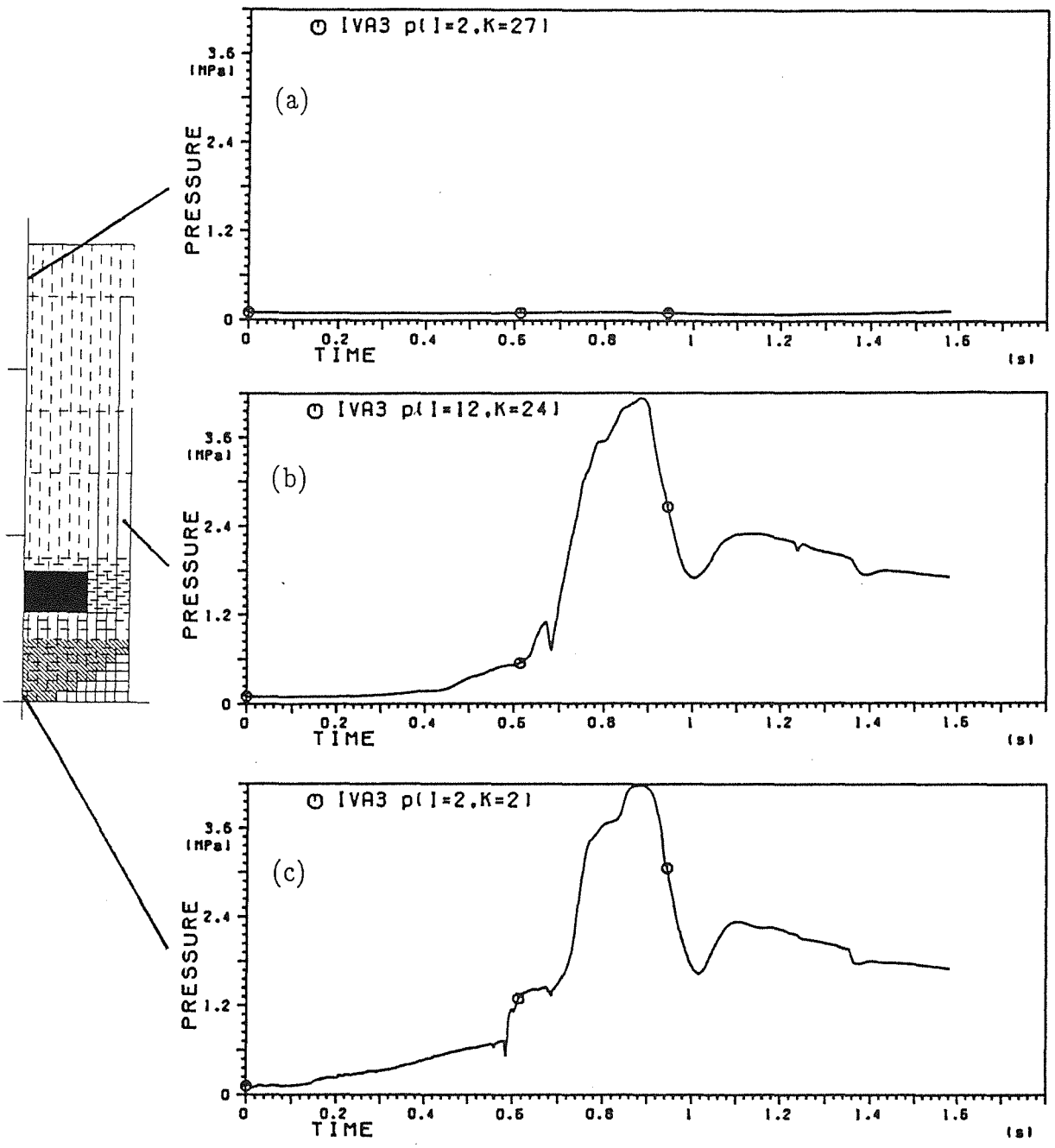


FIGURE 59 Pressure acting at different positions of the reactor vessel wall due to melt – water interaction versus time. Lower end of fuel elements and flow distribution plate – melted.

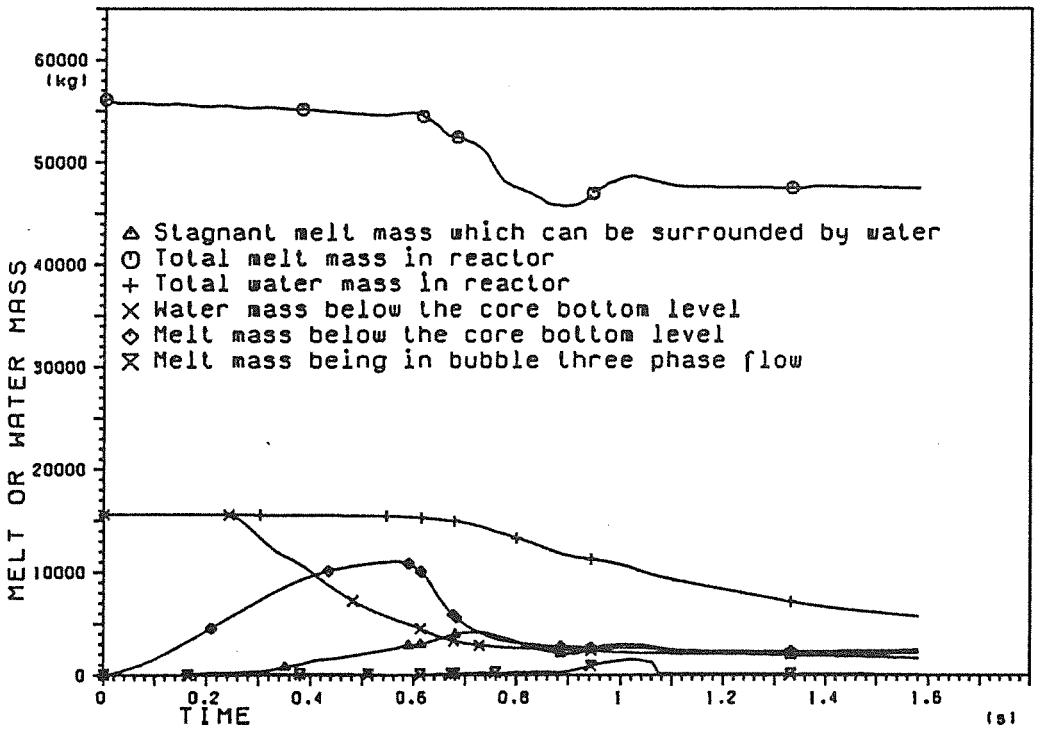


FIGURE 60 Melt and water mass as a function of time. PWR–1300 melt – water interaction. 54 t initial melt mass in the core, 15.6 t water mass in the lower plenum. Lower end of fuel elements and flow distribution plate – melted.

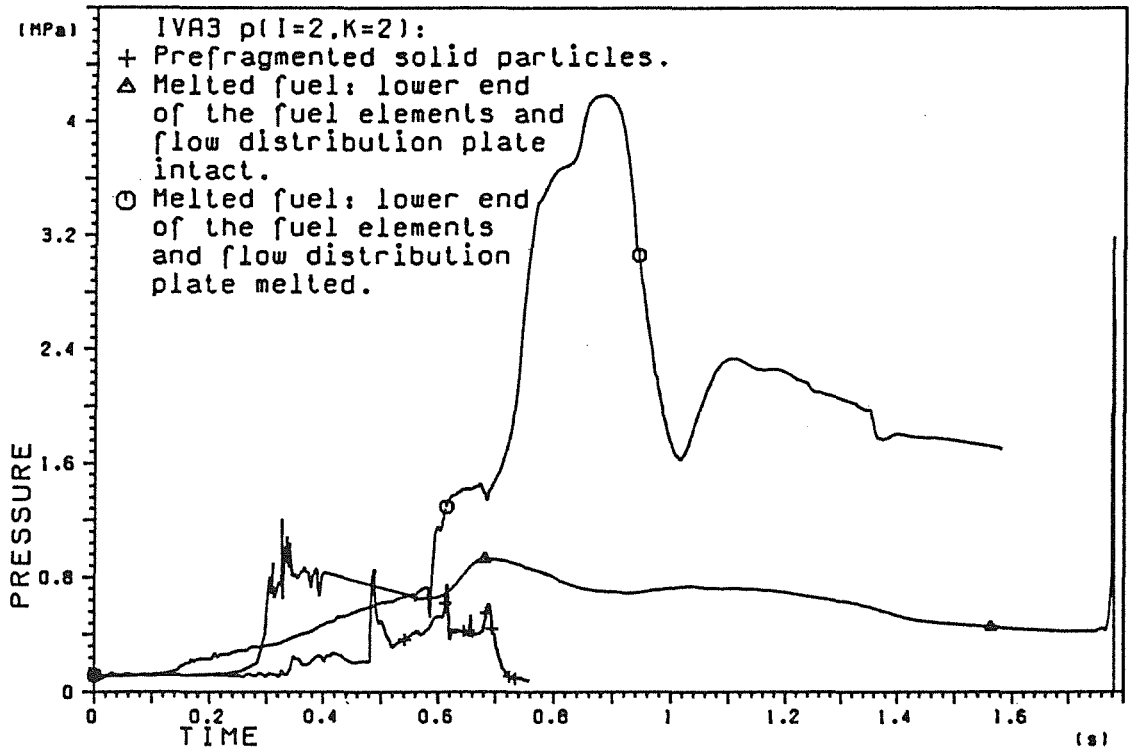


FIGURE 61 IVA3 prediction of pressure transients during melt water interaction for three different hypotheses regarding the fuel state and the structure below the core.